Magnetic-field-induced superconductivity?

M. V. Krasin'kova

A. F. Ioffe Physicotechnical Institute, Russian Academy of Sciences, St. Petersburg
(Submitted March 15, 1999)
Pis'ma Zh. Tekh. Fiz. **25**, 1–3 (July 12, 1999)

It is shown that a giant negative magnetoresistance effect in doped manganites can be explained using a model developed earlier to explain high-temperature superconductivity, based on allowance for the covalence of the transition metal–oxygen bond. This effect is caused by delocalization of π-electrons along asymmetric π-orbitals belonging to chains of covalently coupled Mn and O ions. Unlike high-temperature superconductors, in manganites this delocalization is induced by a magnetic field which ferromagnetically orients unpaired π-electrons and thereby lifts the restriction against their collective motion along the π-orbital when the manganese ions are ferromagnetically ordered. © *1999 American Institute of Physics.* [S1063-7850(99)00107-X]

We know that a giant negative magnetoresistance effect[1,2] is observed in doped manganites. Although this effect was discovered some time ago, the nature of this phenomenon is still the subject of controversy.

The present author[3,4] proposed a new approach to the study of transition-metal oxides having a perovskite structure which is based on the following assumptions.

1. The chemical bond between the transition metal and oxygen (M–O) is strongly covalent because of the difference in the electronegativities.

2. Various types of covalent bond can be formed, ranging from single-electron to two-electron bonds and even including a resonant double bond.

3. The formation of a resonant double bond is promoted by the transport of charge between various layers and consequently by the presence of charge at various layers.

4. Covalent bonds are formed in various crystallographic directions and tend to become ordered in the form of chains. This is accompanied by distortions in the MO_2 layer.

5. Any added dopants also tend to become ordered.

6. The asymmetric crystal field created by the charge difference between the layers, caused by the doping, changes the hybridization of the metal and oxygen ion orbitals perpendicular to the MO_2 plane, reduces their energy and spin state, and forms asymmetric π-orbitals relative to the MO_2 plane.

It was found that this approach to doped manganites yields the conclusion that π-electrons may also exhibit collective behavior in the MnO_2 plane, to some extent similar to that observed in the CuO_2 plane of high-temperature superconductors. The giant negative magnetoresistance effect is in fact the delocalization of π-electrons along asymmetric π-orbitals belonging to chains of covalently coupled Mn and O ions. Delocalization occurs on application of a magnetic field which ferromagnetically orients the spins of the unpaired π-electrons of O^- ions and lifts the restriction against their motion along a π-orbital when the Mn^{2+} ions are ferromagnetically ordered in a high spin state ($S=3/2$).[1)]

The motion of π-electrons along a π-orbital may be represented as the collective motion of equidistant electrons with ferromagnetically ordered spins of 1/2 along a one-dimensional ''filament.'' The collective nature of the motion over the entire MnO_2 plane arises from the polarization of the O^{2-} ions linking the various chains.

Thus, by allowing for the covalence of the manganese–oxygen bond, we can represent the electron behavior in a ferromagnetically ordered material as being similar to that in a superconductor, but this superconductivity is induced by a magnetic field. The only difference is that isolated electrons rather than pairs move in manganites.

The validity of this approach is also supported by the possibility of explaining the strong isotope effect observed in manganites.[5,6] Since the Mn and O atomic orbitals must overlap to form delocalized π-orbitals, the difference between O^{16} and O^{18} may stem from the different sizes of their atomic orbitals. This can also explain the conversion of a ferromagnetic metal into a nonmagnetic insulator when O^{16} is replaced by O^{18}.

[1)]The nature of the lattice distortions and the magnetic ordering in $LaMnO_3$ and a comparison with $CaMnO_3$ implies that Mn in $La_{0.67}Ca_{0.33}MnO_3$ is in the oxidation states Mn^{2+} and Mn^{4+} and oxygen in the MnO_2 plane occurs as O^{2-} and O^-, as will be discussed subsequently.

[1] G. Gong *et al.*, in *Abstracts of 40th Annual Conference on Magnetism and Magnetic Materials*, Philadelphia, 1995, p. 20.
[2] S. Jin, Science **264**, 413 (1994).
[3] M. V. Krasin'kova, Pis'ma Zh. Tekh. Fiz. **23**(17), 57 (1997) [Tech. Phys. Lett. **23**, 681 (1997)].
[4] M. V. Krasin'kova, Zh. Tekh. Fiz. **68**(11), 82 (1998) [Tech. Phys. **43**, 1347 (1998)].
[5] G. Zhao, M. B. Hunt, H. Keller, and K. A. Müller, Nature (London) **385**, 236 (1997).
[6] G. Zhao, H. Keller, R. L. Greene, and K. A. Muller, *Physics of Manganites*, edited by T. A. Kaplan, S. D. Gorkov, and Huang Mahanti (Plenum Press, New York, 1998).

Translated by R. M. Durham

Picosecond semiconductor lasers with a multisection saturable absorber, fabricated by heavy ion implantation

G. B. Venus, I. M. Gadzhiev, A. E. Gubenko, N. D. Il'inskaya, and E. L. Portnoĭ

A. F. Ioffe Physicotechnical Institute, Russian Academy of Sciences, St. Petersburg
(Submitted March 30, 1999)
Pis'ma Zh. Tekh. Fiz. **25**, 4–9 (July 12, 1999)

A method of implanting high-energy heavy ions across the emitter layer of a semiconductor laser has been developed to create distributed regions of ultrafast saturable absorber integrated into the cavity of a quantum-well laser. This method was used to fabricate picosecond laser diodes having high average powers and to demonstrate colliding-pulse mode-locking of a diode laser with a multisection saturable absorber.
[S1063-7850(99)00207-4]

Recently considerable success has been achieved in the generation of high-power picosecond pulses by semiconductor lasers.[1–3] However, the average power of these devices is at most 0.5 mW and is limited by their high pulsed threshold currents. In the present study we consider a new method of implanting high-energy heavy ions across the emitter layer of a semiconductor laser, aimed at fabricating *QW*-switched, mode-locked picosecond lasers based on quantum-well structures having a high average power.

As we showed in our previous studies, bombardment of semiconductor materials with high-energy heavy ions can produce a high-quality optical material with ultrashort nonequilibrium carrier lifetimes. These times do not exceed a few picoseconds at irradiation doses above 10^{11} ion/cm^2 (Ref. 4). Semiconductor materials bombarded with high-energy heavy ions have properties similar to *LT*-GaAs and may be used to fabricate saturable absorbers for semiconductor lasers and also to produce ultrafast photodetectors.[5]

In double-heterostructure[6] and single-heterostructure[2] semiconductor lasers highly efficient *QW*-switching can be achieved when a saturable absorber is fabricated by implanting 70–80 MeV ions into the semiconductor laser mirrors. For lasers with a quantum-well active region, the incorporation of a saturable absorber region near the laser mirrors cannot produce a sufficient modulation of the absorption because of the small Γ-factor and the high residual losses in the cavity at elevated radiation doses. The effective modulation of the absorption can be increased in quantum-well structures by distributing the regions of saturable absorber inside the laser cavity of the diode. For this purpose we developed a method of implanting high-energy heavy ions across the emitter region of the laser from above (Fig. 1). In this irradiation geometry the required ion energy (N, Ar, Kr) is between 2 and 8 MeV depending on the layer thickness of the laser structure. It was demonstrated experimentally that this energy is sufficient to form regions of highly efficient saturable absorber stable to optical annealing. In order to protect the laser regions not being implanted, we designed and fabricated masks using galvanically deposited gold (1.5–6 μm thick) and thick photoresist layers (4–16 μm thick). The use of photolithographic protective masks having characteristic dimensions of 2–3 μm opens up new possibilities for the overall choice of picosecond laser design and for varying the parameters of specific sections within the ultrafast saturable absorber region.

In order to demonstrate the possibilities of this new method, we used stripe InGaAs lasers with a strained quantum-well region and a lasing wavelength around 0.98 μm. The structure was bombarded with N^{3+} (5.6 MeV, 10^{11} ion/cm^2 dose) ions through a segmented photoresist mask 6 μm thick (Fig. 1). The lasers had a cavity of length 1100 μm which consisted of five amplifying sections 200 μm long separated by 20 μm regions of saturable absorber. When these structures were pumped by 1.5 ns current pulses of 0.80–0.95 A amplitude, we obtained single optical pulses having durations of 43–45 ps and energies of 55–58 pJ (Fig. 2). This picosecond pulse energy is a very good

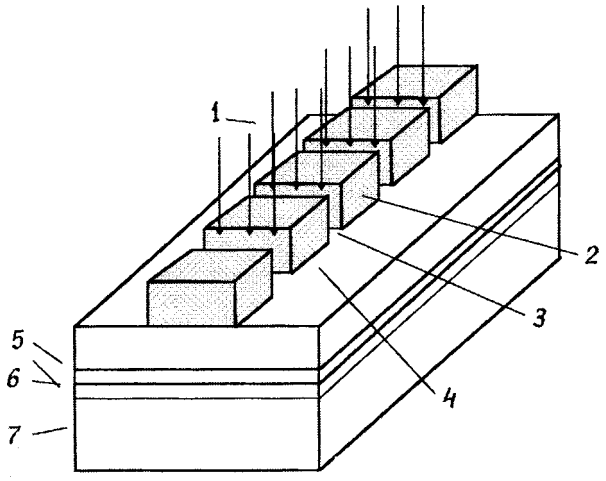

FIG. 1. InGaAs laser with distributed regions of saturable absorber integrated into its cavity by implantation of high-energy ions across the upper emitter layer: *1* — heavy ion implantation to fabricate a saturable absorber, using a 5×10^{10}–10^{12} cm^{-3} dose of 7 MeV Ar ions; *2* — implantation mask, 10 μm thick; *3* — regions of saturable absorber (20 μm); *4* — five amplifying regions (200 μm); *5* — AlGaAs; *6* — quantum-well InGaAs, and *7* — *n*-GaAs.

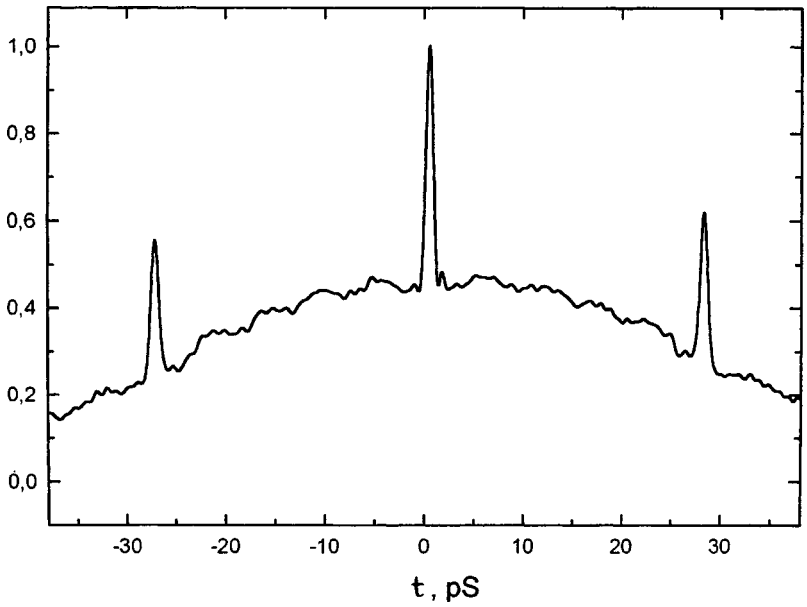

FIG. 2. Autocorrelation function of a picosecond pulse from an InGaAs laser with a multisection saturable absorber implanted with a 10^{11} ion/cm^2 dose of (5.6 MeV) N^{3+} ions

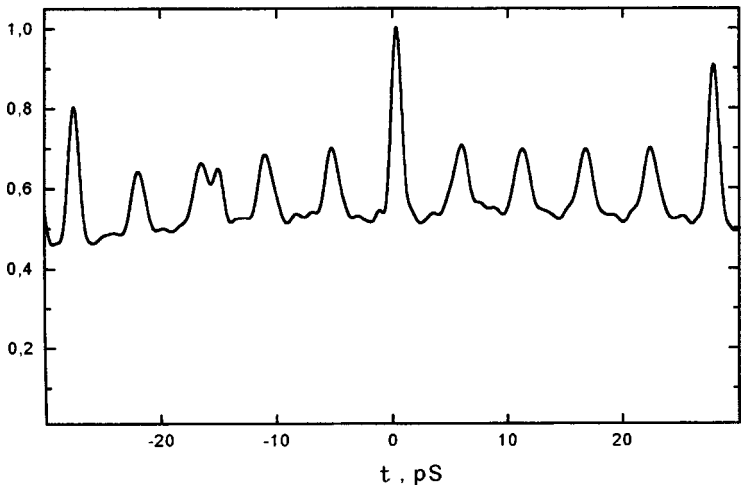

FIG. 3. Autocorrelation function of radiation from an InGaAs laser with a multisection saturable absorber (N^{3+} ions, 5.6 MeV, 10^{12} ion/cm^2) under conditions of colliding-pulse mode-locking with a multisection saturable absorber.

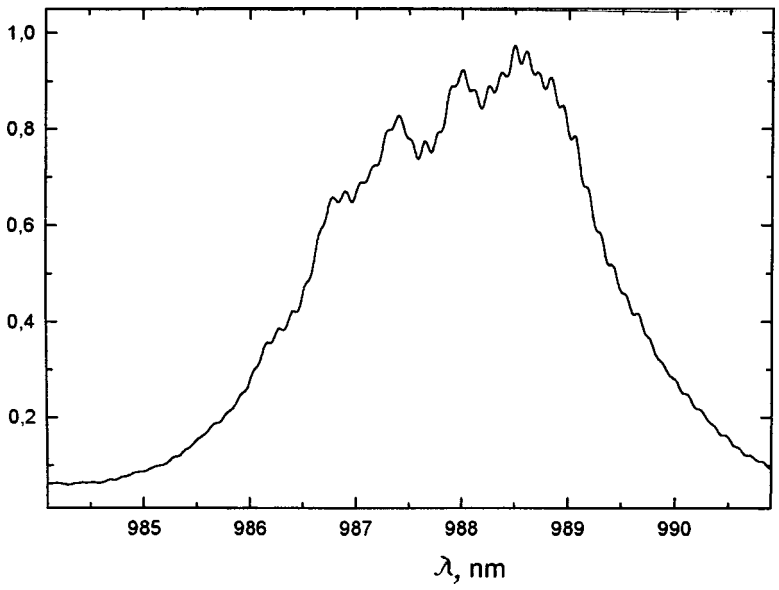

FIG. 4. Emission spectrum of an InGaAs laser with a multisection saturable absorber (N^{3+} ions, 5.6 MeV, 10^{12} ion/cm^2) under conditions of colliding-pulse mode locking with a multisection saturable absorber.

characteristic for low-stripe quantum-well lasers, making it possible to fabricate a source of picosecond optical pulses with an average power of 1.1 mW and a pulse repetition frequency of 20 MHz. The short duration of the optical pulse compared with the laser round-trip ($\tau_{opt}/t_{rt} \approx 1.6-1.7$) indicates that this multisegment saturable absorber operates very efficiently under Q-switched conditions. In our view, this operating efficiency can be attributed not only to the high optical quality of the material in the implanted regions but also to the processes of correlated opening of these regions. This is also indicated by the peaks on the autocorrelation curve of the optical pulse (Fig. 2).

As the radiation dose is increased to 10^{12} ion/cm^2, the correlated opening of the saturable absorber and the reduction in the lifetimes of the nonequilibrium carriers in these regions cause a transition to colliding-pulse mode locking with a multisection saturable absorber, first described by Martins-Filho *et al.*[7] It can be seen from the autocorrelation curve (Fig. 3) that in this regime the laser generates pulses of around 1 ps with a repetition frequency of 180 GHz which is five times higher than the natural frequency of the laser cavity. The presence of microwave modulation of the laser diode radiation can also be seen clearly from its radiation spectrum (Fig. 4). The possibility of achieving a further increase in the lasing frequency and simplifying the laser design compared with reverse-biased sections of saturable absorber[7] indicates that this implantation method may be potentially useful for terahertz optoelectronics.

[1] B. Zhu, I. H. White, K. A. Williams, and F. R. Laughton, IEEE Photonics Technol. Lett. **8**, 503 (1996).
[2] E. L. Portnoi, G. B. Venus, A. A. Khazan, I. M. Gadjiev, A. Yu. Shmarcev, J. Frahm, and D. Kuhl, IEEE J. Sel. Top. Quantum Electron. **3**(2), 256 (1997).
[3] N. Stelmakh, J. N. Lourtioz, G. Marquebielle, and J. P. Hirtz, IEEE J. Sel. Top. Quantum Electron. **3**(2), 245 (1997).
[4] E. A. Avrutin and M. E. Portnoĭ, Fiz. Tekh. Poluprovodn. **22**, 1524 (1988) [Sov. Phys. Semicond. **22**, 968 (1988)].
[5] E. H. Bottcher, E. Droge, D. Bimberg, D. Kuhl, J. Frahm, G. B. Venus, and E. L. Portnoi, in *10th Annual Meeting, LEOS'97*, 1997, Vol. 2, p. 319.
[6] E. Portnoi, E. Avrutin, and A. V. Chelnokov, in *Joint Soviet–American Workshop on the Physics of Semiconductor Lasers*, Leningrad, 1991 (American Institute of Physics, New York, 1991), pp. 58–66.
[7] J. F. Martins-Filho, E. A. Avrutin, C. N. Ironside, and J. S. Roberts, IEEE J. Sel. Top. Quantum Electron. **1**, 539 (1995).

Translated by R. M. Durham

Chemical reactions at high temperatures as a source of pressure pulses

V. P. Kortkhondzhiya and M. O. Mdivnishvili

Institute of Physics, Georgian Academy of Sciences, Tbilisi
(Submitted October 13, 1998; resubmitted March 2, 1999)
Pis'ma Zh. Tekh. Fiz. **25**, 10–14 (July 12, 1999)

It is shown that if the explosion of a wire in a liquid is accompanied by a chemical reaction between the wire material and the liquid in which the wire explodes, the chemical reaction products are the main mechanism responsible for creating pressure pulses. © *1999 American Institute of Physics.* [S1063-7850(99)00307-9]

1. We are familiar[1,2] with a method of creating pressure pulses using the explosion of a wire in a liquid where the liquid serves to transfer the pressure created as a result of the explosion of the wire. The pressure pulse source is a metal plasma formed as a result of the passage of a large pulsed current, of the order of hundreds of kiloamperes, through a metal conductor.

2. Experiments have shown that the parameters of the pressure pulse depend strongly on the conductor–liquid system in which the wire explodes.

We shall subsequently attempt to answer various questions relating to the explosion of a wire in a liquid. One of these questions is what is the pressure pulse source in the presence of a chemical reaction.

3. When copper and aluminum wires explode in water, for the same capacitor bank energy, ≈ 11 kJ, the masses of the exploded wires are 2.1 g for copper and 1 g for aluminum. The pressure pulses formed are $\approx 5\times 10^7$ and $\approx 8\times 10^7$ Pa and their durations are ≈ 0.18 and ≈ 0.8 ms, respectively.

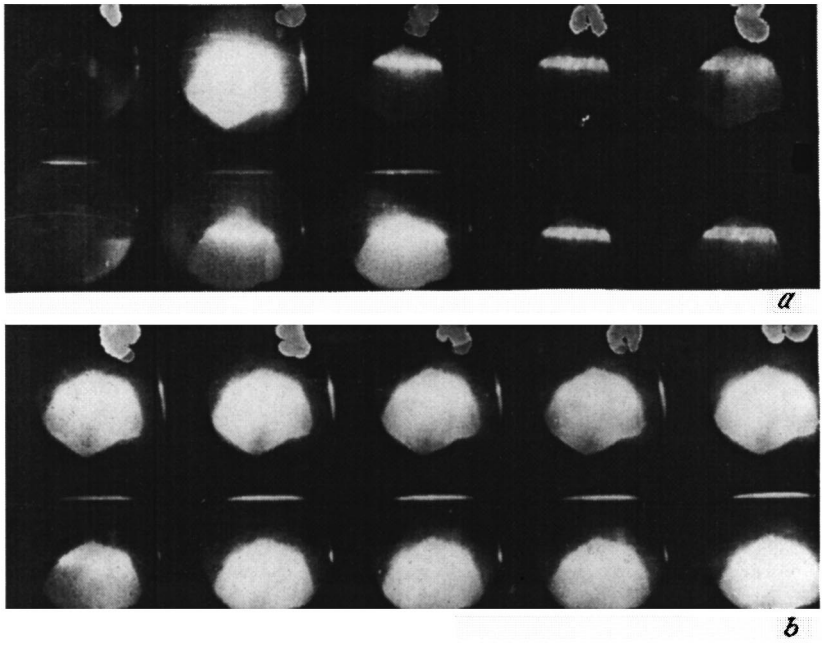

FIG. 1. Framing photographs of the explosion of an aluminum wire in water (a, b); oscilloscope traces of discharge current (upper trace) and voltage (lower trace) for the explosion of aluminum in water (c). Discharge voltage $U=5$ kV.

The oscilloscope traces of the discharge current and voltage for the explosion of copper and aluminum wires in water differ substantially. For a copper wire[2] a discharge current peak is observed as a result of the explosion of the wire. The voltage trace shows that some of the capacitor bank energy is expended in the explosion and some remains unused. In the case of aluminum, the discharge current pulse caused by the explosion of the aluminum is followed by a broader pulse. The oscilloscope trace of the voltage shows that all the capacitor bank energy is used up.

Figures 1a and 1b show the first eighteen frames of a streakhigh-speed photograph of an aluminum explosion in water taken using the framing mode of an image-converter streak camera. The lower left outermost frame is the first, the upper one is the second, and so on. The exposure is 0.02 ms. It can be seen that after ≈ 15 ms the glow from the aluminum explosion has decayed considerably (Fig. 1a) and from approximately 0.16 ms (Fig. 1b) a bright glow begins to appear caused by the breakdown of the reaction products. This glow lasts for approximately 0.8 ms. Figure 1c shows oscilloscope traces of the discharge current (upper trace) and voltage (lower trace) for the explosion of aluminum in water. The left outermost peak on the discharge current trace corresponds to the explosion of aluminum. The duration of the discharge current is approximately 0.15 ms. The following peaks are ascribed to the breakdown of the reaction products. The total duration of the discharge current caused by the explosion of the aluminum and the current attributed to breakdown of the vapor–gas mixture is approximately 0.8 ms, which shows good agreement with the duration of the discharge glow recorded by the streak camera.

In general, the chemical reaction can be expressed as:

$$l\mathrm{M}+n\mathrm{L}\rightarrow s\mathrm{K}+h\mathrm{G}+Q.$$

The interaction between l atoms of metal M and n molecules of liquid L results in the formation of s molecules of compound K and h molecules of gas G, and Q is the heat of the reaction.

When an aluminum wire explodes in water, the temperature may reach the vaporization temperature of aluminum, 2720 K, and the following reactions may take place:

$$2\mathrm{Al}+6\mathrm{H_2O}\rightarrow 2\mathrm{Al(OH)_3}+3\mathrm{H_2}, \quad \text{(a)}$$

$$2\mathrm{Al}+3\mathrm{H_2O}\rightarrow \mathrm{Al_2O_3}+3\mathrm{H_2}+Q, \quad \text{(b)}$$

$Q=-1680$ kJ/m (Ref. 3).

A chemical reaction also takes place when zirconium explodes in water.[4]

If reaction (a) predominates, because of the high temperature it is followed by the transition

$$2\mathrm{AlOH_3}\rightarrow \mathrm{Al_2O_3}+3\mathrm{H_2O}+Q.$$

This reaction results in the formation of a vapor–gas mixture which is ionized by the high-power ultraviolet radiation accompanying the explosion of the wire. Since the discharge gap still has sufficient voltage to break down the vapor–gas mixture, this breakdown does take place, and the higher the voltage applied to the discharge gap, the earlier this breakdown occurs. This explains the origin of the broader discharge current pulse discussed above. When copper explodes, no chemical reaction takes place and pure copper powder is precipitated after the explosion. When aluminum explodes in water, this gives a suspension of Al_2O_3 in water and if the aluminum mass is ~ 1 g, ~ 15 kJ of heat is released. A mass of 700 g water becomes heated to 20°C. If the entire capacitor bank energy of ~ 5.4 kJ was expended in heating this same quantity of water, the temperature rise would be 8 °C. The release of a large quantity of energy 1680 kJ/m around the discharge channel as a result of the exothermic chemical reaction causes its products to be heated to high temperatures ($\sim 7.8\times 10^3$ K) and they develop a high pressure. This will be discussed in greater detail in an article to be published.

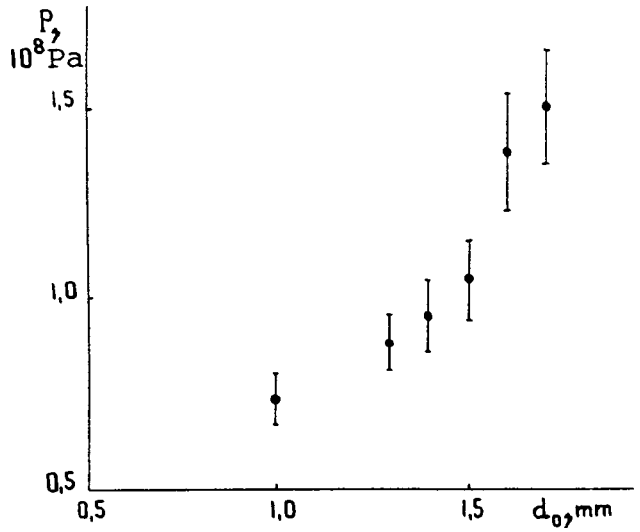

FIG. 2. Amplitude of pressure pulse versus diameter d_0 of exploded aluminum wire in water. Discharge voltage $U=5$ kV.

Figure 2 gives results of experimental measurements of the amplitude of the pressure pulse as a function of the diameter d_0 of an aluminum wire 320 mm long exploded in water. The amplitude of the pressure pulse was measured at the wall of a cylindrical container having a cross-section of diameter $d=5.5$ cm.

The chemical reaction, which is a slower process than the electrical explosion of the wires, and the breakdown of the gaseous products of this reaction increase the duration of the pressure pulse, with the result that this pulse may last several milliseconds when an aluminum wire explodes in water. When wires explode in a liquid without any chemical reaction this duration is determined by that of the discharge current, and in our case for the explosion of a copper wire in water is less than 0.2 ms.

4. To sum up, if the explosion of a wire in a liquid is accompanied by a chemical reaction between the exploded wire and the liquid in which the explosion takes place, the gaseous products of the chemical reaction are the main source of the pressure pulse.

[1] E. V. Krivitskiĭ, *Dynamics of Electrical Explosions in Liquids* [in Russian], Naukova Dumka, Kiev (1986), 400 pp.
[2] V. P. Kortkhondzhiya, M. O. Mdivnishvili, and M. I. Taktakishvili, in press, Zh. Tekh. Fiz. (1999).
[3] G. W. C. Kaye and T. H. Laby, *Tables of Physical and Chemical Constants and Some Mathematical Functions*, 16th ed. (Longman, New York, 1995) [Russ. transl. of earlier ed., Fizmatgiz, Moscow, 1962, 247. pp.].
[4] *Electrical Explosion of Conductors*, edited by A. A. Rukhadze and I. S. Shpigel [in Russian], Mir, Moscow (1965), pp. 239–259).

Translated by R. M. Durham

Acoustic emission and dynamical relaxation of nonchemical energy in martensitic transformations

V. A. Plotnikov

Altai State University, Barnaul
(Submitted October 2, 1998)
Pis'ma Zh. Tekh. Fiz. **25**, 15–22 (July 12, 1999)

Athermal (above-barrier, critical-velocity) motion of the martensite boundary is accompanied by the production of spontaneous transition radiation and (or) spontaneous acoustic bremsstrahlung. The acoustic transition radiation is strongly related to the velocity of the interphase boundary and the correlated (coherent) nature of the formation of a set of martensite crystals. Conversely, the bremsstrahlung is produced when the correlation is destroyed.
 [S1063-7850(99)00407-3]

In alloys not inclined to phase hardening, acoustic emission during cooling (direct transformation) cannot be caused by plastic relaxation of the microstresses generated by the martensitic structure in the course of martensitic transformations. Moreover, during heating (reverse transformation) the acoustic emission is clearly of a different nature. According to our data, the nature of this emission determines the asymmetric and symmetric dissipation of nonthermal energy accompanying reversible martensitic transformations, and the approach we have developed can be used to classify the various results of other investigations accumulated so far.[1]

1. Figure 1 shows fragments of acoustic curves (the mean-square piezotransducer voltage as a function of the heating or cooling time) observed during reversible martensitic transformations (first cycles) in ternary alloys. A characteristic feature reliably observed in the experiments is the asymmetry of the acoustic emission in alloys having copper concentrations up to 8.0 at.% and the nearly symmetric ratio of the radiation energy for the direct and reverse martensitic transformations in alloys having copper concentrations of 9.0–11.0 at.%.

Repeated cycles of martensitic transformation influence the evolution of the acoustic emission in different ways (Fig. 2). In alloys having a copper concentration up to 8.0 at.% the radiation energy decreases during the direct martensitic transformation and increases during the reverse transformation. In alloys having a copper concentration of 9.0 at.% or higher, cycling barely influences the radiation energy but, most importantly, the symmetric character of the emission is conserved.

2. We shall compare the laws governing the acoustic emission with the kinetic characteristics of martensitic transformations and the mechanical properties of the alloys.[2] It can be seen from Tables I and II that alloys having a low (up to 6.0 at.%) copper content are characterized by a high martensitic shear stress and a tendency to phase hardening (an increase in the yield point during cycling), the martensitic transformations exhibit a broad hysteresis loop, the slope (dY/dT) of the martensite curve is small, and slow growth microkinetics, i.e., contraction of martensitic plates is observed.

Conversely, alloys having a high (greater than 8.0 at.%) copper content exhibit a low martensitic shear stress and a weak tendency to phase hardening (no increase in yield point occurs during cycling), the martensitic transformations have a narrow hysteresis loop, the martensite curve has a large slope, and the disappearance of the martensitic crystals exhibits microexplosive kinetics.

Alloys having similar martensitic shear stresses and yield points (alloys containing less than 8.0 at.% copper) typically exhibit the first type of acoustic emission asymmetry during a martensitic transformation cycle, which degrades to saturation during cycling and undergoes a transformation to the second type of asymmetry.

For alloys having an anomalously low martensitic shear stress we observe a nearly symmetric type of acoustic activity during direct and reverse martensitic transformations which depends weakly on the cycling.

The alloys can logically be divided into two groups according to their mechanical characteristics, martensitic transformation microkinetics, and the manifestation of acoustic activity.

3. It was shown by Plotnikov *et al.*[3,4] that for the first group of alloys the acoustic emission accompanying a direct martensitic transformation is caused by plastic relaxation of microstresses which have built up during the transformation. The fact that the martensitic shear stress is close to the yield point indicates that there is a high probability that the local microstresses will reach the plastic (dislocation) shear stress. The buildup of complete dislocations strengthens the crystal structure in both the martensitic and high-temperature phases (causing an increase in the yield point). An increase in the difference between the yield point and the martensitic shear stress during cycling is accompanied by the degradation of plastic relaxation and from a certain cycle when the phase hardening saturates, the plastic relaxation also saturates.

4. The residual acoustic emission accompanying the direct transformation and especially the acoustic emission accompanying the reverse martensitic transformation are no

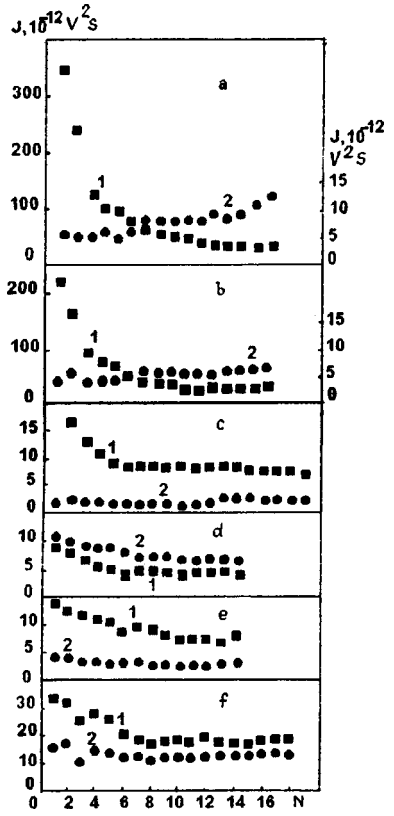

FIG. 1. Fragments of acoustic curves (*1*) for $Ti_{0.5}Ni_{0.5-x}Cu_x$ alloys ($2 \leqslant x \leqslant 11.0$ at.%): a, b — emission asymmetry of the first type in alloys containing 2.0 and 4.0 at.% Cu for B2→B19′ and B19′→B2 transformations; c — emission asymmetry of the first type in an alloy containing 8.0 at.% Cu for B2→B19 and B19→B2 transformations; d, e, f — nearly symmetric acoustic emission in alloys containing 9.0, 10.0, and 11.0 at.% Cu for the B2→B19 and B19→B2 transformations. Curve *2* is the temperature curve.

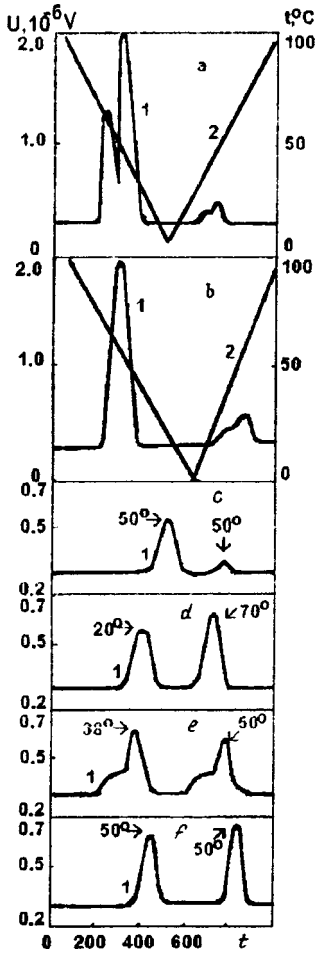

FIG. 2. Influence of cycling of martensitic transformations in alloys on the acoustic emission: a, b — inversion of the first type of acoustic emission asymmetry to the second type in alloys containing 2.0 and 40.0 at.% Cu; c — conservation of the emission asymmetry in an alloy containing 8.0 at.% Cu; d, e, f — conservation of emission symmetry in alloys containing 9.0, 10.0, and 11.0 at.% Cu. *1* — for the direct transformation, *2* — for the reverse transformation; *N* — cycle number.

longer related to the plastic relaxation and are of a different nature. For instance, in Au–Cd alloys the acoustic emission accompanying the reverse martensitic transformation is attributed to scattering of the so-called configurational energy accumulated during the direct transformation.[5] The acoustic emission accompanying the direct transformation is caused by the formation of a martensitic boundary, its interaction with local obstacles, and its emergence at the crystal surface.

The mechanism for the production of acoustic emission following degradation of the plastic relaxation of the microstresses will be called dynamical relaxation of nonchemical energy where dynamical relaxation implies a specific mechanism for the scattering of the nonchemical energy of the martensitic transformation.

5. In the second group of alloys in which no phase hardening is observed (no plastic relaxation of microstresses occurs), from the first martensitic transformation cycle we do in fact observe ''pure'' acoustic emission caused by the dynamical relaxation of nonchemical energy. This dynamical mechanism of acoustic emission appears explicitly when the macroscopically explosive kinetics of a martensitic transformation is modeled.[6]

The specific characteristics of the dynamical relaxation of nonchemical energy in these alloys (Table I) are attributable to the microexplosive kinetics of the appearance and disappearance of martensite crystals of finite dimensions in contrast to the microkinetics of slow growth and contraction of martensite crystals in the first group of alloys. Another factor is the correlation (autocatalysis) of the process of formation and disappearance of groups of martensite crystals,[7] as is evidenced by the high value of the parameter dY/dT, which is three times the value for the first group of alloys. It should also be borne in mind that under conditions where martensite crystals of finite dimensions appear spontaneously, no nonchemical energy accumulates, the reverse transformation takes place at the minimum elastic energy,[8] and also the motion of the interphase boundary is accompanied by an anomalous reduction in the elastic moduli.[9]

6. The above-barrier nature of the martensitic transformations presupposes that the interphase boundary migrates at a velocity no lower than the propagation velocity of the elastic waves in this crystalline medium.[10] This implies only one nonradiative migration regime for the interphase boundary at a velocity equal to that of the transverse wave $c_t^2=(C_{11}-C_{12})/2\rho$ in cubic crystals[11] which determines a B2→B19 transformation in the model of displacement wave locali-

TABLE I. Kinetic characteristics of martensitic transformations in ternary Ti(NiCu) alloys.

Alloys, copper content, at. %	Martensitic transformations: Microkinetics of transformations	Hysteresis, °C	dY/dt, 1/°C	Acoustic emission: Initial asymmetry	Evolution of asymmetry
2.0	Slow growth-contraction for B2→B19′ and B19′→B2	30	0.17	Type 1	Type 1 → type 2
4.0		25	0.17	as above	as above
8.0	Microexplosive for B2→B19→B19	8	1.0	Type 1 asymmetry	Asymmetry conserved
9.0	Microexplosive	8	0.5	Nearly	Symmetry
10.0	at stage	10	0.5	symmetric	conserved
11.0	B2→B19 and B19→B2	10	0.25		

zation.[9] The energy of the interphase boundary (in fact the nonchemical kinetic energy) is expended in exciting the crystalline medium and stimulating a martensitic transformation in a neighboring crystallite. The martensitic transformation process then becomes self-accommodating (autocatalytic).

The nonradiative migration of the martensite boundary is destroyed when the self-accommodating (conservative[12]) behavior of the martensitic transformation is impaired (in the broad sense when the coherence is lost[13]). In this case, the acoustic signal is spontaneous bremsstrahlung. This interaction clearly reduces the velocity of the interphase boundary to zero.

The nonradiative motion can also be impaired if the velocity V of the martensite boundary exceeds the velocity of the transverse waves c_t, i.e., $V/c_t>1$. This situation occurs when the elastic moduli decrease near the interphase boundary running toward the crystallite interface, which is characterized by a jump in the phase propagation velocity of the transverse waves. Each martensite crystal then produces spontaneous transition radiation when it interacts with the boundary and the set of martensite crystals formed by autocatalysis is a system of coherent emitters whose degree of coherence increases as the perfection of the martensitic structure increases. The spontaneous acoustic signal occurs as acoustic transition radiation, which is an analog of the optical transition radiation in a nonsteady-state medium.[14]

TABLE II. Mechanical characteristics of ternary Ti(Ni,Cu) alloys.

Alloy	Yield point, MPa	Martensitic shear stress, **	Stress difference: $\Delta\sigma_s$, MPa	$(\sigma_s-\sigma_m)$, MPa
5. 2 at. % Cu	450	210	100	240
6. 4 at. % Cu	430	120	90	300
7. 6 at. % Cu	380	100	70	280
8. 8 at. % Cu	380	50	40	330
9. 9 at. % Cu	250	35	0	215
10. 10 at. % Cu	250	35	0	215
11. 11 at. % Cu	250	35	0	215

Note: in Table II σ_s is the yield point, σ_m is the martensitic shear stress, and $\Delta\sigma_s$ is the increase in the yield point as a result of martensitic transformation cycling.

These two variants for the production of acoustic emission differ substantially, but this does not exclude the formation of the acoustic signal as a combination of transition radiation and bremsstrahlung.

If the condition $V/c=1$ is reliably satisfied for reversible martensitic transformations, the acoustic emission occurs as bremsstrahlung when the velocity V decreases to zero. Quite clearly, only symmetric acoustic emission can occur in this case.

If the condition $V/c>1$ is satisfied, asymmetric acoustic emission may be observed because of the production of spontaneous transition radiation, which depends strongly on the specific features of the direct and reverse martensitic transformation.

[1] V. A. Plotnikov and Yu. I. Paskal', Fiz. Met. Metalloved. **84**(3), 3 (1997).
[2] V. A. Plotnikov, L. A. Monasevich, V. É. Gyunter, and Yu. I. Paskal', Dokl. Akad. Nauk SSSR **290**, 110 (1986) [Sov. Phys. Dokl. **31**, 755 (1986)].
[3] V. A. Plotnikov, L. A. Monasevich, and Yu. I. Paskal', Fiz. Met. Metalloved. **63**, 757 (1987).
[4] V. A. Plotnikov, L. A. Monasevich, and Yu. I. Paskal', Fiz. Met. Metalloved. **65**, 1219 (1988).
[5] J. Barom, J. Avissar, and Y. Gefen, Scr. Metall. **14**, 1013 (1980).
[6] V. A. Plotnikov, Pis'ma Zh. Tekh. Fiz. **24**(1), 31 (1998) [Tech. Phys. Lett. **24**, 14 (1998)].
[7] V. Ya. Erofeev and Yu. I. Paskal', Dokl. Akad. Nauk SSSR **286**, 879 (1986) [Sov. Phys. Dokl. **31**, 162 (1986)].
[8] Yu. I. Paskal', V. Ya. Erofeev, and L. A. Monasevich, Metallofizika (Kiev) **6**(6), 36 (1984).
[9] V. N. Khachin, Izv. Vyssh. Uchebn. Zaved. Fiz. **5**, 88 (1985).
[10] Yu. I. Paskal', V. A. Plotnikov, and L. A. Monasevich, Deposited Paper No. 5161–V89, VINITI (1989), 48 pp.
[11] W. A. Wooster, *Tensors and Group Theory for the Physical Properties of Crystals* (Clarendon Press, Oxford, 1973; Nauka, Moscow,1977, 384 pp.).
[12] V. A. Plotnikov and Yu. I. Paskal', Izv. Vyssh. Uchebn. Zaved. Fiz. **5**, 49 (1997).
[13] L. A. Shelepin, *Coherent Physics and Its Application. Coherent Cooperative Phenomena* [in Russian], Nauka, Moscow (1976), pp. 3–20.
[14] V. L. Ginzburg and V. N. Tsytovich, Usp. Fiz. Nauk. **126**, 353 (1978) [Phys. Rep. **49**, 1 (1979)].

Translated by R. M. Durham

Impact-resistant high-temperature superconductor

J. N. Anneli and M. M. Bolotashvili

Institute of Mechanics of Machines, Georgian Academy of Sciences, Tbilisi
(Submitted December 21, 1998)
Pis'ma Zh. Tekh. Fiz. **25**, 23–26 (July 12, 1999)

A method of fabricating a high-temperature superconducting ceramic is proposed and described. This method can produce a material having a higher impact strength and lower degradation in air than that obtained by other methods. © *1999 American Institute of Physics.* [S1063-7850(99)00507-8]

At present the most thoroughly studied class of high-temperature superconductors (HTSCs) is $MeBa_2Cu_3O_{7-x}$, where Me is a rare-earth metal. Methods of fabricating these materials are fairly varied and their properties have been optimized. However, a common disadvantage of these HTSCs is frequently their increased brittleness and loss of superconducting properties on exposure to atmospheric gases and moisture during storage, which to some extent limits their range of practical application.

In many studies high-molecular compounds have been used to improve the mechanical properties of HTSCs. For instance, Graboĭ and Kaul'[1] proposed a method of fabricating current-carrying thin fibers using a highly loaded stabilized suspension of $YBa_2Cu_3O_{7-x}$ superconducting ceramic powder in an aqueous solution of polyvinyl alcohol. The suspension was stabilized using oxyethylene polyethers. The percent by weight of superconducting powder in the fibers was 93%. The polymer component of the fibers was burnt out by heat treatment at 453–753 K and the residual oxide particles were sintered at 980 °C for 5 min in an oxygen stream. The fibers obtained exhibited a superconducting transition near 84 K but were highly brittle. In Ref. 2 HTSCs were fabricated by pressing with 0.02–0.05 m.u. of organic plasticizer mass added to the ceramic powder to improve the regrouping efficiency of the HTSC ceramic particles. The resulting mass was pressed into special shapes and then sintered to produce a high-temperature superconductor. Although methods of obtaining HTSCs using organic substances have some advantages,[1,2] they also have various disadvantages, the main one being their comparatively low impact strength. In addition, these materials change their properties on exposure to water vapor and carbon dioxide.

In order to improve the specific impact strength and prevent any degradation of the material under atmospheric conditions, we developed a method of two-stage annealing of a mixture containing the familiar superconducting powder $YBa_2Cu_3O_{7-x}$ and various organic high-molecular compounds such as KO-812 organosilicon lacquer, ÉD-20, 4,4′-isopropylenediphenol epoxy resin, and phenolformaldehyde resin (PFR). The HTSC samples were obtained by the following method.

High-molecular compounds taken in the weight percent ratio specified in Table I were thoroughly mixed in acetone and $YBa_2Cu_3O_{7-x}$ powder was then added. The mixture was mixed again and then dried at room temperature and atmospheric pressure for 2 h. The dry mixture was then placed in a steel mold and held for 1 h at 100 MPa with the temperature increased to 353–393 K. After 1 h the samples were removed and placed in a thermostat for annealing in vacuum. The samples were heated gradually to prevent cracking from the thermal impact. The samples were annealed for 2 h at 973 K in vacuum down to 10 kPa, after which the furnace was switched off and the samples cooled down inside the furnace for 2 h. The samples were removed from the thermostat after 16–18 h and were placed in a muffle furnace for annealing at 1223 K in an oxygen atmosphere for 4 h. The samples then cooled down with the furnace for 20–24 h. The materials thus obtained have an increased impact strength whose values are given in Table I.

According to the tabular data, if a polymethyl sesquisiloxane ladder oligomer combined with epoxy and phenol-formaldehyde resins are incorporated in a specific ratio in the technological cycle to produce $YBa_2Cu_3O_{7-x}$ high-temperature superconductors, this can produce materials having a generally high impact strength. In particular, this strength is increased by almost an order of magnitude if the mixture contains the components $YBa_2Cu_3O_{7-x}$, KO-812, and ÉD-20 + phenolformaldehyde resin in the ratio 90.0:7.0:3.0.

An explanation for these experimental results must be sought primarily in the characteristics of formation of the final structure, which depends not only on the choice of initial mixture components but also on the heat treatment regime.

A comparison between the electrophysical characteristics of pure $YBa_2Cu_3O_{7-x}$ and our composite based on this shows that the superconducting transition temperatures of both materials are the same (83 K). We can therefore conclude that the structures responsible for the superconducting states in the pure superconductor and the composite are the same.

In this case, in our view, one possible variant for the structure of the composite is a configuration in which the well-known structure[2] of the HTSC ceramic $YBa_2Cu_3O_{7-x}$ is combined with a framework of Si, C, and O atoms formed after high-temperature annealing of the high-molecular compounds used under the conditions described above.

Anneli *et al.*[3] showed that heat treatment of these high-molecular compounds under similar conditions results in a

TABLE I. Composition (m.u.) and specific impact strength of new high-temperature superconductors.

No.	$YBa_2Cu_3O_{7-x}$	KO-812	ÉD-20/PFR 65/35	Specific impact strength kgf·m/cm^2
1	98.5	135	0.15	0.18
2	98.5	1.05	0.45	0.27
3	98.5	0.75	0.75	0.23
4	95.0	4.5	0.5	0.57
5	95.0	3.5	1.5	0.81
6	95.0	2.5	2.5	0.71
7	90.0	9.0	1.0	0.70
8	90.0	7.0	3.0	0.93
9	90.0	5.0	5.0	0.82
10	100	0	0	0.1

strong molecular framework constructed of the chemically bound silicon, carbon, and oxygen atoms left after annealing. In particular, it was shown that pyrolysis of polymethyl sesquisiloxane results in the formation of a cubic structure whose edge is formed by Si–O–Si bonds while the pyrolysis of phenolformaldehyde and epoxy resins leads to the formation of graphite-like structures.

The existence of this framework probably helps to reduce cracking and therefore improves the strength properties and monolithic quality of the entire HTSC composite.

At the same time, a reduction in the number of cracks and various structural defects through which gases may diffuse is clearly responsible for the enhanced stability of the composite in atmospheric gases when the samples are stored in air for at least a year.

It should be noted that the technology for fabricating HTSCs incorporating high-molecular compounds can be used to produce samples of large dimensions.

[1] I. É. Graboĭ and Yu. G. Kaul', Itogi Nauki i Tekhniki (Khimiya Tverdogo Tela) **6**, 144 (1989).
[2] *Chemistry of High-Temperature Superconductors*, edited by D. L. Nelson, M. S. Whittingham, and T. F. George (American Chemical Society, Washington, 1988; Mir, Moscow, 1988, 280 pp.).
[3] J. N. Anneli, L. M. Khananasvili, and G. E. Zaikov, *Structuring and Conductivity of Polymer Composites* (Nova Science Publishers, New York, 1998), p. 185.

Translated by R. M. Durham

Microwave and rf excitation of a discharge in sulfur vapor with added neon

A. N. Kozlov, G. A. Lyakhov, Yu. V. Pavlov, A. E. Reznikov, R. M. Umarkhodzhaev, and E. D. Shlifer

Scientific Center of Wave Research, Institute of General Physics, Russian Academy of Sciences, Moscow
(Submitted November 2, 1998)
Pis'ma Zh. Tekh. Fiz. **25**, 27–33 (July 12, 1999)

An experimental investigation was made of the transient emission of a discharge excited by microwave radiation in mixtures of sulfur and rare gases. Several typical spectral types of emission were identified which alternate over time. © *1999 American Institute of Physics.*
[S1063-7850(99)00607-2]

1. The electrodeless system for excitation of a gas discharge using an external electromagnetic field was developed far later than the classical system with an external current source.[1] It proved fruitful to consider the microwave range and this was promoted by previous developments of powerful, economical, microwave sources. At the same time, it was established that electromagnetic wave energy in this range can be efficiently converted into kinetic energy of ionized gas particles and then into radiation energy.

Probably the most advanced application so far is a powerful efficient light source with a high-quality radiation spectrum[2] (for a detailed system see Ref. 3).

This system includes a magnetron whose cavity contains a sealed quartz envelope containing sulfur (and/or selenium) powder and a low-pressure buffer gas (argon). The physical mechanisms for the excitation of a discharge in this system were broadly established by Warmby.[4] The microwave field induces a glow discharge in the buffer gas, which has a low breakdown threshold at low initial pressure. At the same time, the field heats the sulfur powder until it vaporizes. In the high-pressure gas mixture thus formed, the microwave field converts the sulfur atoms (and also dimers, and so on) to excited states. This is accompanied by a direct atomic and molecular absorption channel and a collisional mechanism. Finally, reemission from excited states forms the observed emission spectrum.

Extremely detailed experimental measurements have been made of the energy balance for this new light source.[5] However, this set of data which, significantly, applies to the steady-state regime, is insufficient to formulate a quantitative model. A general theory needs to be constructed, not only to optimize this promising prototype for a whole range of devices, but also from the general plasma physics point of view. The processes determining the efficiency of a microwave discharge in this type of mixture are typical of both a low-pressure glow discharge and breakdown at high pressure. On the one hand, this complicates the problem (it is impossible to identify parameters that stay small during the entire process) and on the other hand, it extends the range of possible applications.

The obvious next step toward solving this problem is to investigate the evolution kinetics of a microwave discharge. The various elementary processes contributing to its evolution generally have different intensities and rates of establishment, so that separating these in time would at least yield estimates of the relative values of these characteristic parameters.

The aim of the present paper was to observe the transient emission pattern for a discharge excited by microwave radiation in mixtures of sulfur and rare gases. In fact we succeeded in identifying a number of characteristic spectral types of discharge emission which alternate over time.

2. The first series of measurements was made using a mixture of sulfur and neon at a high microwave excitation power. This provided conditions similar to the operating conditions of a light source.[2] Neon was selected as the buffer gas because its characteristic lines are widely displaced from the sulfur lines.

A 30 mm diameter spherical quartz envelope filled with neon at 4 Torr pressure and 30 mg of sulfur powder was placed in the cavity of a waveguide system excited by an M-155 magnetron. The magnetron radiation power at 2.45 GHz was 800 W. The spectral measurements were made using an SP40 spectrograph with an operating range of 3600–12 500 Å. The nonuniformity parameters of the sensitivity curve are: 10% nonuniformity at 11 000 Å and 70% at 3600 Å.

In the measurements the temperature of the outer surface of the envelope played the role of the timelike parameter in the kinetics. Its relationship with the real time during heating of the mixture by the microwave radiation is nonlinear but single-valued. This procedure was used because the time scales of the kinetics of the spectral composition of the emission differ substantially at the various stages of variation in the qualitative pattern of the spectrum. The kinetics includes both smooth (on scales of the order of 100 s) and abrupt changes (over times shorter than a tenth of a second). The temperature of the outer surface of the envelope was measured using a ''Kel'vin'' laser-directed remote pyrometer having a working range of 50–1000 °C. The relative error of the temperature measurements under the experimental conditions, where the heat flux was recorded from a region at least 20 mm in diameter, is better than ± 1 °C. The absolute error at high temperatures reaches $\pm 3-5\%$ because of the inaccuracy in determining the emissivity of the surface.

A second series of measurements was carried out to

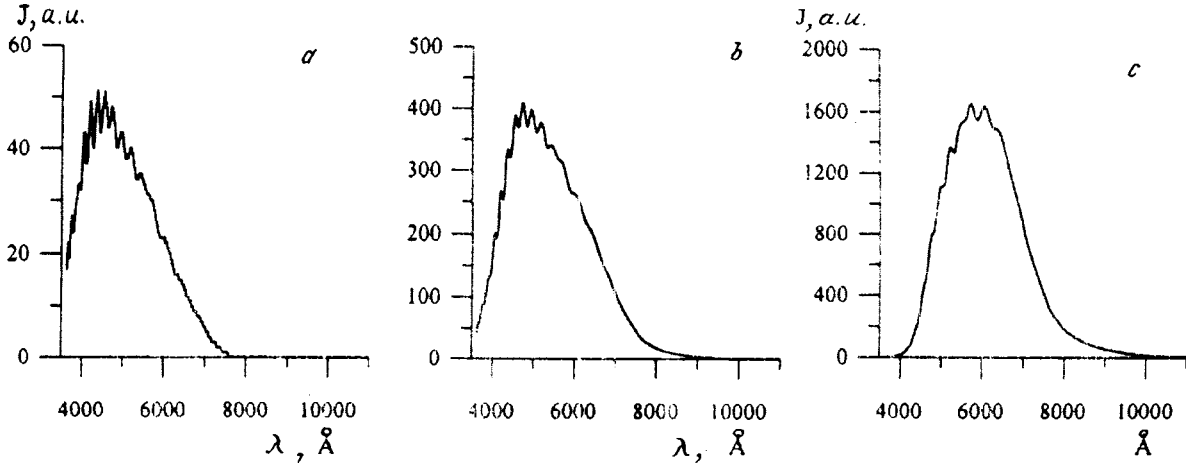

FIG. 1. Luminescence spectra of a discharge excited by high-power (800 W) microwave (2.45 GHz) radiation in a sulfur + neon mixture. The temperature of the outer surface of the envelope is 450 (a), 580 (b), and 640 °C (c).

make more detailed observations. Instead of using a magnetron, the electromagnetic excitation of the discharge was provided by a longer-wavelength (operating frequency 100 MHz), less powerful (100 W) generator inductor.

3. In a series of spectral measurements using a high-power microwave excitation field, the evolution of the emission in a sulfur + neon mixture reveals three stages (Fig. 1).

1) Almost as soon as the microwave radiation is supplied, a relatively low-intensity glow appears in the gas mixture. The maximum spectral intensity lies around 4500 Å (Fig. 1a) and the spectrum extends, at half maximum, between 3700 and 5900 Å.

2) When the temperature of the outer surface of the envelope reaches approximately 500 °C, the maximum intensity of the emission increases by a factor of 7–9. The spectral maximum is shifted toward 4700 Å and the spectrum occupies the range between 3900 and 6500 Å (Fig. 1b).

3) The second jump, at around 600 °C, forms a quasisolar spectrum (Fig. 1c). The maximum intensity increases by a further factor of 3–5. The poorly defined maximum lies around 5800 Å and the half-width is around 2400 Å.

4. A reduction in the frequency and power of the electromagnetic excitation can slow the evolution of the discharge in the same sulfur + neon mixture. The more detailed pattern of variation in the spectral composition of the emission observed in this case includes additional characteristic stages whose lifetime in a high-power field does not exceed a fraction of a second.

1) In a cold envelope (at temperatures below 35–40 °C), a characteristic set of neon lines is emitted with the highest-intensity line at 6400 Å (Ref. 6). The lamp emits a high-intensity red-orange light (Fig. 2a).

2) The discharge in the neon buffer heats the envelope to temperatures above 45 °C, simultaneously creating an appreciable concentration of sulfur vapor. The neon lines are suppressed relative to the rapidly growing 9200 Å line of atomic sulfur[6] (Fig. 2b).

3) The 9200 Å atomic sulfur line is suppressed as soon as the envelope temperature exceeds approximately 65 °C. At the same time, the visible radiation band increases from 4500 to 6500 Å and the 4690 Å sulfur line[6] appears (Fig. 2c). A blue halo appears which changes into a stable bluish-white glow.

4) As the envelope temperature increases to 120–130 °C, the intensity of the bluish white glow drops rapidly. The emission spectrum (Fig. 2d) shifts toward the blue and the ultraviolet (and there is a characteristic smell of ozone). The 9200 Å line almost disappears while the 4690 Å line can still be discerned against the background of the molecular spectrum.

5) At around 160 °C the discharge is quenched and the generator-inductor power must be increased to sustain it. The discharge quenching temperature depends on the generator power and on the size of the envelope. At constant power, the quenching temperature increases as the volume of the envelope decreases.

5. The evolution of emission in a sulfur + argon mixture excited by a low-intensity rf field is broadly the same as the discharge pattern with a neon buffer.

At envelope temperatures up to 60 °C the well-known argon lines at 7630, 8100, and 8400 Å are present[6] together with the atomic spectrum of sulfur. This quantitative difference from the initial stage of the discharge in neon indicates that argon is more efficient as a buffer. As the temperature increases, the argon lines become less intense, whereas lines of the molecular spectrum of sulfur appear in the ultraviolet. This indicates that in the presence of argon sulfur vaporizes more efficiently than in neon and the short-wavelength part of its spectrum is excited. This process is evidently responsible for the formation of the quasisolar spectrum at high levels of microwave excitation.

6. In our view, these results substantially extend the set of experimental data required to construct a quantitative model of a discharge excited by an electromagnetic field in the 0.1–10 GHz range in a mixture of a low-pressure buffer gas and a vaporizable component having an advanced emission spectrum in the visible range. In view of the obvious complexity of the system, it is unproductive to formulate the theoretical description problem using exact rate equations. However, known data on the parameters of a steady-state

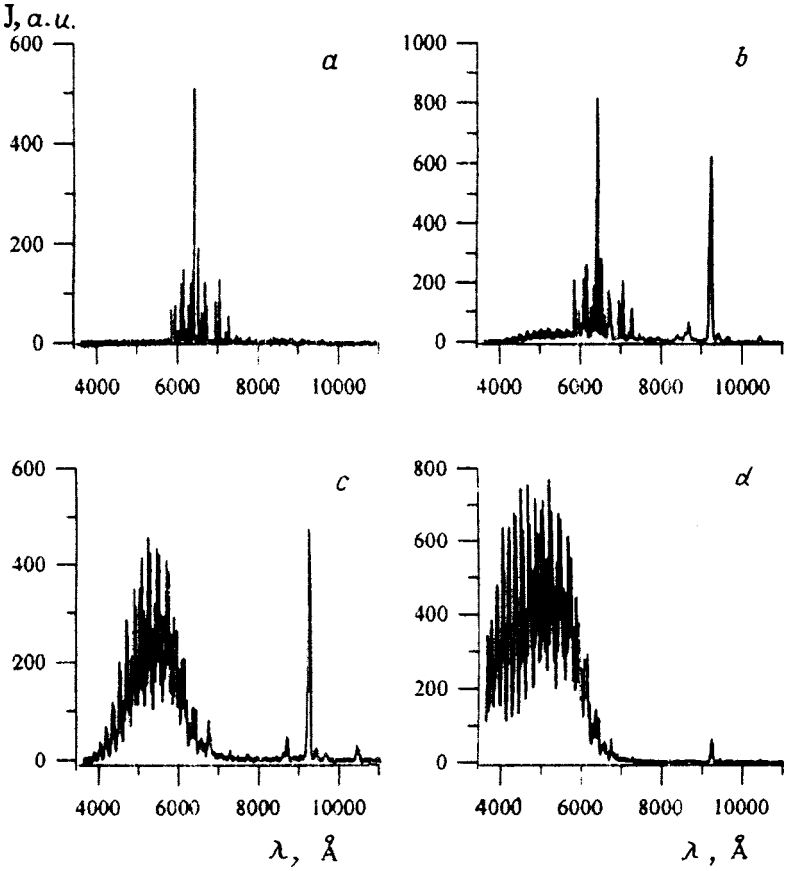

FIG. 2. Luminescence spectra of a discharge in a relatively low-power (100 W), rf (100 MHz) field. The temperature of the envelope surface is 34 (a), 55 (b), 78 (c), and 145 °C (d).

discharge are insufficient even to optimize the electromagnetic source in terms of frequency, the geometry of the gas volume, and the component composition of the mixture. This optimization problem for which a solution, at least in terms of frequency, was indicated in Ref. 7 has in fact not yet been formulated. In particular, the choice of wavelength in the series of studies beginning with Ref. 2 was based on economic factors.

These data can be used to select the most effective energy transfer channels at each discharge stage and to estimate, at least approximately, the rates of energy transfer and the corresponding saturation levels. Quite clearly, these data should be recalculated because of the nonlinear time dependence of the temperature at the surface of the discharge envelope. The corresponding theoretical problem can already be formulated.

[1] Yu. P. Raĭzer, *Gas Discharge Physics* (Springer-Verlag, New York, 1991) [Russ. original, Nauka, Moscow, 1992).
[2] J. T. Dolan, M. G. Ury, and C. H. Wood, in *Sixth International Symposium on the Science and Technology of Light Sources*, (Budapest Technical University Press, 1992), pp. 301–302.
[3] J. T. Dolan, M. G. Ury, and C. H. Wood, *Lamp Including Sulfur* US Patent No. 5404076 (1995).
[4] D. O. Warmby, IEE Proc. A **140**, 465 (1993).
[5] D. A. Maclennan, J. T. Dolan, and M. G. Ury, in *Digest of Technical Papers of the Society for Information Display International Symposium*, 1992. Vol. 23, pp. 460–463.
[6] A. N. Zaĭdel', V. I. Prokhorov, S. M. Raĭskiĭ, and E. Ya. Shreĭder, *Tables of Spectral Lines* [in Russian], Fizmatgiz, Moscow (1962).
[7] A. N. Didenko, E. A. Vinogradov, G. A. Lyakhov, and K. F. Shipilov, Dokl. Ross. Akad. Nauk **334**(2), 182 (1995).

Translated by R. M. Durham

Influence of self-oxide formation regimes on the properties of oxide–*p*-InSe heterojunctions

V. N. Katerinchuk, Z. D. Kovalyuk, and A. V. Zaslonkin

Institute of Problems in Materials Science, Ukrainian National Academy of Sciences, Chernovtsy
(Submitted January 18, 1999)
Pis'ma Zh. Tekh. Fiz. **25**, 34–36 (July 12, 1999)

Oxide–*p*-InSe heterojunctions were formed by thermal oxidation of a *p*-InSe crystal substrate in various temperature–time regimes. Measurements of the current–voltage characteristics confirmed that these were of good optical quality. The optimum technological conditions for fabricating these junctions were determined. © *1999 American Institute of Physics.* [S1063-7850(99)00707-7]

In earlier studies[1,2] we showed that the oxidation of indium monoselenide leads to the formation of a self-oxide on its surface, having properties similar to those of In_2O_3. Possessing both high conductivity and transparency, this oxide film only forms a heterojunction with *p*-type InSe crystals. No energy barrier is formed at the heterojunction with *n*-type InSe.

We used a method of nonstoichiometric InSe growth[3] and doping with cadmium impurities[4,5] to obtain *p*-type InSe crystals.

The as-grown *p*-InSe ⟨Cd⟩ crystals were oxidized in air for 1, 5, 10, 20, and 50 min at temperatures of 200, 300, 400, and 500 °C, using three samples for each oxidation regime. After the oxidized samples had been cut and cleaved, contacts were deposited on them. We then measured the photo-emf for these self-oxide–*p*-InSe heterojunctions at an illumination intensity of $\sim 100\,\mathrm{mW/cm^2}$. The results of the measurements are presented in Table I, which only includes those samples which possessed the maximum open-circuit voltage.

Table I shows that no large differences are observed in the value of U at different temperatures, although the oxidation time differs substantially.

In order to determine how the heterojunction formation regimes influence their quality, we investigated the current–voltage characteristics of forward-biased samples. As we know,[6] in this case the relationship between the current and voltage is exponential and the maximum exponent is observed for ideal diodes, i.e., when the ideality factor is $n=1$. Deviations from an ideal current–voltage characteristic are observed a) when the mechanism of current flow across the $p-n$ junction changes, b) as a result of the influence of shunting currents induced by barrier defects, and c) as a result of the presence of a dielectric layer. In each of these cases we find $n>1$.

Figure 1 shows the forward branches of the current–voltage characteristics of the heterojunctions whose photoelectric parameters are given in Table I. It can be seen that in a semilogarithmic plot these branches are linear with two slopes, each characterized by the value of n indicated in the figure. The curves of $I(U)$ described by $n=1$ correspond to the diffusion mechanism of current flow through the barrier and $n=2$ corresponds to the recombination mechanism. However, if diffusion and recombination currents flow simultaneously, this may lead to $1<n<2$. The existence of both mechanisms of current flow through the heterojunction (in particular for samples oxidized at 300 °C) and the transition from a recombination current to a diffusion current indicates that the samples are of good quality. Such a transition

TABLE I. Maximum open-circuit voltage of self-oxide–*p*-InSe heterojunctions under various conditions of formation.

t, °C	200	300	400	500
t, min	10	5	5	1
U, V	0.41	0.53	0.44	0.49

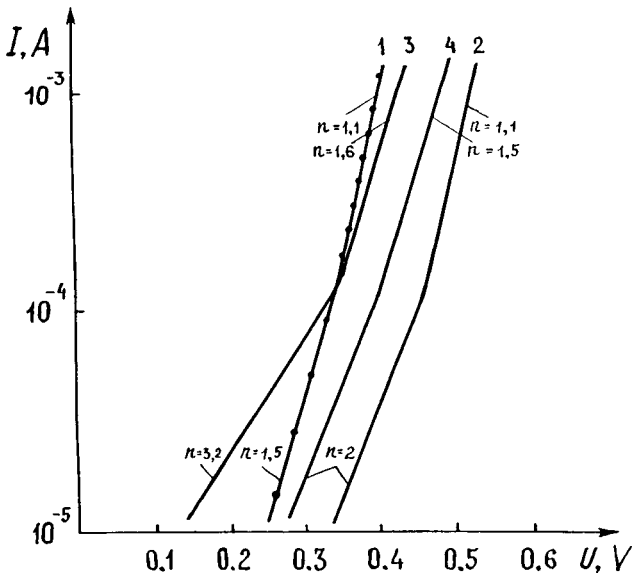

FIG. 1. Forward branches of the current–voltage characteristic of oxide-*p*-InSe heterojunctions at room temperature: *1* — 200 °C, 10 min; *2* — 300 °C, 5 min; *3* — 400 °C, 5 min; *4* — 500 °C, 1 min.

is observed in diffusion silicon diodes.[6] In this case factors b) and c) may arise but they are not important. Heterojunctions with $n = 1.5–1.6$ and $n = 3.2$ are of lower quality. In this last case, for $n > 2$ the current–voltage characteristic is caused by leakage currents.

To sum up, we have established as a result of these investigations that thermal oxidation of layered *p*-InSe crystals can produce high-quality heterojunctions and we have determined the optimum conditions for forming them.

[1] V. N. Katerinchuk and M. Z. Kovalyuk, Pis'ma Zh. Tekh. Fiz. **18**(12), 70 (1992) [Sov. Tech. Phys. Lett. **18**, 394 (1992)].
[2] V. N. Katerinchuk and M. Z. Kovalyuk, Pis'ma Zh. Tekh. Fiz. **23**(10), 1 (1997) [Tech. Phys. Lett. **23**, 377 (1997)].
[3] A. Chevy, A. Kuhn, and M.-S. Martin, J. Cryst. Growth **38**, 118 (1977).
[4] A. Chevy, J. Appl. Phys. **56**, 978 (1984).
[5] G. Micocci, M. Molendini, and A. Tepore, J. Appl. Phys. **70**, 6847 (1991).
[6] S. Sze, *Physics of Semiconductor Devices* (Wiley, New York, 1969; Vol. 1, Nauka, Moscow 1984, 456 pp.).

Translated by R. M. Durham

Suppression of parasitic backgating by hydrogenation of ion-doped gallium arsenide structures

V. A. Kagadeĭ, Yu. V. Lilenko, L. S. Shirokova, and D. I. Proskurovskiĭ

State Scientific-Industrial Organization ''Research Institute of Semiconductor Devices,'' Tomsk
Institute of High-Current Electronics, Siberian Branch of the Russian Academy of Sciences, Tomsk
(Submitted February 7, 1999)
Pis'ma Zh. Tekh. Fiz. **25**, 37–41 (July 12, 1999)

It has been established that hydrogenation of ion-doped gallium arsenide structures can be used to suppress parasitic backgating. Curves describing the degree of suppression of the backgating as a function of the hydrogenation regimes are given. The observed dependence is evidently caused by the formation and decay of hydrogen complexes with deep centers.
 [S1063-7850(99)00807-1]

It is generally assumed that parasitic backgating in GaAs is attributable to the influence of deep centers in the bulk of the semiinsulating substrate and/or at the interface between the active *n*-layer and the semiinsulating substrate. The nature of these centers is not completely clear.[1,2]

One method of reducing the negative influence of backgating on the operation of transistors in integrated circuits is local implantation of Be^+ ions needed to form *p*-pockets beneath the *n*-type channel of the transistor. In this way the transistor channel is isolated from the influence of the substrate.[3] Another method of suppressing backgating may involve passivating the electrically active deep centers responsible for the effect. We know[4,5] that hydrogenation in atomic hydrogen passivates many shallow and deep centers in single-crystal Si and GaAs. However, very few detailed studies have been made of the hydrogenation of ion-doped GaAs structures, and the possibility of reducing backgating has not been studied at all. In the present study the possibility of suppressing backgating by using hydrogenation is confirmed experimentally for the first time.

The investigations were carried out using n^+-n-type structures fabricated by implanting Si^+ ions in semiinsulating GaAs substrates. The electron concentration n_e in the contact n^+ layer was $(1.5–2)\times10^{18}\,\mathrm{cm}^{-3}$ and that in the active *n* layer was $3\times10^{17}\,\mathrm{cm}^{-3}$. From the batch of fabricated structures we selected samples exhibiting the maximum gating effect. These samples were hydrogenated in atomic hydrogen using a system described in Refs. 6 and 7. The temperature of the samples during hydrogenation was $T=100–300\,^\circ\mathrm{C}$, the treatment time was $t=5–90$ min, and the hydrogen pressure 10^{-2} Pa. The electron concentration n_e in the ion-doped layer was determined from capacitance–voltage measurements using a system with a mercury probe. The parasitic backgating was estimated using a method proposed in Refs. 8 and 9, which is based on the fact that the degree of variation in the resistance of a semiconductor structure when bias voltages are applied to it is directly proportional to the backgating. A bias voltage was applied to the contact n^+ layer and the resistance of the structure was measured using a noncontact method for which the structure was inserted in a 38 GHz microwave resonator. The change in the resistance of the structure was determined from the change in the microwave power *P* reflected from the resonator. Thus, by measuring the change in the power *P* when a bias is

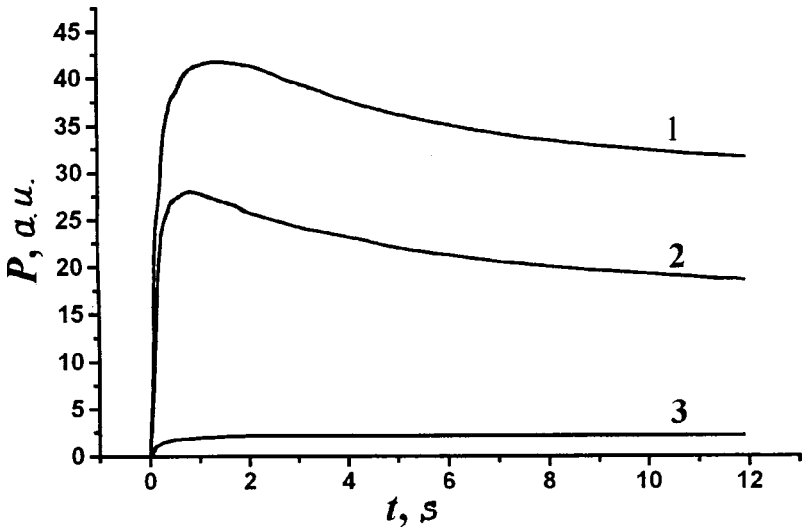

FIG. 1. Power *P* reflected from microwave resonator versus time *t* when a bias voltage is applied to the initial sample (1) and after the sample has been hydrogenated and annealed; hydrogenation regime: $T=150\,^\circ\mathrm{C}$, $t=30$ min (2); $T=150\,^\circ\mathrm{C}$, $t=30$ min + $T=200\,^\circ\mathrm{C}$, $t=30$ min (3).

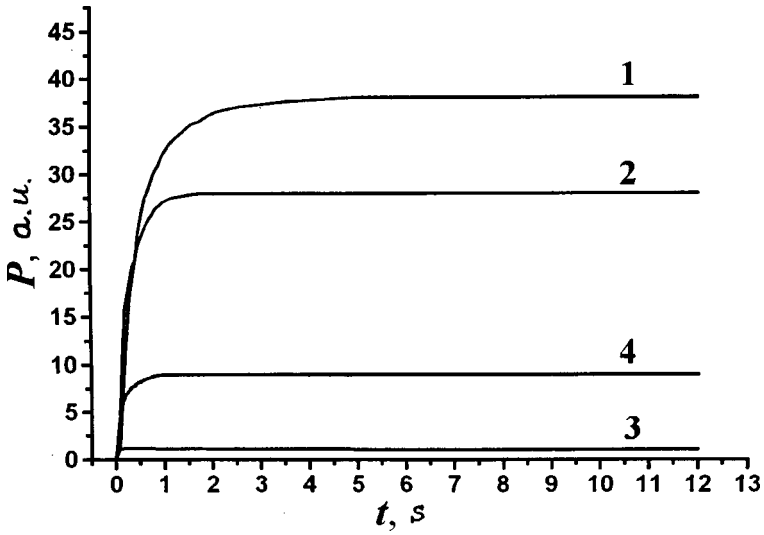

FIG. 2. Power P reflected from microwave resonator versus time t when a bias voltage is applied to the initial sample (1); for the sample after hydrogenation ($T=150\,^{\circ}\mathrm{C}$, $t=30$ min) and annealing at $T^*=400\,^{\circ}\mathrm{C}$, $t^*=5$ min+$T^*=450\,^{\circ}\mathrm{C}$, $t^*=1$ min (2), for the same sample after additional annealing at $T^*=475\,^{\circ}\mathrm{C}$, $t^*=2$ min (3), and for the same sample after additional annealing at $T^*=475\,^{\circ}\mathrm{C}$, $t^*=20$ min (4).

applied, it was possible to estimate the backgating effect.

Measurements of the carrier concentration in the ion-doped layer showed that as a result of hydrogenation n_e decreases from $(1-2)\times10^{18}$ to $10^{17}\,\mathrm{cm}^{-3}$ or less. This indicates that after penetrating into the surface layer of the semiconductor structure, the atomic hydrogen formed electrically neutral complexes with dopant atoms. It is known that hydrogen–shallow-impurity center complexes in GaAs decay at lower temperatures than complexes of hydrogen with deep centers.[10] Consequently, we used low-temperature annealing in the following regime to restore the initial carrier concentration: $T^*=400-475\,^{\circ}\mathrm{C}$, annealing time $t^*=1-10$ min. The measurements made after annealing indicated that the carrier concentration had been almost completely restored.

Figure 1 gives the power P reflected from the microwave resonator as a function of the time t for the initial sample and the sample after hydrogenation and annealing. The origin on the time axis corresponds to when the bias voltage is applied to the n^+-layer. As a result of hydrogenation at $T=150\,^{\circ}\mathrm{C}$ for $t=30$ min and annealing, the initial value of P decreased by $\sim30\%$. Additional hydrogenation at $T=200\,^{\circ}\mathrm{C}$ for $t=30$ min and annealing reduced P by $\sim95\%$ from the initial level. It was established experimentally that the lowest value of P achieved (curve 3) corresponds to a backgating level which has no significant influence on the operation of the integrated circuit.

Additional investigations showed that treatment in atomic hydrogen has a greater influence on backgating as the hydrogenation time increases. The optimum hydrogenation temperature is close to $T=150-200\,^{\circ}\mathrm{C}$. Hydrogenation at lower or higher temperatures has a weaker influence on the electrophysical parameters of the structure.

It is of particular interest to note that in some cases the value of P and hence the degree of suppression of backgating depends not only on the hydrogenation regimes but also on the annealing regimes (Fig. 2). Hydrogenation and subsequent annealing ($T^*=400\,^{\circ}\mathrm{C}$, $t^*=5$ min+$T^*=450\,^{\circ}\mathrm{C}$, $t^*=1$ min) reduced the value of P by $\sim20\%$ of the initial level (curve 2). As a result of additional annealing at $T^*=475\,^{\circ}\mathrm{C}$ for $t^*=2$ min, the backgating effect was almost completely suppressed (the value of P was reduced by $\sim97\%$, curve 3). A series of prolonged annealing gradually increases P (curve 4).

The experimentally observed change in the electrophysical parameters of the ion-doped structures may be caused by the presence of atomic hydrogen in the ion-doped layer, at the doped layer–substrate interface, and/or in the semiinsulating substrate. Parasitic backgating is evidently suppressed by the atomic hydrogen passivation of deep centers responsible for the backgating effect and situated in the GaAs surface layer. The experimentally observed behavior of the backgating as a function of the various regimes is determined by the laws governing the formation and decay of hydrogen complexes with deep centers.

To sum up, we have observed that the hydrogenation of n^+-n ion-doped GaAs structures in atomic hydrogen leads to the suppression of effects clearly caused by the formation and decay of hydrogen complexes with deep centers.

The authors are grateful to G. I. Aĭzenshtat for fruitful discussions.

[1] M. Lee and L. Forbes, IEEE Trans. Electron Devices **ED-37**, 2148 (1990).
[2] N. Goto, Y. Ohno, and H. Yano, IEEE Trans. Electron Devices **ED-37**, 1821 (1990).
[3] D. J. Allstot and P. C. Canfield, IEEE J. Solid-State Circuits **25**, 1544 (1990).
[4] J. Chevallier and M. Aucouturier, Annu. Rev. Mater. Sci. **18**, 219 (1988).
[5] J. W. Corbett, S. J. Pearton, and M. Stavola, *Defect Control in Semiconductors*, edited by K. Sumino (Elsevier, North-Holland, 1990), pp. 53–63.
[6] V. A. Kagadei and D. I. Proskurovsky, J. Vac. Sci. Technol. A **16**, 2556 (1998).
[7] V. A. Kagadeĭ, D. I. Proskurovskiĭ, S. D. Reger, and L. M. Romas', Mikroelektronika **27**(1), 10 (1998).
[8] V. Ya. Prinz, S. N. Rechkunov, and V. A. Samoylov, Inst. Phys. Conf. Ser. **160**, 487 (1997).
[9] V. Ya. Prints, Russian Patent No. 2006984; Byull. Izobret 30.01.1994.
[10] E. M. Omel'yanovskiĭ, F. V. Pakhomov, and F. Ya. Polyakov, Fiz. Tekh. Poluprovodn. **21**, 842 (1987) [Sov. Phys. Semicond. **21**, 514 (1987)].

Translated by R. M. Durham

Natural frequency spectrum of a flat superconducting cable

A. A. Akhmetov, S. S. Ivanov, and I. O. Shchegolev

Joint Institute of High Temperatures, Russian Academy of Sciences, Moscow
(Submitted May 27, 1998; resubmitted January 18, 1999)
Pis'ma Zh. Tekh. Fiz. **25**, 42–47 (July 12, 1999)

A matrix method is used to investigate the current damping process in a flat superconducting cable. A discrete spectrum of natural frequencies is obtained, each determining the rate of exponential damping of the corresponding induced current. Although the number of natural frequencies increases as the size of the cable increases, their spectrum remains finite because the maximum and minimum frequencies tend to finite limits. An analysis is made of the induced currents for the limiting frequencies. It is shown that in the range of minimum natural frequencies the induced currents are long-lived long current loops. At high frequencies the distribution of the induced currents in cable layers is sinusoidal. © *1999 American Institute of Physics.* [S1063-7850(99)00907-6]

Interest in studying the consequences of the penetration of an alternating magnetic field in flat superconducting cables has surged because of undesirable side effects caused by the action of the magnet's self-induced field on the cable.[1,2]

The main difference between the present understanding of the problem[3,4] and the approach adopted in earlier studies[5] is that attempts are made to allow for the translational symmetry of the cable. The latter is an inherent property, since all the properties of a perfect superconducting cable are reproduced with a period equal to its twist pitch. If the cable is imperfect or the alternating magnetic field is inhomogeneous, resonance effects occur along its length and the currents induced by the magnetic field are highly nonuniform.[2–4,6]

A model in which the superconducting strands of a flat cable are represented as linear inductances connected by normal resistances is fairly widely used in the continuous[7,8] and discrete approximation.[3–6] In particular, the continuous approximation is used to calculate the cable time constants τ, of which there are two according to Takács.[8] However, the following analysis indicates that the discrete spectrum is characterized by an entire spectrum of τ. An analysis of this spectrum can reveal many properties of the penetration of an alternating magnetic field into a cable.

The discrete model is shown in the inset to Fig. 1. Here the resistances R are points and L is the inductance of one side of a unit cell of length a formed by two adjacent strands of the upper layer superposed on two adjacent strands of the lower cable layer.[5] We shall assume that the length of a sample fabricated using K strands is finite, and then the set of all the resistances can be represented as a finite matrix $\mathbf{R}$ and the set of all the inductances can be represented as the matrix $\mathbf{L}$, where the order of both square matrices is the same as the number of unit cells of the sample N. All the currents circulating in the unit cells at time t will now be represented as a vector $\mathbf{I}(t)$ of order N. Then, if the field is constant, the damping rate of the currents $\mathbf{I}$ will be determined by the matrix $\mathbf{D}=\mathbf{L}^{-1}\mathbf{R}$ as

$$\dot{\mathbf{I}}=-\mathbf{D}\mathbf{I}. \tag{1}$$

The eigenvalues of the matrix $\mathbf{D}$ are the natural frequencies ν, the reciprocal of τ. The eigenvectors of the matrix $\mathbf{D}$ are the current distributions in the cells $\mathbf{I}_s$ which decay according to the law

$$\mathbf{I}_s(t)=\mathbf{I}_s(0)\exp(-\nu t). \tag{2}$$

There are N natural frequencies of the matrix $\mathbf{D}$, having calculated which it is easy to obtain N values of $\mathbf{I}_s$ and then the currents flowing in the strands.

In order to study the damping of an arbitrary current distribution, the latter should be expanded in terms of the eigenvectors of the matrix $\mathbf{D}$. We shall subsequently use two systems to describe the induced currents: the currents in the strands will be denoted as $i_{k,s}$ where $k[1,K]$ is the number of the strand and s is the position number along the cable (see inset to Fig. 1); the currents in the layers will be denoted as $i_{p,s}$ where $p[1,P]$ is the number of the layer into which the cable is divided by the horizontal lines of the contact resistances.

The ν spectrum was investigated for cables fabricated from four (C4) and six (C6) strands. Figure 1 shows the spectrum of sample C4 $N_n=N_n(\nu)$ where $N_n[1,N]$ is the frequency number. Three regions are clearly visible corresponding to three fundamentally different distributions of the induced currents. The spectrum of cable C6 has five such regions.

We shall examine in greater detail the outermost regions which have common features for the two types of cables. The lowest values of ν are found in steps of similar values, three for C4 and five for C6 (see inset to Fig. 2a). The average values of ν for the first, second, and subsequent steps are in the ratio of the squares of the natural numbers, i.e., 1:4:9:16.... The induced currents $i_{1,s}$ corresponding to the lowest values of ν for the first two steps are shown in Fig. 2a. The induced currents corresponding to the other two values of ν belonging to the same step are similar. It can be seen that the induced currents in the strands form large loops

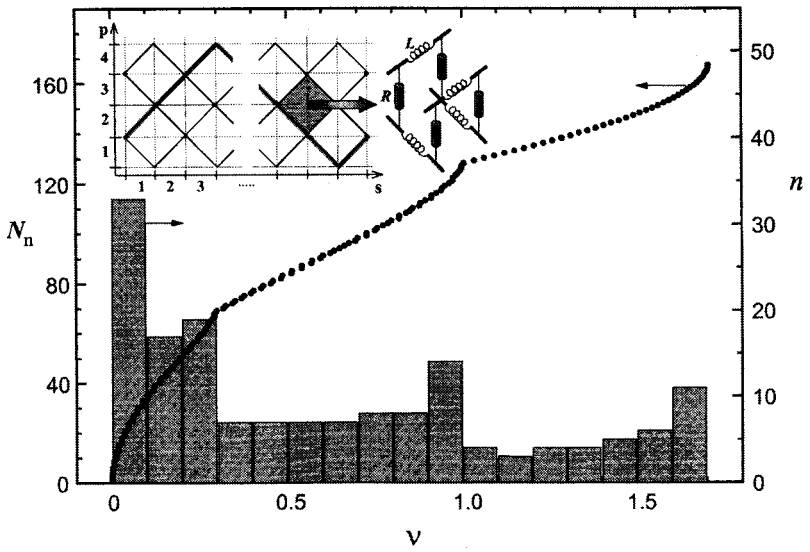

FIG. 1. The dependence $N_n = N_n(\nu)$ for C4 with $N = 167$. The histogram shows $n = n(\nu)$. The frequency ν is in units of R/L.

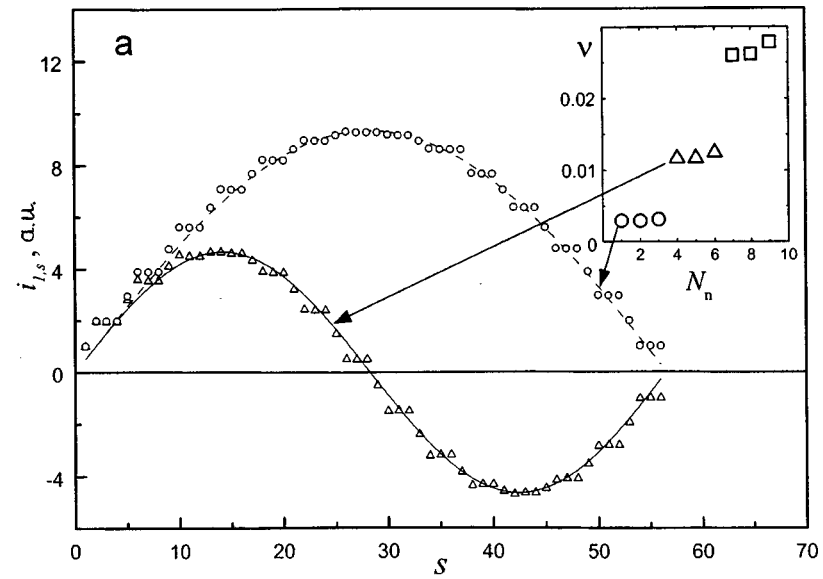

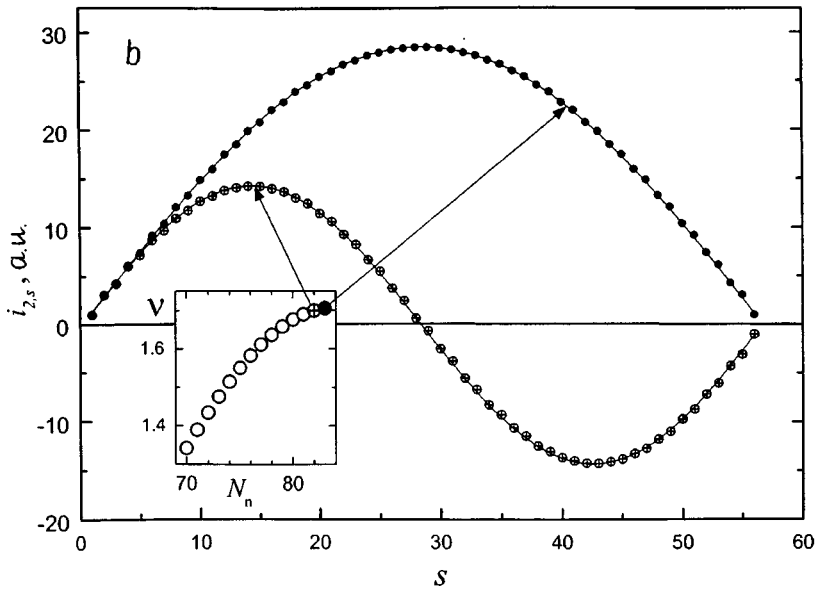

FIG. 2. Distributions of induced currents for limiting frequencies (the values of ν are given in units of R/L): a — along an individual ($k = 1$) strand of C4 cable (shown in the inset to Fig. 1) for $N = 83$ and the lowest ν values of the two lowest steps in the frequency spectrum (see inset). The values of the currents are normalized to the current in one of the cells; b — along the second layer of cable C4 ($N = 83$) for ν_{max} and the closest natural frequencies (see inset). The values of the currents are normalized to the current in one of the cells.

the same size as the sample. The lowest step corresponds to the sinusoidal loops with a half-period equal to the length of the strand in sample l, i.e., $i_{k,s} \sim \sin(\pi \cdot a \cdot s/l)$. The next ν triplet (quintuplet) corresponds to loops having the period l, and so on. This result is consistent with the prediction of the continuous model[9] and has a simple qualitative explanation: the inductance of the current loop is directly proportional to its length and the average resistance experienced by the currents flowing between the strands is directly proportional to the loop length. As a result, the damping time of a large loop is proportional to the square of its length, for instance $\tau_{\max} \sim l^2$, where $\tau_{\max}$ is the maximum time constant. Assuming $a = 10^{-3}$ m, $L \sim 10^{-10}$ H, $R \sim 10^{-5}\,\Omega$, and $l \sim 10^2 - 10^3$ m which is typical of the cables used in dipole magnets in accelerators,[10] the value of $\tau_{\max}$ can be estimated[9] as $10^5 - 10^7$ s. Significantly, as has been demonstrated experimentally,[11] even for short (~ 1 m) samples of flat cable the damping time constant of large loops may be ~ 1 h.

Large loops are evidently responsible for the existence of long-lived residual oscillations in accelerator magnets[1] and for the dependence of the normal-state transition current on the rate of current supply to the magnet.[2] These are an example of the long-range order correlation between the currents in the cells.

The range of large ν also exhibits a sinusoidal induced-current distribution, but in the cable layers. In this case, the maximum natural frequency $\nu_{\max}$ corresponds to a current distribution with a half-period equal to the layer length; the frequency closest to $\nu_{\max}$ corresponds to a current distribution with a period equal to the layer length, and so on (Fig. 2b). These distributions are not long loops, since the currents in the strands vary substantially over a distance of the order of a.

Quite clearly, as the sample length increases, for $\nu = \nu_{\max}$ the induced current distribution at the center of the sample becomes uniform. This means that the limit $\nu_{\max}$ for $l \to \infty$ can immediately be calculated for C4 as $\nu_{\max,\infty} = 1.707\,R/L$ and for C6 as $\nu_{\max,\infty} = 1.866\,R/L$. As the number of strands increases, $\nu_{\max,\infty}$ tends to the limit $2R/L \sim 2 \times 10^{-5}\,\mathrm{s}^{-1}$, which is substantially higher than the estimate given by Takács.[8]

The most difficult to describe is the central part of the spectrum where the long current loops and currents in various cells begin to be modulated by the twist pitch of the cable. A detailed analysis of this case will be reported in future publications.

An important characteristic of the ν spectrum is the density of states $n(\nu) = \partial N_n / \partial \nu$. The dependence $n = n(\nu)$ is plotted as a histogram in Fig. 1. It can be seen that the density of states has local maxima in sections corresponding to joins between regions and the edges of the spectrum. Further analysis is required to determine the influence of the characteristics of this spectrum on the response of a flat superconducting cable to the application of an alternating magnetic field.

This work was supported by the subprogram ''Topical Directions in the Physics of Condensed Media,'' ''Superconductivity,'' Project No. 98035 ''Symmetry.''

[1] A. K. Ghosh, K. E. Robins, and W. B. Sampson, Supercollider **4**, 765 (1992).
[2] L. Krempasky and C. Schmidt, Cryogenics **36**, 471 (1996).
[3] A. A. Akhmetov, A. Devred, and T. Ogitsu, J. Appl. Phys. **75**, 3176 (1994).
[4] A. P. Verweij, IEEE Trans. Appl. Supercond. **7**, 723 (1997).
[5] G. H. Morgan, J. Appl. Phys. **44**, 3319 (1973).
[6] A. A. Akhmetov, K. Kuroda, K. Ono, and M. Takeo, Cryogenics **35**, 495 (1995).
[7] B. Turck, Cryogenics **14**, 448 (1974).
[8] S. Takács, Supercond. Sci. Technol. **10**, 733 (1997).
[9] A. A. Akhmetov, A. Devred, R. G. Mints, and R. I. Schermer, Supercollider **5**, 443 (1995).
[10] A. Devred and T. Ogitsu, KEK preprint No. 94–156.
[11] A. A. Akhmetov, K. Kuroda, T. Koga, K. Ono, and M. Takeo, Inst. Phys. Conf. Ser. No. 148, 527 (1995).

Translated by R. M. Durham

Microscopic principles of information recording in condensed media

M. D. Bal'makov, L. N. Blinov, I. V. Murin, and N. S. Pocheptsova

St. Petersburg State Technical University
(Submitted January 21, 1998; resubmitted April 12, 1999)
Pis'ma Zh. Tekh. Fiz. **25**, 48–54 (July 12, 1999)

It is shown that the maximum information capacity of a condensed system is determined by the number of its equilibrium configurations. An analytic expression is obtained for the upper limit of the possible values of the information capacity. The problem of preserving stored information is discussed. © *1999 American Institute of Physics.* [S1063-7850(99)01007-1]

The information aspects of microscopic processes are currently being studied intensively.[1–3] This is not only because of their practical importance but also because of the internal logic of the evolution of physics. The practical aspect is related to the development of the scientific principles of nanotechnology, which in particular can be used to fabricate functional nanometer-size microelectronics elements. From the fundamental point of view, an investigation of the microscopic mechanism for the formation of nanostructures is a logically required step in the further development of the physics of condensed media.

The process of formation of nanostructures in condensed media depends on many factors and as these vary, different nanostructures are obtained. As a result, information can be recorded on the microscopic level. Its quantity I characterizes the information aspect[1] of the microscopic mechanism for structuring the various fragments of a condensed system. The question then naturally arises as to what quantity of information I can be recorded and stored over a fairly long time interval $t_{\max}$ in a system consisting of M atoms.

It is clear *a priori* that if M is finite, the value of I is also finite and, other conditions being equal, its value increases linearly with respect to M. The information content increases similarly as the number of symbols in a text increases.[1] Thus, the unknown value I is contained in the interval

$$0 \leqslant I \leqslant M B^{(I)}/\ln 2, \tag{1}$$

where $B^{(I)}$ is a constant, the information content I is expressed in bits, $B^{(I)}$ is in nats,[1] and the conversion factor between the units is $\ln 2$. The value of I is a function of the operator $\hat{\mathbf{W}}^{(r)}$, which describes the external action as a result of which the information is recorded. In other words, the numerical value of I from the interval (1) is determined by the choice of particular technical means used to record the information. Conversely, the numerical value of the constant B^I does not depend on this choice and is determined only by the fundamental equations of quantum theory.

The constraint is usually imposed that recorded information should be preserved with a probability $P(t)$

$$P(t) > 1-\varepsilon, \quad \text{for} \quad 0 \leqslant t \leqslant t_{\max}, \quad 0 < \varepsilon \ll 1, \tag{2}$$

close to unity over a fairly long time interval $t_{\max}$. It is also assumed that the value of $t_{\max}$ considerably exceeds the relaxation time of the phonon subsystem. Inequality (2) should be satisfied even in the presence of an unfavorable external perturbation $\hat{\mathbf{W}}$ whose prolonged action on the particular system generally results in the information being erased.

We shall estimate the numerical value of the constant $B^{(I)}$. We shall assume that information is recorded by means of structural transformations.[4] If all equilibrium configurations $\mathbf{R_i}$ corresponding to the minima of the adiabatic electron term $U_M(\mathbf{R})$ of the condensed system (Fig. 1) can be used to record, store, and read out information, this system can be considered to be a storage device with the information capacity[1]

$$I^{(s)} = \frac{\ln J}{\ln 2}, \tag{3}$$

where J is the number of physically nonequivalent minima of the function $U_M(\mathbf{R})$.

Usually, because of technical difficulties, a substantially smaller number $\tilde{J}$ of equilibrium configurations is suitable for recording information

$$\tilde{J} < J. \tag{4}$$

These form a so-called ensemble with reduced configurational entropy.[5] Hence, the actual information capacity $\ln\tilde{J}/\ln 2$ of the condensed system is smaller than the maximum possible capacity $I^{(s)}$ (3). The latter can be conveniently calculated using the relation[4]

$$J = \exp(\alpha_{\mathbf{n}} M + o(M)), \tag{5}$$

where $\alpha_{\mathbf{n}}$ is a positive parameter which only depends on the chemical composition $\mathbf{n}$ (the components of the vector $\mathbf{n}$ are the relative concentrations n_l of atoms of each type forming the particular condensed system with $\Sigma_l n_l = 1$), and the function $o(M)$ satisfies the condition $\lim_{M\to\infty} o(M)/M = 0$. Under these assumptions we obtain from Eqs. (1) and (3)–(5) $B^{(I)} \approx B$, where

$$B \equiv \sup_{\mathbf{n}} \alpha_{\mathbf{n}}. \tag{6}$$

It was shown in Ref. 6 that $B \approx 3$. As a result, we obtain the following estimate

$$B^{(I)} \approx 3. \tag{7}$$

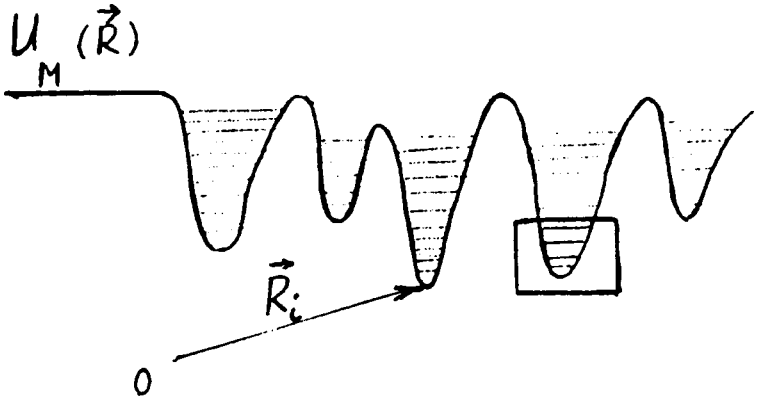

FIG. 1. Adiabatic electron term $U_M(\mathbf{R})$ for the ground state of the electron subsystem. The figure is arbitrary since for multiatomic systems ($M \gg 1$) the function $U_M(\mathbf{R})$ depends on many arguments $\mathbf{R}=(\mathbf{r}_1,\mathbf{r}_2,\ldots,\mathbf{r}_k,\ldots,\mathbf{r}_M)$, which determine the coordinates $\mathbf{r}_k$ of the atomic nuclei.

Naturally, when calculating $B^{(I)}$ (1) we need more than the minima of the adiabatic electron term $U_M(\mathbf{R})$ (Fig. 1) corresponding to the ground state of the electron subsystem. The excited states also make some contribution to $B^{(I)}$. In many cases, their role is fundamental, for example, when a ferromagnetic is used to record information. However, in the vast majority of cases the excited-state lifetimes τ_l of the electron subsystem are comparatively short ($\tau_l \ll t_{\max}$). These states are unsuitable for storing information over a fairly long time interval $t_{\max}$. The corresponding adiabatic electron terms may be neglected. Hence, the contribution of the excited states of the electron subsystem to the value of $B^{(I)}$ is not so large as to radically alter the estimate (7) according to which the constant $B^{(I)}$ (1) is of order unity.

In fact, the basis of the estimate (7) is relation (5) which establishes that the number J of different physically nonequivalent minima of the potential U_M $(\mathbf{R})$ (Fig. 1) increases exponentially rapidly with increasing number M of atoms forming a system of fixed ($\mathbf{n}=\text{const}$) chemical composition. This fact is not so surprising, since the value of J (5) allows for all potentially possible structures $\mathbf{R}_i$ of the condensed system. These structures include liquids, glasses, ideal crystals, crystals having different concentrations of particular defects, polycrystals, amorphous substances, amorphous and glassy films, pyroceramics, and many, many more, including structures of microinhomogeneous materials with information recorded in them in nanometer-size fragments. The many different minima of the adiabatic electron term $U_M(\mathbf{R})$ can also explain the possibility of varying the properties of a material having a specific chemical composition by obtaining different modifications.

The use of the adiabatic approximation is not so important for the approach being developed. Outside the limits of this approximation, the microscopic mechanism for recording information can be interpreted as a generally nonequilibrium transition from one ensemble of quantum states[4] to another and instead of Eq. (3), the information content $I^{(s)}$ will be given by

$$I^{(s)}=\frac{\ln G}{\ln 2}, \tag{8}$$

where G is the number of different quasiclosed ensembles of quantum states of the condensed system.

In particular, a quasiclosed ensemble may be formed by low-energy states localized in only one quantum well. The energies of the corresponding quantum states are shown by the sections of horizontal lines inside the rectangle in Fig. 1. In this case, under the action of an external perturbation $\hat{\mathbf{W}}$ transitions only take place between states of this quasiclosed ensemble, and transitions between different potential wells can be neglected. In other words, this ensemble is closed relative to the perturbation $\hat{\mathbf{W}}$, whereas it is open relative to the recording operator $\hat{\mathbf{W}}^{(r)}$.

Consequently, the microscopic mechanism for recording of information involves a transition to a predefined ''kth'' quasiclosed ensemble of quantum states (Fig. 2) under the action of an external perturbation $\hat{\mathbf{W}}^{(r)}$. Incidentally, many other processes may be interpreted as a transition from one quasiclosed ensemble to another. These include in particular melting, crystallization, vitrification,[4] and also chemico-information synthesis[7] which forms of the basis of modern nanotechnology.

This chemico-information synthesis process is a nonequilibrium process for which conditions of local thermodynamic equilibrium are not satisfied.[8] There is thus a need to develop nontraditional methods of describing these processes, which is why it is advisable to give a stricter definition of the concept of a quasiclosed ensemble.

As we know,[9] any state of a system is described by a

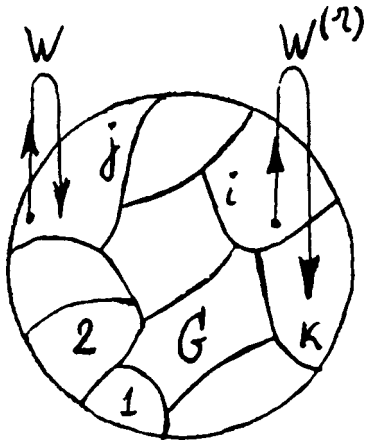

FIG. 2. Various quasiclosed ensembles.

corresponding statistical operator (density matrix) $\hat{\rho}(t)$ in Hilbert space Γ. A quasiclosed ensemble is understood to be a nonvoid set of system states satisfying the following two conditions.

1) A one-to-one correspondence can be established between the elements of this set and all possible statistical operators $\hat{\rho}^{(N)}$ of some subspace N of Hilbert space Γ. Each state of the quasiclosed ensemble is defined by a single operator $\hat{\rho}^{(N)}$, and conversely, each operator $\hat{\rho}^{(N)}$ of the subspace N defines a unit state from this ensemble.

2) Any state $\hat{\rho}(t)$ of the system which initially $(t=0)$ belongs to a quasiclosed ensemble $(\hat{\rho}(0)=\hat{\rho}^{(N)})$ is then $(0 \leqslant t \leqslant t_{max})$ described in the ε-approximation in subspace N even in the presence of an external perturbation $\hat{W}$. This implies that for $0 \leqslant t \leqslant t_{max}$ the following inequalities are satisfied

$$|\mathrm{Tr}(\hat{\rho}(t)\hat{f}_l) - \mathrm{Tr}_N(\hat{\rho}(t)\hat{f}_l)| < C_l\varepsilon, \quad l=1,2,\ldots . \qquad (9)$$

Here $\hat{f}_l$ are the operators of the physical quantities, $\mathrm{Tr}_N(\hat{\rho}(t)\hat{f}_l)$ is the sum of the diagonal matrix elements of the operator $\hat{\rho}(t)\hat{f}_l$ in an arbitrary orthonormalized basis of subspace N, $\mathrm{Tr}(\hat{\rho}(t)\hat{f}_l)$ is the similar sum for Hilbert space Γ, and C_l are constants.

The probability $P(t)$ of finding the system in one of the quasiclosed ensembles whose number is G (8) satisfies the inequality (2). This follows directly from the inequalities (9) if we set $\hat{f}_l = C_l = 1$ and also bear in mind that $\mathrm{Tr}(\hat{\rho}(t)) = 1$ and $P(t) = \mathrm{Tr}_N(\hat{\rho}(t))$. In other words, information is preserved in one of the quasiclosed ensembles (Fig. 2) over the time interval t_{max}.

The value of t_{max} can increase without bound as a result of improvements in the methods of recording and storing information. This cannot be said of the quantity I/M of stored information per atom. According to Eq. (1), the ratio I/M does not exceed $B^{(I)}\ln 2$. The closeness of I/M to the constant $B^{(I)}\ln 2$ [Eq. (1)] is one of the criteria for the efficiency of various methods of recording information.

In order to improve the efficiency, we need to use nanosize fragments, since the largest information content can be recorded by obtaining (synthesizing) quite specific information structures at the molecular level. This is essentially the main problem in modern nanotechnology. The information aspect of this problem has not been sufficiently well studied, although its importance is obvious.[7] Thus, we can hope that the results of the present study will also be useful for developing the theoretical principles of nanotechnology.

This work was supported financially by the Russian Fund for Fundamental Research (Project No. 98-03-32114a) and by the Russian State Committee for Higher Education (Project No. 97-92-66).

[1] B. B. Kadomtsev, Usp. Fiz. Nauk **164**, 449 (1994).
[2] *Ecoinformatics: Theory, Practice, Methods, and Systems*, edited by V. E. Sokolov [in Russian], St. Petersburg (1992) 520 pp.
[3] B. B. Kadomtsev, Usp. Fiz. Nauk **165**, 967 (1995).
[4] M. D. Bal'makov, *The Glassy State of Matter* [in Russian], St. Petersburg State University Press, St. Petersburg (1996), 184 pp.
[5] L. N. Blinov, M. D. Bal'makov, and N. S. Pocheptsova, Pis'ma Zh. Tekh. Fiz. **22**(21), 69 (1996) [Tech. Phys. Lett. **22**, 894 (1996)].
[6] M. D. Bal'makov, Glass Phys. Chem. **22**, 344 (1996).
[7] V. B. Aleksovskiĭ, *Chemistry of Permolecular Compounds* [in Russian], St. Petersburg State University Press, St. Petersburg (1996), 256 pp.
[8] P. Glansdorff and I. Prigogine, *Thermodynamic Theory of Structure, Stability, and Fluctuations* (Wiley, New York, 1971; Mir, Moscow, 1973, 280 pp.)
[9] L. D. Landau and E. M. Lifshitz, *Statistical Physics*, 3rd English ed. (Pergamon Press, Oxford, 1986) [Russ. original, earlier ed., Nauka, Moscow, 1964, 568 pp.]

Translated by R. M. Durham

Separation of germanium and silicon oxides by plasma-chemical deposition of germanosilicate glass in a moving plasma column

K. M. Golant and I. V. Nikitin

Scientific Center of Fiber Optics, Institute of General Physics, Russian Academy of Sciences, Moscow
(Submitted April 5, 1999)
Pis'ma Zh. Tekh. Fiz. **25**, 55–61 (July 12, 1999)

The optical transmission spectrum of germanosilicate glass deposited by surface plasma chemical vapor deposition on the inner surface of a quartz tube revealed interference resonances typical of multilayer dielectric coatings with alternating refractive indices. It is shown that this effect can be attributed to the longitudinal inhomogeneity of the plasma composition and specifically to an axial shift of the concentration maxima of germanium and silicon oxide. As a plasma having a nonuniform composition moves along the tube, a layer of glass is formed with a strong transverse germanium concentration gradient. It is established that in surface plasma chemical vapor deposition the axial separation of the regions of deposition of the silicon and germanium oxides increases if the glass is synthesized under conditions of oxygen deficiency.
 [S1063-7850(99)01107-6]

Surface plasma chemical vapor deposition (SPCVD) is used to synthesize quartz-glass preforms for fiber-optical waveguides.[1] In this method, layers of pure and doped SiO_2 are deposited on the inner surface of a section of quartz glass tube whose volume is periodically filled with a chemically active plasma. This periodic filling is accomplished by varying the length of a steady-state plasma column which is created and sustained in the tube by microwave energy transported by surface plasma waves.[2] The length of the column (distance between the point of application of the microwave field and the point of plasma detachment) is regulated by varying the power supplied to the plasma.

In SPCVD, silicon dioxide is synthesized by passing silicon tetrachloride mixed with oxygen through a moving plasma column. When the reagents enter the discharge zone, gas-phase SiO molecules are formed as a result of the plasma-chemical interaction between $SiCl_4$ and oxygen molecules excited by electron impact. The process of glass formation on the walls of the tube terminates, where the SiO adsorbed from the gas phase is oxidized to give SiO_2 by heterogeneous addition of oxygen. The chlorine released as a result of the reactions and the excess oxygen are removed by the pumping system.

Here we report some characteristic features of the formation of germanosilicate glass by this method. In the experiments we synthesized and investigated glass coatings 200 μm thick deposited on the inner surface of a quartz tube having an outer diameter of 20 mm and a wall thickness of 2 mm. An $O_2+SiCl_4+GeCl_4$ mixture was passed into the tube at a total pressure of around 0.2 Torr. Each reagent was supplied via a separate RRG-9 gas flow rate regulator which measured each component of the gas mixture to within 1%. The coatings were deposited by periodically moving a plasma along a 25 cm long section of the tube. The velocity and amplitude of the displacement of the plasma column front was controlled using a feedback system which controls the microwave power supplied to the plasma. The chloride flow rate and the plasma displacement velocity were such that a 200 μm thick coating was obtained after 400 plasma passes. The temperature of the tube walls was stabilized at around 1200 °C by means of an electrical furnace and was monitored with an optical pyrometer. During the deposition process we observed temperature fluctuations in the range of ± 50 °C about a given value, which were synchronous with the periodic motion of the plasma column and caused by the internal plasma heating of the tube. The deposition process was carried out with a flow rate ratio $SiCl_4/GeCl_4=10{:}1$, which corresponds to a GeO_2 content in the resultant glass of around 10 mol.% assuming 100% efficiency of implanting silicon and germanium atoms in the glass. After the end of the deposition process, the tube together with the layer of germanosilicate glass deposited on the inside was cut into transverse sections. These transverse sections were used as samples to obtain transmission spectra and were examined by electron microscopy.

A characteristic feature of the optical transmission spectrum of the deposited glass is its contrast interference structure (Fig. 1) which indicates that the refractive index distribution exhibits regular variations over the coating thickness. From the spectral position of the peaks we can readily establish that these correspond to different interference orders of the same periodic refractive-index structure with the fundamental interference order at the wavelength $\lambda_0 \approx 2.9\ \mu$m.

Figure 2 shows a photograph of a transverse section of the deposited layer of germanosilicate glass obtained using a scanning electron microscope. The light bands correspond to sections of the glass having an increased germanium content. It can be seen that the periodic structure responsible for the observed transmission spectrum of the coating can be attributed to germanium concentration peaks repeated from one

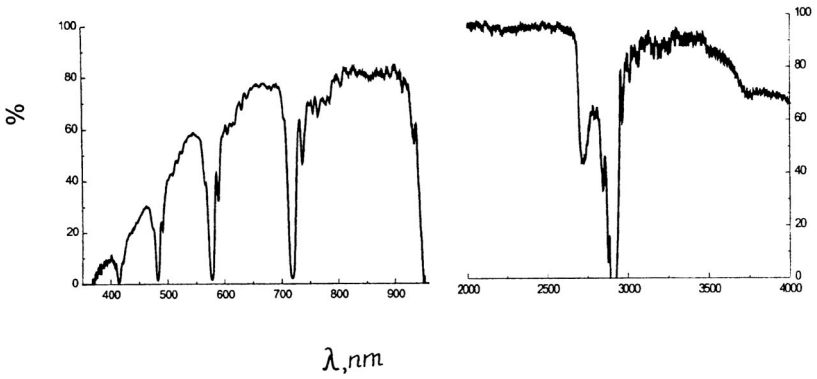

FIG. 1. Transmission spectrum of a germanosilicate glass coating 200 μm thick deposited on the inner surface of a quartz glass tube by SPCVD. The measurements were made using an S2000 Ocean Optics Inc. spectrometer at 350–940 nm and using a Perkin–Elmer Fourier spectrometer at 2000–4000 nm.

layer to another, which increase the refractive index of the glass. Note that, judging by Fig. 2, the thickness of the germanium-enriched layers is small and is at least an order of magnitude less than the period of the structure (≈ 1 μm for the deposition regime described above). We used the method of characteristic matrices[3] to model the transmission spectrum of a structure formed by ''thick'' dielectric layers of thickness d separated by ''thin'' dielectric layers of high refractive index. The fundamental interference order for which the transmission coefficient of this structure has a minimum corresponds to the condition $d=\lambda_0/2n$ where n is the refractive index of the glass in the thick layer. For $\lambda_0 \approx 2.9$ μm and $n \approx 1.45$ (undoped quartz glass) we obtain the estimate $d \approx 0.98$ μm which shows good agreement with the period of the layered structure shown in Fig. 2. If the total number of structure periods is 200 and the thickness of the thin germanium-enriched layers is of the order of 0.1 μm, the refractive index of the thin layers would have to be 1.55–1.6 to produce a contrast interference spectrum such as that shown in Fig. 1. Since the refractive index increment of quartz glass caused by introducing 10 mol.% GeO_2 does not exceed 0.014, it must be concluded that the SiO_2 and GeO_2 are substantially stratified at the glass formation stage in SPCVD. We note that the observed effect is too great to be a consequence of variations in the germanium content caused by the periodic temperature fluctuations of the tube walls noted above.

Direct confirmation of a layering effect at the stage where the chlorides are converted to the gas phase is provided by the distribution curves of SiO molecules and Ge atoms in the plasma, obtained by local emission optical spectroscopy (Fig. 3). In the experiments we measured the intensity distributions of the 425 nm (SiO molecular band[4]) and the 327 nm spectral lines (Ge atomic line[5]) along the plasma column. Apart from variations in the parameters of the plasma electron component (density and temperature), the radiation intensities of the bands correspond to the concentrations of emitting particles. It can be seen from Fig. 3 that the maxima of the axial distributions of SiO and Ge are shifted relative to each other and the shift increases as the oxygen partial pressure decreases. As a result of this shift, the gaseous medium above the deposition zone is a section of plasma having a highly nonuniform composition. On its right-hand side some distance from the microwave exciter, predominantly SiO_2 is deposited whereas on the left-hand side it is predominantly GeO_2 (Fig. 2). The periodic motion of this inhomogeneous deposition zone relative to the tube results in the formation of a layered structure in the deposited layer.

Note that the thermodynamic characteristics of SiO and GeO differ substantially. For instance, the sublimation temperature of GeO at normal pressure is only 710 °C (Ref. 6), i.e., even at high pressure it is far below the characteristic temperature maintained during the deposition of quartz glass in the SPCVD process (1000–1200 °C). This can explain the ''pulling'' of Ge from the deposition zone into the depth of the plasma column. Quite clearly, this effect is intensified when there is an oxygen deficiency because the rate of heterogeneous oxidation of GeO to form GeO_2 is reduced.

To conclude we note that this layering effect in SPCVD is evidently typical not only of germanosilicate glass but also of other SiO_2-based systems in which the active radicals

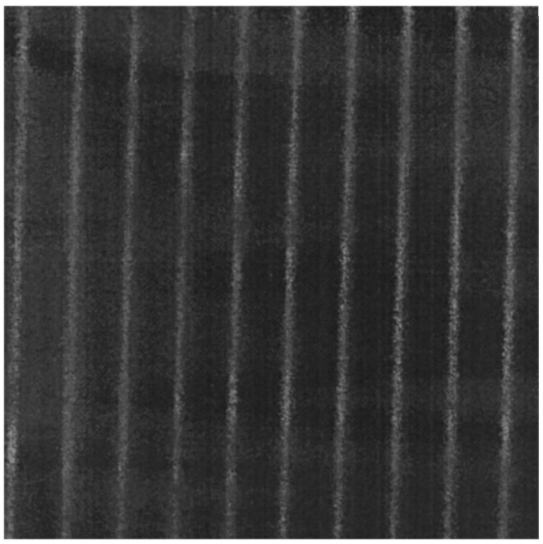

FIG. 2. Electron image of the transverse cross section of a deposited coating, which illustrates the periodic spatial variation of the germanium distribution. The period of the structure is 1 μm.

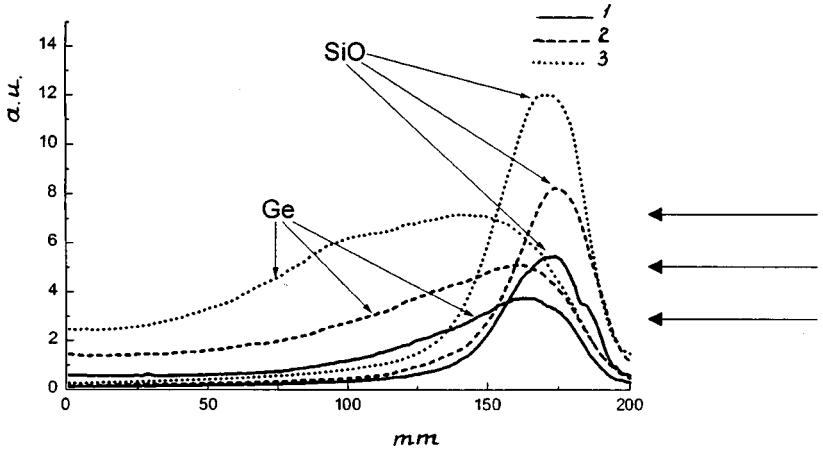

FIG. 3. Intensity distribution of the emission lines of SiO molecules and Ge atoms along a chemically active plasma at various oxygen partial pressures. The excess of oxygen in the gas mixture over that required by stoichiometry to oxidize all the silicon and germanium atoms is: *1* — a factor of 6.5; *2* — a factor of 4; and *3* — a factor of 2.6. The abscissa is directed from the exciter toward the point of plasma quenching.

forming the glass are produced in different parts of the deposition zone. By varying the ratio of the reagent flow rates, we can control the parameters of these layered structures so that this effect can be used to produce quartz-glass optical interference filters.

For the optical measurements we used apparatus from the central pool of spectroscopic equipment of the Russian Academy of Sciences and we should like to thank the director, V. G. Plotnichenko, for making this possible. The authors would also like to thank S. V. Lavrishchev for the electron microscopic analyses of the samples and Prof. A. S. Biryukov for valuable comments.

This work was partially supported by the Russian Fund for Fundamental Research (Project No. 98-02-16361).

[1] D. Pavy, M. Moisan, S. Saada, P. Chollet, P. Leprince, and J. Marrec, in *Proceedings of the 12th European Conference on Optical Communication*, Barcelona, 1986, pp. 19–22.
[2] M. Moisan, C. Beaudry, and P. Leprince, IEEE Trans. Plasma Sci. **PS-3**(2), 55 (1975).
[3] M. Born and E. Wolf, *Principles of Optics*, 4th ed. (Pergamon Press, Oxford, 1969; Nauka, Moscow, 1970, 885 pp.).
[4] K. P. Huber and G. Herzberg, *Molecular Spectra and Molecular Structure*, Vol. 4 *Constants of Diatomic Molecules* [Russ. transl., Nauka, Moscow, 1984, 365 pp.].
[5] C. H. Corliss and W. R. Bozeman, *Experimental Transition Probabilities for Spectral Lines of Seventy Elements* (U.S. Government Printing Office, Washington, D.C., 1962; Mir, Moscow, 1968, 561 pp.).
[6] *Handbook of Physical Quantities* edited by I. S. Grigor'ev and E. Z. Meĭlikhov [in Russian], Energoatomizdat, Moscow (1991), 1232 pp.

Translated by R. M. Durham

Electron impact ionization of $(1s2s2p)^4P_j$ autoionization states of the lithium atom

V. N. Krasilinets

Institute of Electronic Physics, Ukrainian National Academy of Sciences, Uzhgorod
(Submitted August 14, 1998; resubmitted January 28, 1999)
Pis'ma Zh. Tekh. Fiz. **25**, 62–67 (July 12, 1999)

Electron spectroscopy using intersecting electron and atomic beams was used for the first time to measure the electron excitation function of the $(1s2s2p)^4P_{1/2,3/2}$ autoionization states of the lithium atom in the range of collision energies between the level excitation threshold and 90 eV with an energy resolution better than 0.4 eV and a magic observation angle $\theta = 54.7°$. An analysis of the intense near-threshold structure observed revealed for the first time that autodetachment states of the negative lithium ion having excitation thresholds of 58.2 ± 0.1 and 59.5 ± 0.1 eV exist in the autoionization energy range. © *1999 American Institute of Physics.* [S1063-7850(99)01207-0]

Studies of negative Li ions in the autoionization energy range are of practical interest because of their potential use for plasma injection heating in tokamaks.[1] Theoretical calculations[2,3] predict that $(1s2s2p^2)^5P^e$ and $(1s2p^3)^5S^0$ states of the Li ion metastable against electron decay exist at energies of 56.892 and 60.443 eV, respectively, based on $(1s2s2p)^4P$ and $(1s2p^2)^4P$ autoionization states. These states are interrelated by a dipole transition ($\lambda = 349$ nm) which was observed experimentally in beam-film experiments.[4] However, the literature contains no experimental or theoretical data on the existence of negative lithium ion states which decay in the electron channel (so-called autodetachment states). Feldman and Novick[5] suggested that the $(1s2s3snp)^5P$ Li autodetachment state may influence the excitation of the $(1s2s2p)^4P_{5/2}$ metastable level because of the near-threshold structure observed on its electron excitation function. The $1s2s2p$ configuration contains two other quartet P-levels with $j = 1/2$ and $j = 3/2$ which, unlike the $^4P_{5/2}$ level, decay effectively in the electron channel.[5] In view of the negligible splitting of these levels ($\Delta E \leqslant 3.5\ \mathrm{cm}^{-1}$; Ref. 6), their electron decay in the autoionization spectra corresponds to a single line at 52.02 eV (Refs. 7 and 8). In order to observe and identify the role of the autodetachment levels of the Li ion in the excitation of the $(1s2s2p)^4P_{1/2,3/2}$ autoionization levels, we measured their total electron excitation function for the first time. Particular attention was paid to studying the near-threshold range of excitation energies, for which measurements were made with a collision energy step of 0.1 eV and an energy resolution of $\leqslant 0.4$ eV. In order to eliminate any influence of the anisotropy of the angular distribution of the emitted electrons, the autoionization spectra were measured at the magic observation angle $\theta = 54.7°$.

The experimental setup and the method of studying the electron excitation of the autoionization states were described in detail in Ref. 7. The apparatus consists of an electron gun, a 127° cylindrical electron energy analyzer, and a source of neutral lithium atoms. The analyzer recorded the energy spectra of the autoionization electrons formed by decay of the autoionization states of the lithium atom. The excitation function of the $(1s2s2p)^4P_{1/2,3/2}$ states was obtained by measuring the intensity of the corresponding line in the electron spectra normalized to the primary electron beam current at various collision energies. The relative error in measurements of the line intensity in the spectra was less than 30% at energies near the threshold. Each point on the electron excitation function was determined as the average of data taken from three independent measurements. The error in determining the collision energy was 0.1 eV.

Figure 1 shows the electron excitation function of the $(1s2s2p)^4P_{1/2,3/2}$ autoionization states of the lithium atom at collision energies between the excitation threshold and 90 eV. A characteristic feature of the function is its resonant structure in the form of peaks *a*, *b*, *c*, *d*, and *e* at energies of 58.2, 59.5, 61.2, 62.8, and 63.8 eV, respectively, with a principal peak at 68.5 eV.

On analyzing the origin of the structure *a*–*e* we shall first consider radiative cascade transitions which can cause additional filling of these $^4P_{1/2,3/2}$ states. The first well-known cascade transition ($\lambda = 371.4$ nm; Ref. 9) corresponds to decay of the nearest $(1s2p^2)^4P$ level located at 60.75 eV (Ref. 8; Fig. 2). On the measured electron excitation function this transition corresponds to the beginning of the *c* peak (see arrow in Fig. 1). The beginning of peaks *d* and *e* (see arrows) coincides with the excitation thresholds of the $(1s2s3s)^4S$ and $(1s2s4s)^4S$ levels, thereby reflecting the corresponding cascade transitions with $\lambda = 293.4$ nm and $\lambda = 217.3$ nm, respectively[9] (Fig. 2). Peaks *a* and *b* are positioned below the threshold of the first cascade transition at 60.75 eV (Fig. 2) and thus cannot be ascribed to the process of cascade filling of the $^4P_{1/2,3/2}$ levels considered above. We shall therefore consider possible resonance processes for the excitation of these levels. It can be seen from the diagram in Fig. 2 that peaks *a* and *b* are located in the energy gap between the $1s(2s2p^1P)^2P$ and $(1s2s2p)^4P_j$ autoionization states.

The theoretical calculations[2] indicate that this energy range contains the $1s2s2p^2$, $1s2s2p3s$, and $1s2s2p3p$ electron configurations of the Li ion formed on the basis of

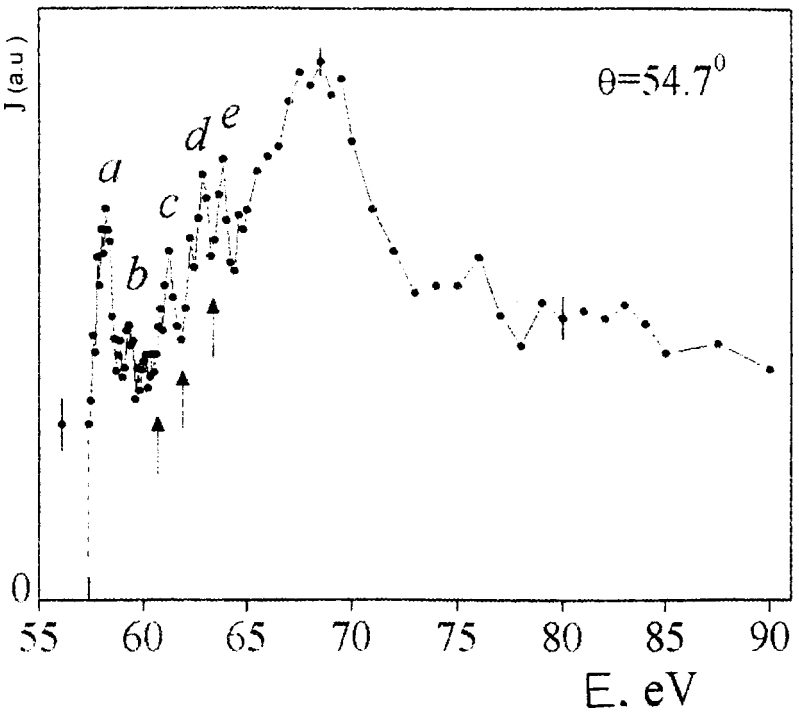

FIG. 1. Electron excitation function of the $(1s2s2p)^4P_{1/2,3/2}$ autoionization states of the lithium atom at collision energies between the 57.41 eV excitation threshold[8] and 90 eV.

the $1s(2s2p^3P)^2P$ and $1s(2s2p^1P)^2P$ doublet states. In L–S coupling only the $^3P^{o,e}$ and $^3D^{o,e}$ terms of these configurations can decay into $(1s2s2p)^4P_{1/2,3/2}$ levels, resulting in the appearance of peaks *a* and *b*. Another process which could be responsible for these peaks is the formation of shape resonances in the near-threshold electron excitation of the ^4P levels. In this case, peaks *a* and *b* should reflect the single-channel decay of the appropriate resonances to the initial ^4P_j level. However, our investigations of the electron excitation function of the $(1s2s^2)^2S$ and $1s(2s2p^3P)^2P$ autoionization states[7] show that characteristics *a* and *b* are also present on these functions, indicating that the decay of the corresponding resonances is a multichannel process (Fig. 2). On this basis, we identified characteristics *a* and *b* as a manifestation of the decay of the autodetachment states of the Li ion with terms $^3P^{o,e}$ or $^3D^{o,e}$ at energies of 58.2 and 59.5 eV. In examining the origin of peaks *c*–*e*, one should note that their well-defined resonant nature unambiguously indicates that they are related to processes of resonant excitation of the upper quartet autoionization states. The corresponding resonance states may decay into the nearest quartet atomic states (so-called resonance cascades) which fill the $^4P_{1/2,3/2}$ levels being studied as a result of radiative decay (radiation cascades; Fig. 2).

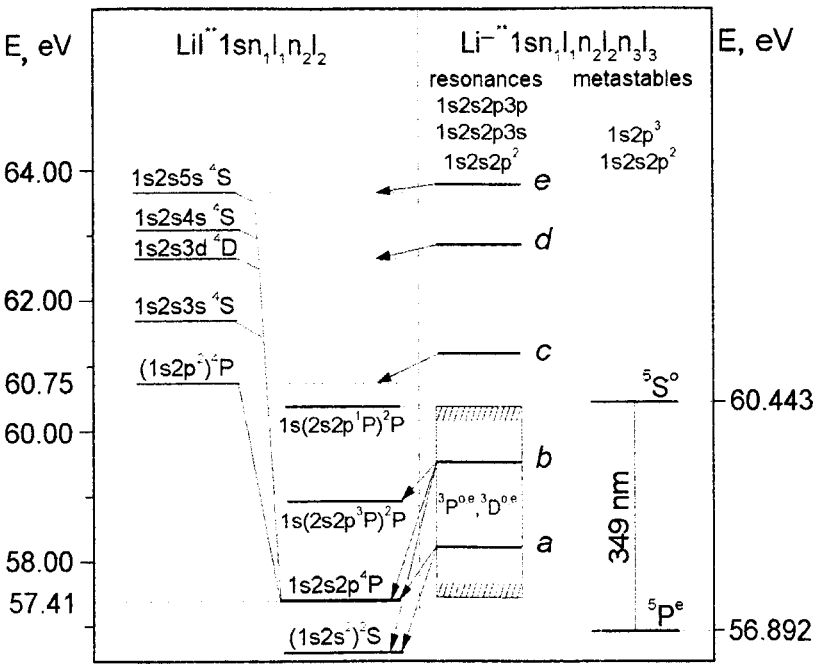

FIG. 2. Energy level diagram of the lithium atom[8,9] and a negative Li^- ion[3] in the range 56–64 eV. The letters *a*–*e* denote the resonance structure observed on the excitation function of the $(1s2s2p)^4P_{1/2,3/2}$ states. The lines without arrows denote well-known radiative transitions in the system of quartet autoionization levels[9] and between Li^- states.[2,4] The lines with arrows indicate possible electron channels for the decay of resonances *a*–*e*.

To sum up, these experimental data and their analysis unambiguously indicate that the near-threshold electron excitation of the $(1s2s2p)^4P_j$ autoionization states is a resonant process associated with the existence of autodetachment states of the Li ion.

To conclude, it is the author's pleasant duty to thank senior collaborator A. A. Borovik and Professor I. S. Akeksakhin for useful discussions and assistance.

This work was partially supported financially by INTAS (Grant No. 96-0477).

[1] V. A. Esaulov, Ann. Phys. (San Diego) No. 11, 493 (1986).
[2] C. F. Bunge, Phys. Rev. A **22**(1), 1 (1980).
[3] H. Y. Yang and K. T. Chung, Phys. Rev. A **51**, 3621 (1995).
[4] S. Mannervik, G. Astner, and M. Kisielinski, J. Phys. B **13**, 441 (1980).
[5] P. Feldman and R. Novick, Phys. Rev. **160**, 143 (1967).
[6] P. Feldman, M. Levitt, and R. Novick, Phys. Rev. **21**, 331 (1968).
[7] A. A. Borovik, V. N. Krasilinets, and I. S. Aleksakhin, Ukr. Fiz. Zh. **42**, 400 (1997).
[8] D. Rassi, V. Pejcev, and K. J. Ross, J. Phys. B **10**, 3535 (1977).
[9] S. Mannervik and H. Cederquist, Physica Scripta **27**, 175 (1983).

Translated by R. M. Durham

Influence of a sapphire substrate on the emission spectra of gallium nitride light-emitting diodes

V. E. Kudryashov, S. S. Mamakin, and A. É. Yunovich

M. V. Lomonosov State University, Moscow
(Submitted March 3, 1999)
Pis'ma Zh. Tekh. Fiz. **25**, 68–72 (July 12, 1999)

The emission spectra of green light-emitting diodes based on InGaN/AlGaN/GaN heterostructures revealed a weak thin doublet line at the long-wavelength edge. This line is ascribed to luminescence of residual Cr^{3+} impurity ions in the sapphire substrate (similar to ruby, Al_2O_3:Cr, doublet wavelengths 692.9 and 694.3 nm). The ions are excited by visible diode radiation which is close to the absorption bands of the Cr^{3+} ions. It is shown that ruby luminescence may be excited by radiation from blue and green GaN light-emitting diodes. © *1999 American Institute of Physics.* [S1063-7850(99)01307-5]

1. Recent investigations and development of gallium nitride light-emitting diodes (LEDs) have culminated in the mass production of these diodes.[1,2] However, the electroluminescence spectra of these LEDs continue to be studied by many authors (see Refs. 3 and 4 and the literature cited therein). Investigations of the recombination mechanisms in InGaN/AlGaN/GaN quantum-well heterostructures have shown that it is important to study not only the fundamental spectral bands but also details of the long- and short-wavelength edges of the spectra.

In the present study, a spectral line not observed previously was detected in the emission spectra of GaN LEDs from Hewlett–Packard and Nichia, fabricated from heterostructures grown on sapphire (Al_2O_3) substrates.[1,2] The luminescence spectra of these LEDs have a maximum in the blue–green region around ≈ 502–505 nm at room temperature and currents of 10–15 mA.

2. Figure 1 shows the typical spectrum of one LED with details visible on the long-wavelength tail of the spectrum when the gain is increased seventyfold and the spectral slits of the MDR-12 monochromator are broadened fivefold. The intensity of the narrow line near 694 nm increased with increasing current in the range $J = 2$–20 mA (Fig. 2).

Details of the spectrum for two LEDs (NLMP-CE30 and NSPG-510S) are shown in Fig. 3: the doublet lines have peaks at 692.9 nm and 694.3 nm. The intensity of these lines varies by a factor of 10–20 for the various LEDs studied. We know that the luminescence spectra of ruby ($Al_2O_3:Cr^{3+}$) contains these lines and that their excitation bands lie near 410 and 560 nm (Ref. 5).

A control experiment was set up using a ruby sample

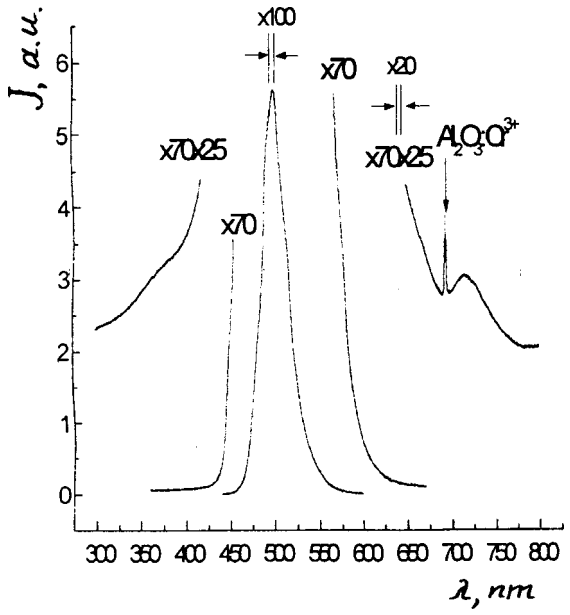

FIG. 1. Electroluminescence spectra of an NLMR-CE30 LED at $J = 30$ mA and room temperature showing the Cr^{3+} impurity line in the sapphire substrate.

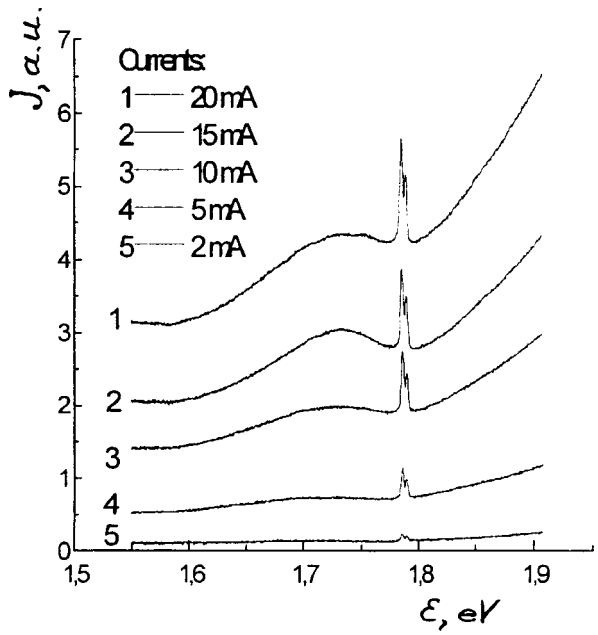

FIG. 2. Change in the emission spectra of Cr^{3+} impurities in a sapphire substrate for various currents through the LED.

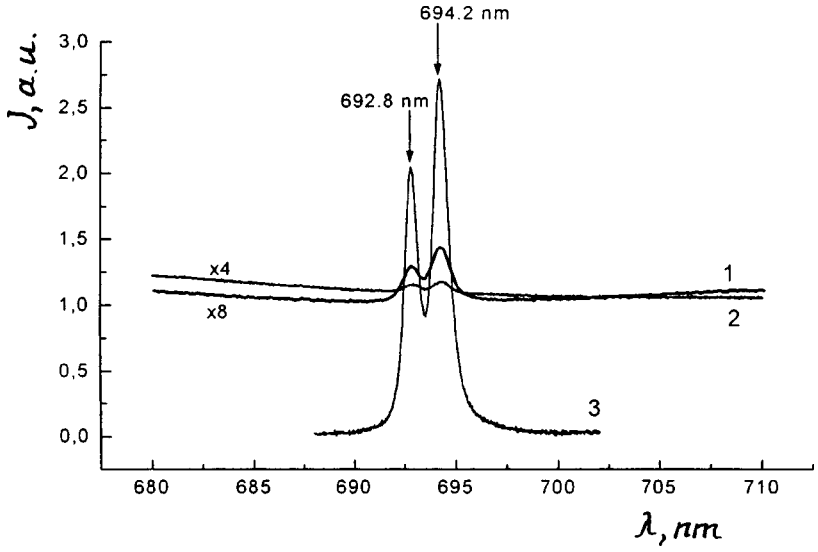

FIG. 3. Fine structure of Cr^{3+} impurity line in sapphire for two different LEDs compared with the photoluminescence line of ruby excited by radiation from an HLMP-CM30 LED: *1* — HLMP-CE30, $J=15$ mA, *2* — NSPG-510S, $J=15$ mA, *3* — ruby (excitation: HLMP-CM30, 30 mA).

containing 0.05% Cr ions. Different types of LED (blue, blue–green, and green) were placed with the plastic cap close to the end of a cylinder 6 mm in diameter and 25 mm long. The luminescence spectra were observed from the other end when excited by LED radiation at $J=30$ mA.

Figure 3 shows a typical photoluminescence spectrum of $Al_2O_3:Cr^{3+}$ compared with the lines in the LED spectra — the position and shape of the doublet lines agree to within ± 0.1 nm.

3. It has thus been shown that the line observed in the LED spectra is caused by the influence of residual Cr impurities in the sapphire substrates. It has also been shown that ruby luminescence can be excited by radiation from GaN heterostructure LEDs. Of particular interest is the fact that, in principle, these heterostructures can be grown not only on pure sapphire but also on ruby $Al_2O_3:Cr^{3+}$.

One important technical application of GaAs LEDs and injection lasers emitting in the infrared at ≈ 800 nm is the excitation of neodymium-doped garnet lasers.[5] If the radiation power of a GaN LED is sufficiently high and the emission spectrum is selected to coincide with the excitation bands of the Cr^{3+} ions, it is interesting to investigate the possibility of exciting ruby lasers using these LEDs. A recent report by Nichia on the initial manufacture of GaN injection lasers[6] suggests that experiments can be carried out on the excitation of ruby by GaN lasers.

We know that LEDs have been developed in which white light is achieved by coating blue GaN LEDs with a yellow phosphor.[7] If the LED radiation can be converted sufficiently efficiently to the ruby line, the color of the LED radiation can be changed by adding the fundamental blue or green radiation band to the red ruby radiation.

The authors would like to thank Dr. P. Martin (Hewlett–Packard Laboratory) for supplying LED samples to the semiconductor department of Moscow State University and N. A. Kravtsov for supplying the ruby and for discussions of the results.

[1] F. A. Ponce and D. P. Bour, Nature (London) **386**, 351 (1997).
[2] S. Nakamura and G. Fasol, *The Blue Laser Diode; GaN Based Light Emitters and Lasers* (Springer-Verlag, New York, 1997), 256. pp.
[3] A. E. Yunovich, V. Kudryashov, A. Turkin, K. Zolina, A. Kovalev, and F. Manyakhin, in *Proceedings of the 2nd Symposium on III–V Nitride Materials and Processes*, Vol. 97–34 (Electrochemical Society Press, Pennington, NY, 1998), pp. 83–102.
[4] A. N. Kovalev, F. I. Manyakhin, V. E. Kudryashov, A. N. Turkin, and A. É. Yunovich, Fiz. Tekh. Poluprovodn. **33**, 224 (1999) [Semiconductors **33**, 192 (1999)].
[5] G. M. Zverev and Yu. D. Golyaev, *Crystal Lasers and Their Applications* [in Russian], Moscow (1994), 312 pp.
[6] *''Nichia announces laser commercialization''*, MRS Internet J. Nitride Semiconductor Res. http://nsr.mij.mrs.org/news/lasers4sale.html. DLB
[7] S. Nakamura, Mater. Res. Soc. Symp. Proc. **449**, 135 (1997).

Translated by R. M. Durham

Attraction of macrobodies in a plasma

A. E. Dubinov, V. S. Zhdanov, A. M. Ignatov, S. Yu. Kornilov, S. A. Sadovoĭ, and V. D. Selemir

Russian Federal Nuclear Center, Research Institute of Experimental Physics, Sarov
Institute of General Physics, Russian Academy of Sciences, Moscow
(Submitted January 22, 1999)
Pis'ma Zh. Tekh. Fiz. **25**, 73–80 (July 12, 1999)

Results are presented of an experimental investigation of the observation of attraction between metal and dielectric macrobodies in the air plasma of a steady-state dc glow discharge and measurements were made of the attraction as a function of the plasma density. The potential difference between the bodies was measured as a function of the plasma density. © *1999 American Institute of Physics.* [S1063-7850(99)01407-X]

We know that under certain conditions in a dusty plasma, the dust microparticles may become aligned to form ordered structures known as plasma-dust crystals.[1–3] Since the dust particles in a plasma may become charged to some equilibrium electrical charge of the same sign, usually negative, at distances shorter than the Debye length they should repel each other because of their Coulomb interaction. However, in addition to repulsion, at large distances mechanisms of attraction must exist between dust microparticles which confine a plasma dust crystal so that it does not decay. At this point, we note that the formation of a homogeneous crystal structure of like charged particles in a closed container or unbounded space does not generally require long-range forces of attraction, although for the bounded crystal structures observed experimentally[3] the search for mechanisms of attraction between dust particles is quite justified.

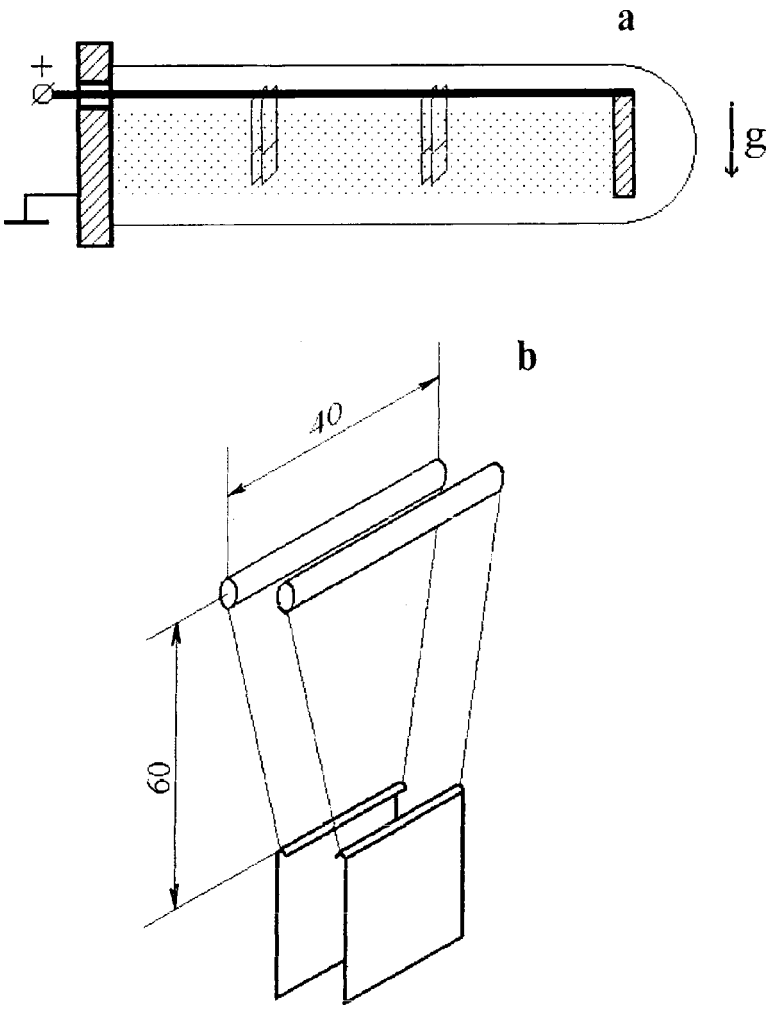

FIG. 1. Schematic of experiment: a — discharge chamber, b — plate suspension system (all dimensions in millimeters).

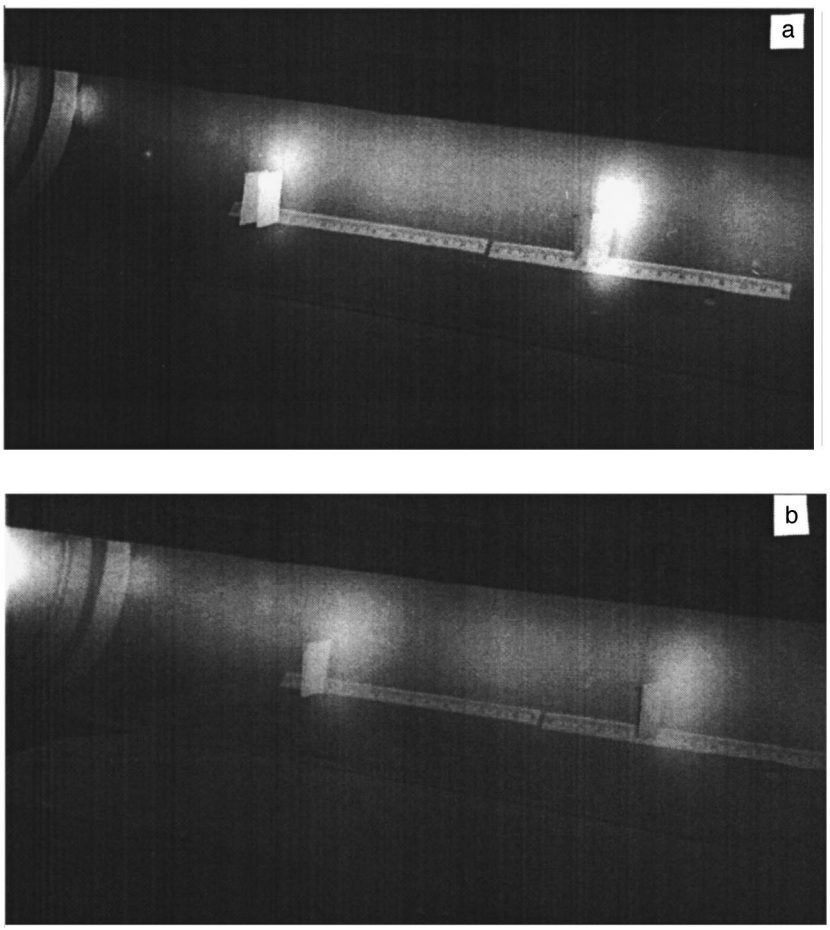

FIG. 2. Photographs showing the position of the plates in the plasma: a — minimum discharge current, plates freely suspended, b — discharge current ~0.5 A, plates have converged completely.

Various theoretical studies have now been published in the scientific literature in which several different forces of attraction have been proposed and analyzed, among which we note the following:

1) Attraction whose mechanism is based on the asymmetric bombardment of a dust particle by plasma particles caused by shadowing of this dust particle by neighboring ones;[4,5]

2) Attraction caused by Coulomb scattering of charged plasma particles by charged dust particles;[6]

3) Attraction as a result of ion-acoustic wave coupling between dust particles, which, as is shown in Ref. 7, is a classical analog of the Cooper pairing of electrons well-known from the theory of superconductivity in metals.

Existing ideas on the mechanisms of attraction between dust particles in a plasma were reviewed in Ref. 6. However, despite numerous studies of the theoretical aspects of this problem, as far as we are aware, no specific experimental studies have been made of the attraction of dust particles in a plasma. In view of this, the aim of the present study was to make direct experimental observations of the attraction between macroscopic particles in a plasma.

Clearly, it is difficult to investigate the attraction of dust particles (''zero-dimensional'' macroscopic objects) by means of direct observations because of their smallness. For the measurements it is therefore advisable to use their one-dimensional (thin filament) or two-dimensional (thin-film) analogs. In our previous study[8] we observed the attraction of two polyester fiber films suspended freely in the Earth's gravitational field and inserted into a plasma and we observed that at constant pressure the attractive forces increased as the degree of ionization of the plasma increased.

However these measurements were made with a high degree of error and inadequate reproducibility because of the thermal action of the plasma on the film, so that even after a short time in the plasma, the films crumpled, twisted, and were no longer flat and frequently had to be replaced. Moreover, the imperfect suspension of the films as a result of the uncontrollable deviation from the vertical at the upper point resulted in a substantial spread of the measured attraction after new films had been installed. In addition, the attraction between metal objects remained unexplained in Ref. 8. These factors stimulated further research and the search for more acceptable designs of attracting objects in the plasma.

The experiments were carried out as in Ref. 8 in a thin-walled glass discharge chamber 180 mm in diameter with an interelectrode gap 700 mm long (Fig. 3a). The chamber was positioned horizontally so that the freely suspended objects in the chamber were at right angles to the discharge current.

The air pressure in the chamber was maintained between 0.01 and 0.1 Torr. A steady-state dc glow discharge was ignited between the chamber electrodes. The parameters of the discharge plasma were determined using a probe technique.

For the experiments we used 25×25 mm dielectric (80

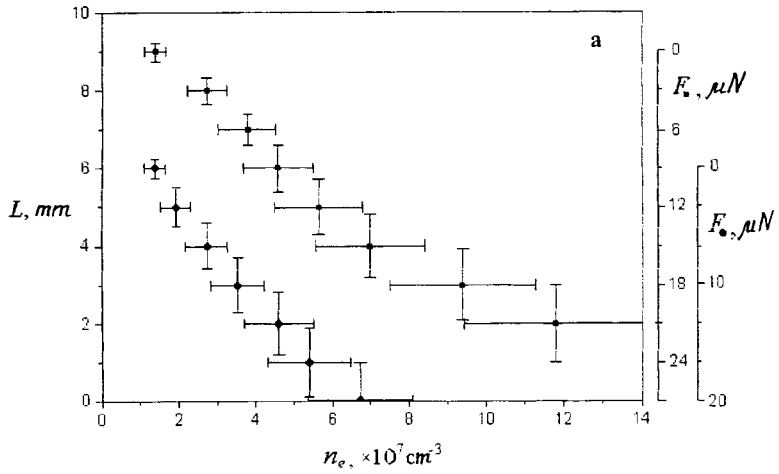

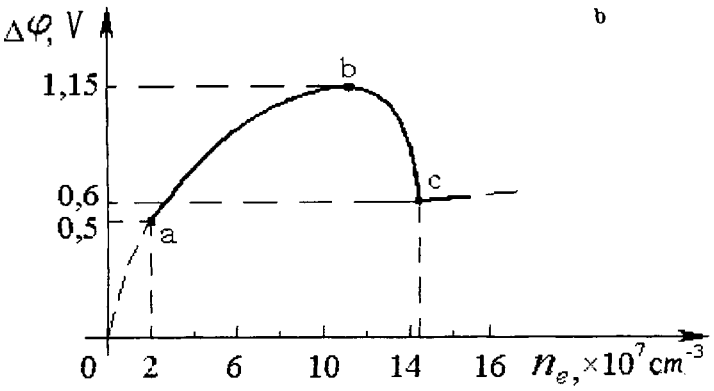

FIG. 3. Graphs showing experimentally determined dependences: a — forces of attraction between plates and distance between them as a function of plasma electron density (● — for paper plates, ■ — for aluminum plates); b — potential difference of aluminum plates versus plasma density.

g/m^2 photocopier paper) and metal (67.5 g/m^2 aluminum foil) plates suspended on copper wires 80 μm in diameter. The method and suspension geometry shown in Fig. 1b first, ensured sufficient sensitivity for the measurements and second, eliminated rotational movement of the plates about the vertical axis.

Figure 2a shows a photograph of the freely suspended plates in a weak discharge. As the discharge current and therefore the plasma density were slowly increased, the plates gradually came closer until their edges almost adhered (the approaching plates did not seem to come completely in contact, as discussed below). The final situation is shown in the photograph in Fig. 2b. The convergence of the plates was measured as a function of the discharge current and a correspondence was established between the values of the discharge current and the values of the electron density obtained from the results of the probe measurements. Figure 3a shows the behavior of the convergence thus obtained and the corresponding forces of attraction for paper and aluminum plates.

It should be noted that when the discharge burned nonuniformly in the form of standing striations the plates also converged at a specific pressure and discharge current, although the results of the measurements were less reproducible than those obtained for a homogeneous discharge.

After the discharge was quenched the plates repelled each other, which indicates that they had accumulated substantial electric charge of the same sign. However, external shorting of the aluminum plates did not change the character and nature of the attraction, which indicates that the attraction is nonelectrical.

The electric potential of the aluminum plates approximately corresponded to the potential of the positive discharge column, while the potential difference between the plates initially increased to 1.15 V as the plasma density increased and then dropped to 0.6 V as the plates came close together, indicating that there is a minimum gap between the plates, which according to our estimates is of the order of the Debye length (approximately a few hundredths of a millimeter). This can be attributed to the fact that at shorter distances the forces of electrostatic repulsion already exceed the forces of attraction observed by us. Figure 3b gives the potential difference for aluminum plates plotted as a function of the plasma density.

To sum up, these experimental results indicate that forces of attraction of a nonelectrical nature are observed between adjacent macroscopic bodies in a plasma, and these determine the dynamics of these bodies. These forces may also determine the hydrodynamics of the expansion of a dusty plasma cluster, slowing its expansion compared with that of a pure plasma and in many cases, causing self-compression of the cluster, as was shown in Ref. 9, which is

interesting in the context of plasma confinement. Another consequence of these forces of attraction is the formation of an isotropic surface tension at the boundary of a dusty plasma in contrast to the anisotropic tension at a plasma–magnetic field interface.

To conclude the authors thank A. A. Rukhadze for useful discussions.

[1] H. Thomas, G. E. Morfill, V. Demmel, and J. Goree, Phys. Rev. Lett. **73**, 652 (1994).
[2] J. H. Chu, J. -B. Du, and I. Lin, J. Phys. D: Appl. Phys. **27**, 296 (1994).
[3] V. E. Fortov, A. P. Nefedov, V. M. Torchinskiĭ *et al.*, Pis'ma Zh. Éksp. Teor. Fiz. **64**, 86 (1996) [JETP Lett. **64**, 92 (1996)].
[4] A. M. Ignatov, Fiz. Plazmy **22**, 648 (1996) [Plasma Phys. Rep. **22**, 585 (1996)].
[5] A. M. Ignatov, Kratk. Soobshch. Fiz. No. 1, 58 (1995).
[6] V. N. Tsytovich, Usp. Fiz. Nauk **167**, 57 (1997).
[7] M. Nambu, S. V. Vladimirov, and P. K. Shukla, Phys. Lett. A **203**, 40 (1995).
[8] A. E. Dubinov, V. S. Zhdanov, A. M. Ignatov *et al.*, Kratk. Soobshch. Fiz. No. 7, 40 (1997).
[9] V. N. Tsytovich and D. Rezendes, Fiz. Plazmy **24**, 71 (1998) [Plasma Phys. Rep. **24**, 65 (1998)].

Translated by R. M. Durham

Magnetization and nature of the rotation of the solar convective zone

Yu. V. Vandakurov

A. F. Ioffe Physicotechnical Institute, Russian Academy of Sciences, St. Petersburg
(Submitted April 17, 1999)
Pis'ma Zh. Tekh. Fiz. **25**, 81–88 (July 12, 1999)

An analysis is made of adiabatic magnetized differentially rotating structures of the stellar convective zone obtained by minimizing the production of entropy. The change in the law of rotation when one type of magnetic field is replaced by another (for example, a toroidal field by a poloidal one) is studied. It is found that for the latitude distribution of the rotation observed on the Sun, the variation in the latitude gradient of the angular rotation speed is comparatively small for this change in fields. This condition facilitates the establishment of cyclic variations in the field. In a configuration in which the equatorial layers rotate faster, it becomes more difficult for these variations to exist, which may account for the well-known Maunder minimum of solar activity. © *1999 American Institute of Physics.* [S1063-7850(99)01507-4]

In the stellar adiabatic convective zone, a unique situation is achieved where the entropy production is directly related to the distributions of the rotation and the magnetic field.[1,2] Here we shall assume that the establishment of convective heat transfer is always accompanied by the generation of turbulent viscosity, which is a strong source of entropy production. Since the theorem of the minimum property of entropy production[3] is valid for near-equilibrium states, we can use this property to find equilibrium or approximately equilibrium magnetized rotating configurations. We shall subsequently assume that this minimum property is achieved in the adiabatic part of the solar convective zone.

In Refs. 1 and 2 the present author showed that the minimization procedure being discussed can be used to obtain a rotation distribution of the type observed on the Sun even when there is no magnetic field, although this solution is unstable.[4] In the presence of a toroidal magnetic field this instability can be eliminated.[4] Also of interest is a more general field, in particular that undergoing slow time variations . In view of the complexity of the problem, we confine ourselves merely to a comparison of equilibrium models containing only a toroidal field or only a poloidal field. It is assumed that the distributions of the field and the rotational speed are determined in accordance with the condition of minimum entropy production. Naturally, the poloidal field formed under these conditions is extremely strong, so that it will cause rapid generation of a toroidal field. However, this approximation is quite suitable for a qualitative discussion on the main features of the interaction between the field and the rotation of the convective zone or to solve the problem of the possible weak interdependence between the distributions of the field and the rotation.

For an adiabatic zone structure the pressure is a function of a single density, and the equation of motion yields

$$(\partial/\partial t)\,\mathrm{curl}\,\mathbf{v}+\mathbf{R}=\mathrm{curl}\,\mathbf{F}, \tag{1}$$

where

$$\mathbf{R}=\mathrm{curl}\,[(\mathrm{curl}\,\mathbf{v})\times\mathbf{v}-(\mathrm{curl}\,\mathbf{B})\times\mathbf{B}/(4\pi\rho)], \tag{2}$$

$\mathbf{v}$ is the hydrodynamic velocity, $\mathbf{B}$ is the magnetic field, $\mathbf{F}$ is the viscous force, and ρ is the density of the medium (the latter is considered to be a known function of the radius r). To this equation we need to add the induction equation. If an approximately steady state is being considered, the vector $\mathbf{R}$ will be determined by the turbulent viscous force, which is a source of entropy production. In order to find the state corresponding to minimum entropy production, we must find the field and velocity distribution corresponding to the lowest average value $|\mathbf{R}|$ over this zone. In order to solve this problem, we shall use a representation of the vectors $\mathbf{v}$ and $\mathbf{B}$ as an expansion in terms of vector spherical harmonics with the coefficients $v_{J0}^{(\lambda)}$ and $B_{J0}^{(\lambda)}$, where $\lambda=0$ or ±1.

For the nonmagnetic case, an expression for $\mathbf{R}$ was given in Ref. 2 and the additional terms arising from the presence of a magnetic field are similar. We shall confine our analysis to the approximation of a thin convective zone. This in fact implies that the entire zone is divided into various thin layers, in each of which the density ρ and the coefficients $v_{J0}^{(\lambda)}$, $B_{J0}^{(\lambda)}$ are taken to be proportional to $r^{-\beta}$, r^{α}, and $r^{(\alpha-\beta/2)}$, respectively, where α and β are constants. As a result, the vector $\mathbf{R}$ will be expressed in terms of a system of algebraic equations. Obviously, in order to obtain a general solution we need to also consider the question of matching the various solutions although the main qualitative characteristics of the model may be studied using the solution for each layer.

The corrections caused by a toroidal field were discussed in Ref. 4. In the presence of a poloidal field a similar additional term in the expression for $\mathbf{R}$ will be given by formula (10) from Ref. 4 if the values of $v_{J_10}^{(-1)}v_{J_20}^{(-1)}$, $\alpha-\beta+2$, and $\alpha+1$ are replaced by $-B_{J_10}^{(-1)}B_{J_20}^{(-1)}/(4\pi\rho)$, $\alpha-\beta/2+2$, and $\alpha-\beta/2+1$, respectively, where the term 2α remains unchanged. In the approximation being discussed we have $B_{J0}^{(+1)}=B_{J0}^{(-1)}(\alpha-\beta/2+2)/[J(J+1)]^{1/2}$. As in Ref. 4, we shall consider a magnetic field antisymmetric with respect to the equatorial plane when the components $B_{J0}^{(\pm1)}$ have odd

TABLE I. Relative angular rotational speed at latitudes between 30° and 90° for models with toroidal (t) and poloidal (p) fields.

Model number	**B**	β	α	$A_{\max}$	Ω/Ω_e				
					30	50	70	80	90
1	t	10	1.237693	0.076	0.9658	0.8961	0.7589	0.6975	0.6735
2	p	10	1.237459	0.257	0.9645	0.9033	0.7775	0.7191	0.6961
3	t	5	1.266446	0.080	0.9653	0.8939	0.7570	0.6964	0.6728
4	p	5	1.264968	0.109	0.9670	0.8796	0.7544	0.7080	0.6908
5	t	10	1.266259	0.062	0.9624	0.8847	0.7437	0.6827	0.6590
6	p	10	1.266876	0.108	0.9621	0.8905	0.7554	0.6954	0.6719
7	p	12	1.261423	0.137	0.9617	0.8925	0.7662	0.7106	0.6888
8	t	5	1.289898	0.078	0.9619	0.8850	0.7382	0.6731	0.6477
9	t	5	1.299598	0.074	0.9575	0.8733	0.7374	0.6814	0.6600
10	p	5	1.291732	0.109	0.9632	0.8684	0.7343	0.6848	0.6665
11	t	10	1.295910	0.059	0.9575	0.8722	0.7280	0.6674	0.6440
12	p	10	1.296663	0.132	0.9578	0.8782	0.7308	0.6658	0.6404
13	p	12	1.297970	0.070	0.9574	0.8786	0.7423	0.6837	0.6609
14	t	20	1.290984	0.043	0.9576	0.8720	0.7259	0.6642	0.6403
15	p	20	1.295698	0.112	0.9546	0.8405	0.8510	0.8970	0.9190
16	t	50	1.291355	0.023	0.9580	0.8713	0.7335	0.6775	0.6560
17	t	10	1.354617	0.080	0.9395	0.8437	0.7288	0.6871	0.6717
18	p	10	1.355307	0.090	0.9532	0.8615	0.7064	0.6409	0.6156

subscripts J. The poloidal velocities are usually small (for models with a toroidal field they are generally zero[4]). We shall subsequently neglect these. In dimensionless variables the relations (3) from Ref. 4 are valid and to these we need to add the expression $\beta_J^{(-1)}=B_{J0}^{(-1)}/[iv_{10}^{(0)}(4\pi\rho)^{1/2}]$, where $J=2k-1$, $k=1,2,\ldots,N$, and N is the number of modes.

The main purpose of our calculations was to identify those characteristics which distinguish the distribution of the rotational speed of the convective zone observed on the Sun from the many other possible distributions. We compared various minimized models obtained assuming that the parameter ε characterizing the value of $|\mathbf{R}|$ introduced in Ref. 2 is smaller than or of the order of 10^{-9}. In this case the average level of entropy production is close to zero.

Since the interaction of rotation with a poloidal magnetic field gives rise to a strong electromagnetic force, the most realistic models are those in which the toroidal field plays a major role. If no poloidal field is present, solar rotation occurs, for example, in a minimized model with $N=4$, $\alpha\approx 1.3$, and $\beta\leqslant 50$ (see Ref. 4). We shall subsequently confine ourselves to studying four-mode models ($N=4$), considering various types of fields and varying the values of α and β. The parameters of various calculated models are given in Table I, where models with a toroidal (poloidal) field are denoted by the letter t (p) in the second column. The value of $A_{\max}$ denotes the highest Alfvén velocity relative to the equatorial rotational speed. A comparison of models 8 and 9 shows that the solution is not single-valued. In our calculations all the parameters of similar different solutions were similar.

For the case $\alpha\approx 1.3$, the distributions of the angular rotational speed Ω for the t-models (models with a toroidal field) are fairly similar to those observed on the Sun. In Fig. 1 these distributions are shown by the heavy solid curve (for $\beta=10$, i.e., $r/R_\odot\approx 0.85$) and by the heavy dashed lines ($\beta=50$, $r/R_\odot\approx 0.96$). Here $R_\odot$ is the radius of the Sun and we use data from the solar model in Ref. 5. In this figure the crosses denote experimental data obtained by Doppler measurements.[6] Moreover, the helioseismological results obtained by Birch and Kosobichev[7,8] for depths with a relative radius greater than 0.96 are shown by the vertical bars whose length characterizes the data spread. It can be seen that the experimental and theoretical curves show satisfactory agreement. Similar agreement between the curves can also be obtained for p-models (models with a poloidal magnetic field), although, as has already been noted, these models are strictly theoretical. We also note that for $\alpha\approx 1.3$ the angular rotational speed is approximately proportional to $r^{0.3}$, which is fairly close to the values of $r^{0.1}$ or $r^{0.2}$ obtained from the helioseismological data obtained by Schou *et al.*[9] for the main part of the convective zone at latitudes of 0 or 30°. Some discrepancies arise at high latitudes, and the reason for this has yet to be explained.

The following formulation of the problem is of interest. We shall assume that the initial toroidal field varies slowly and a poloidal component appears. If its rotation distribution is constrained to comply with the condition of minimum entropy production, the rotation will also be redistributed during the process. The direction of displacement of the model parameters can be assessed by comparing the characteristics of $t-p$ pairs, where a pair is formed by two models with different types of field but having the same or approximately the same values of β and α. In Table II we give the mean-square difference σ between the angular speeds in $t-p$ pairs, considering these differences at latitudes of 0, 5, 10, . . . ,90°. It is interesting that in the rotation observed on the Sun, the difference σ reaches a minimum if we are considering the lower half of the convective zone, for which $5\leqslant\beta\leqslant 10$ (see

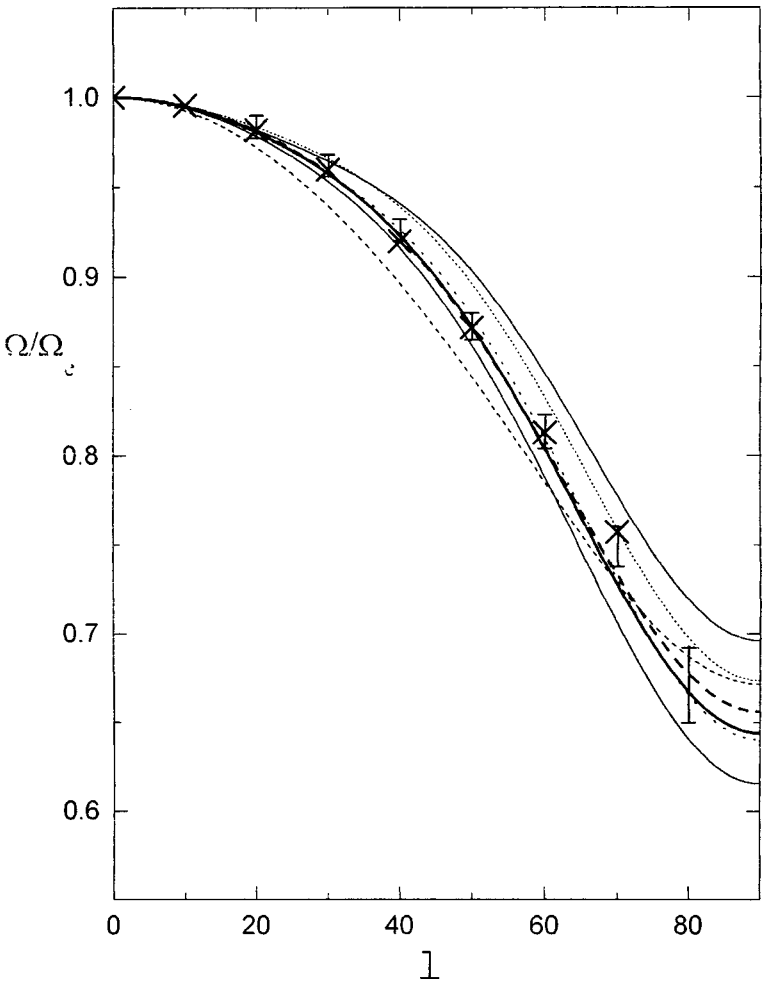

FIG. 1. Angular rotational speed Ω normalized to the angular speed at the equator Ω_e plotted as a function of latitude l (in degrees) for models 1 (closely spaced points), 2 (upper solid curve), 11 (thick solid curve), 12 (widely spaced points), 16 (dashed curve), 17 (short dashes), and No. 18 (lower solid curve) from Table I. The crosses and vertical bars give the experimental results from Ref. 6 and Refs. 7 and 8, respectively.

models 9–12 in Table I). This interval approximately corresponds to $0.73 \leqslant r/R_\odot \leqslant 0.85$. For $\beta = 10$ and $\alpha \approx 1.3$ the distributions of the angular speeds in a $t-p$ pair are shown by the heavy solid curve in Fig. 1 and by the widely spaced dots. These curves are similar.

If β is slightly greater than 10 and $\alpha \approx 1.3$, substantial differences are observed in the rotation behavior in the $t-p$ pair. In this case any processes of spontaneous magnetic field generation will probably be impeded because they should be accompanied either by considerable variations in the rotation distribution of the medium or by changes in the average level of entropy production. A similar situation also arises when we change over to models with different values of the radial gradient of the angular rotational speed. In Fig. 1 the different law of rotation of the minimized models in $t-p$ pairs is indicated by the two upper curves for a small radial gradient (closely spaced points and solid curve corresponding to models 1 and 2 in Table I) and also by the two lower curves for large gradients (short dashes and solid curve corresponding to models 17 and 18 in Table I).

We know that in the seventeenth century the level of solar activity was very low (the Maunder minimum) and the equatorial speed was 3–4% higher than the modern value for approximately the same rotational speed at mid latitudes.[10] For the t-model 17 in Table I (short dashes in Fig. 1) we would obtain a 2–3% increase in the equatorial speed under the same conditions. On this basis we can conclude that the field generation processes were most probably impaired for the distribution of the rotation of the convective zone noted in Ref. 10.

These results indicate that:

a) A state corresponding to a minimum level of entropy production is established in the solar convective zone;

b) This zone contains a magnetic field needed to achieve this state;

c) The present distribution of the rotation of the convective zone is maintained in a state where in most of the zone (i.e., in its lower half) the condition of weak interdependence is satisfied between the rotation distribution and the nature of the field.

TABLE II. Mean-square differences σ between the relative angular speeds in $t-p$ pairs from Table I.

Pair	1−2	3−4	5−6	9−10	11−12	14−15	17−18
σ	1.23×10^{-2}	9.4×10^{-3}	7.6×10^{-3}	4.5×10^{-3}	3.3×10^{-3}	1.2×10^{-1}	2.5×10^{-2}

If this last condition is satisfied, magnetic field generation processes can easily occur. It is probably energetically more favorable to expend energy incoming from the depths on field generation than to transport this energy over distances of order a hundred thousand kilometers by exciting convective motion. In our models, a typical field is around 10 kG (Ref. 4), and then approximately 0.1% of all the energy produced by the Sun can be expended in generating the magnetic field. Naturally, in these field generation processes an important role should be ascribed to asymmetric modes which are directly responsible for sustaining this state with minimum entropy production. If this is the case, then with the Sun we have another example of the formation of regular chaotic structures (see the problem discussed in Ref. 11).

This work was supported financially by the Foundation of the St. Petersburg Educational and Scientific Center of the Russian Ministry of Education and the Russian Academy of Sciences ''Electrophysics of High-Density Currents and Strong Magnetic Fields.''

[1] Yu. V. Vandakurov, in *Proceedings of the Conference on the New Cycle of Solar Activity*, Pulkovo, St. Petersburg (1998) [in Russian], pp. 23–27.
[2] Yu. V. Vandakurov, Zh. Tekh. Fiz. in press (1999).
[3] I. Prigogine, *From Being to Becoming: Time and Complexity in the Physical Sciences* (Freeman, San Francisco, 1980; Nauka, Moscow, 1985, 327 pp.).
[4] Yu. V. Vandakurov, Pis'ma Zh. Tekh. Fiz. **25**(10), 82 (1999) [Tech. Phys. Lett. **25**, 415 (1999)].
[5] D. B. Guenther, P. Demargue, Y. -C. Kim, and M. H. Pinsonneault, Astrophys. J. **387**, 372 (1992).
[6] R. Howard, Annu. Rev. Astron. Astrophys. **22**, 131 (1984).
[7] A. C. Birch and A. G. Kosovichev, Astrophys. J. Lett. **503**, L187 (1998).
[8] A. C. Birch and A. G. Kosovichev, in *Proceedings of SOHO 6/GONG 98 Workshop*, Boston, 1998, Vol. 2, pp. 679–684.
[9] J. Schou, Astrophys. J. **505**, 390 (1998).
[10] J. A. Eddy, P. A. Gilman, and D. E. Trotter, Science **198**, 824 (1977).
[11] Yu. L. Klimontovich, *Turbulent Motion and Structure of Chaos* [in Russian], Nauka, Moscow (1990), 317 pp.

Translated by R. M. Durham

Investigation of oxidation and segregation processes at the surface of titanium nickelide

S. P. Belyaev, F. Z. Gil'mutdinov, and O. M. Kanunnikova

Physicotechnical Institute, Urals Branch of the Russian Academy of Sciences, Izhevsk
V. I. Smirnov Research Institute of Mathematics and Mechanics, St. Petersburg State University
(Submitted March 28, 1999)
Pis'ma Zh. Tekh. Fiz. **25**, 89–94 (July 12, 1999)

The chemical composition of the surface of the equiatomic alloy TiNi was studied using x-ray electron spectroscopy. It is shown that titanium nickelide shows a tendency toward titanium segregation at the free surface. After thermal action in vacuum and in air, the fraction of titanium atoms in the surface layer reaches 98% of the total content of titanium and nickel. Under heat treatment in air an oxidized layer forms at the surface whose main component is TiO_2. © *1999 American Institute of Physics.* [S1063-7850(99)01607-9]

The martensitic transformation in TiNi-based alloys is an athermal process whose rate is completely determined by the rate of temperature change near thermodynamic phase equilibrium. Hence all the specific mechanical effects in TiNi accompanying a martensitic transformation, such as shape memory and transformation plasticity, can take place within extremely short times in suitable heating or cooling regimes. In high-speed devices, thin strips, wires, and tubes having linear cross-sectional dimensions of a few micron are used to enhance the exchange of heat with a liquid or gaseous coolant. In this case, the state of the free surface of the alloy acquires major importance. Since even small variations in composition change the temperature kinetics and completeness of the transformation, segregation of elements and oxidation of the surface substantially alter the special properties of the material. This factor is especially important because of the need for preliminary thermal or thermomechanical treatment of the material. In view of this, the aim of the present paper was to study changes in the surface composition of the TiNi alloy as a result of thermal treatment.

The chemical composition of the surface was analyzed by x-ray electron spectroscopy using an ÉS-2401 spectrometer. The spectra of the internal electron levels were excited with 1253.6 eV MgK_α radiation. Bombardment with 1 keV argon ions was used for a layer-by-layer analysis and to purify the surface in vacuum. The samples measured $9\times9\times1$ mm and were cut from plates of Ti–50.2 at.% Ni alloy. After rolling, the plates were annealed in air at 825 K, the surface layer was then removed by etching followed by thorough washing. At room temperature the material was in the martensitic state.

An analysis of the x-ray electron spectra showed that the surface composition of the plates initially differs from the bulk composition of the alloy. Even at room temperature the surface is highly enriched in titanium. In a layer ≈5 nm thick the ratio $C_{Ti}:C_{Ni}$ of the titanium concentration to the nickel concentration is 92 : 8. As a result of interaction with oxygen in the air the surface is oxidized to a depth of up to 7 nm with the nickel oxidized to a smaller depth (up to 1–2 nm) compared with titanium which is consistent with its lower affinity to oxygen. Titanium is oxidized to the Ti^{4+} state and nickel to Ni^{2+} (Fig. 1a). Most of the oxide film is TiO_2. From the surface into the matrix we observe a gradual transition from higher oxides of titanium to lower ones and then to suboxides. Oxidized nickel (NiO) interacts with some of the titanium oxide to form $NiO\cdot2TiO_2$. In addition, the measurements showed that a layer of up to 3–5 nm contains a negligible quantity of nitrogen (2–4%) which does not participate in forming new compounds.

It would be natural to assume that the excess titanium observed at the surface is merely attributable to the characteristics of the interaction of Ti and Ni atoms with oxygen in the air. In order to eliminate the influence of the external medium, we studied the temperature kinetics of the change in the surface composition in the vacuum chamber of a spectrometer at 10^{-5} Pa pressure. The surface was first cleaned of oxide film by ion bombardment. After cleaning in vacuum, the ratio of the Ti and Ni concentrations was $\approx50:50$, i.e., it was the same as that in the bulk of the sample. The sample was then heated gradually, being held at each temperature for 10 min. The temperature dependence of the surface composition is shown in Fig. 2. It can be seen that from 370 K the surface becomes highly enriched in titanium. In the range 370–510 K the titanium content increases to 90% of the total Ti and Ni content. Under further heating C_{Ti} increases slightly more slowly and at 660 K is 98%. The layer of modified composition is less than 7 nm thick, with the surface layer ≈1 nm thick being most enriched. It can thus be confirmed that the segregation of titanium at the free surface in TiNi is not related to the presence or absence of a medium in contact with the metal.

The observed titanium enrichment of the surface agrees with the method of predicting changes in the composition of the surface layers of multicomponent alloys proposed in Ref. 1. The method is based on the known correlation of the free surface energy and the surface tension of a material with its melting point. Segregation should occur in the direction of varying concentration of the components, corresponding to the minimum of the liquidus curve on the phase diagram of

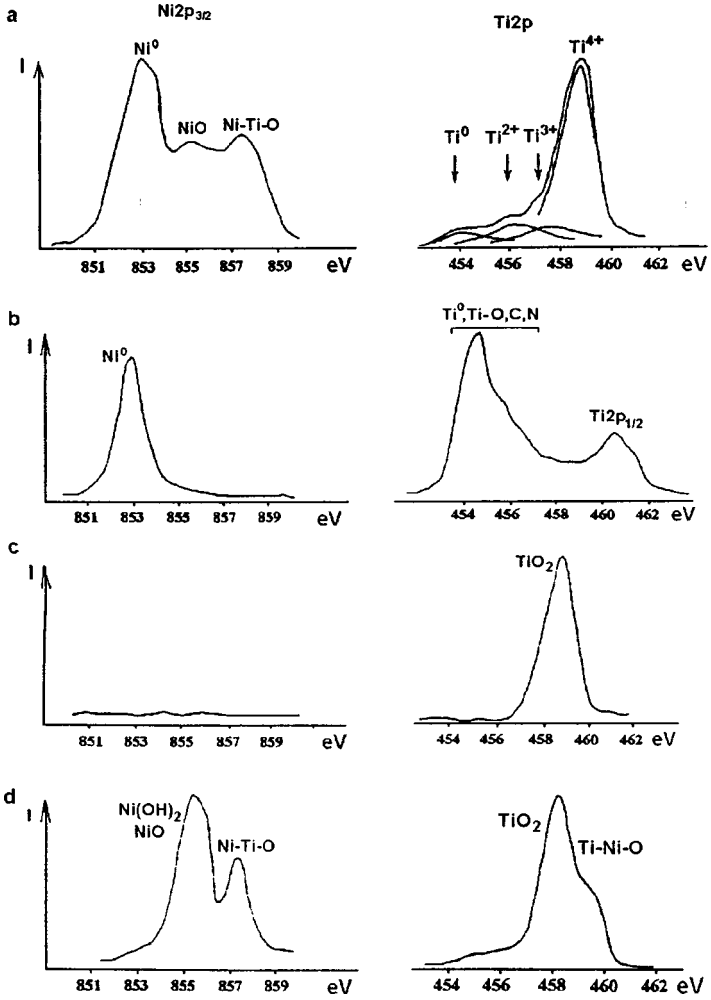

FIG. 1. X-ray electron spectra of the Ni2$p_{3/2}$ and Ti2p surface of TiNi oxidized at room temperature in air in the initial state (a), after heating in vacuum at $T=660$ K (b), after annealing at $T=770$ K (c), and after heat treatment at 1070 K for 1 h (d).

this system. For TiNi alloy this rule corresponds to an increase in the titanium concentration at the surface.

Note that an analysis of the spectra of Ti and Ni (Fig. 1b), C, O, and N after heating has ended reveals the presence of titanium carbides, nitrides, and suboxides in a layer of angstrom thickness which is a result of interaction between the segregated metal and residual gas molecules and atoms in the spectrometer chamber. Nickel is not oxidized under these conditions. The selective oxidation of titanium intensifies the titanium enrichment of the surface as well as the segregation effect. Obviously, ultrahigh vacuum conditions with oil-free pumping of the vacuum chamber are required to obtain an atomically clean TiNi surface.

We shall analyze the results obtained for samples which had undergone preliminary heat treatment. Homogenizing quenching from 1070 K and stabilizing annealing at 770 K are frequently used for TiNi alloys. In the present case we studied the surface state of samples annealed in air for 3 h at 770 K and cooled within the furnace, and also samples quenched in water from 1070 K after being held for 0.5 h and 1 h.

A typical feature of all the regimes was the formation of a thick clinker, whose main component was TiO_2 (Figs. 1c and 1d) which is converted to lower oxides with increasing depth (Ti_2O_3, TiO, suboxides). As for the surface of samples heated in vacuum, the clinker was depleted in nickel to 1–2 at.%. The only exception is a thin layer 1–5 nm thick. Here absolutely no nickel is observed in the annealed samples, whereas the quenched samples held for 0.5 and 1 h reveal an increased nickel content: 3.5% and 10–20% of the total Ti and Ni content, respectively. In the annealed samples most of the nickel is not oxidized, whereas in the quenched samples it is oxidized to the Ni^{2+} state and forms the hy-

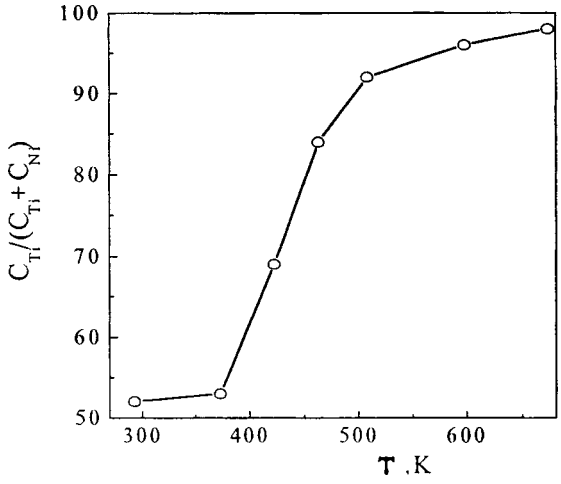

FIG. 2. Change in the titanium concentration at the surface of TiNi under heating in vacuum.

droxide $Ni(OH)_2$ and the compound $NiO \cdot 2TiO_2$. Most of the nitrogen in the clinker is in the atomic state. The thickness of the oxidized surface layer of the heat-treated samples is evidently a few microns. In any case, it could not be removed by ion etching for 2.5 h at a rate of 5 nm/min.

Thus, these investigations have shown that titanium nickelide tends to exhibit titanium segregation at the free surface under heat treatment. In an oxygen-containing atmosphere the alloy is oxidized to form an oxidized layer mainly containing TiO_2. We can assume that since titanium is chemically highly active, in an oxygen-free medium the titanium atoms will form compounds with any noninert gas, for example, nitrides in a nitrogen atmosphere. Moreover, bearing in mind the known correlation between segregation at the free surface and internal interfaces, we can predict that the grain boundaries will be enriched in titanium. Under high-temperature treatment in air, regions having a high titanium content will certainly sorb oxygen, promoting brittle intergranular fracture (catastrophic embrittlement of thin TiNi wires was observed in our experiments). The formation of oxides along grain boundaries and at the surface can only be avoided by heat-treating the samples in vacuum or in an inert medium.

The observed phenomenon of titanium segregation is extremely important from the point of view of analyzing the characteristics of a martensitic transformation in titanium nickelide. Enrichment of the surface in titanium implies depletion of the matrix. However, as we well know, even small deviations of the TiNi composition from stoichiometric lead to changes in the kinetics and sequence of martensitic transformations.[2] If there is a deviation from stoichiometric by a few percent in the direction of one of the elements, no transformation can take place. Consequently, segregation causes an appreciable increase in the dispersion of the material properties relative to martensitic transformations, which must be taken into account when interpreting the results of a structural analysis. We also note that the reverse influence of a diffusion-free transformation on segregation processes cannot be eliminated. This is indirectly indicated by the results of differential thermal analysis, according to which martensitic rearrangement of the lattice occurs when these samples are heated in the range 340–365 K and, as can be seen from Fig. 2, a rapid increase in the titanium concentration at the surface is observed directly after the transformation has been completed.

This work was carried out with assistance from the program ''State Support of Leading Scientific Establishments of the Russian Federation'' 96-15-96-66.

[1] F. Z. Gil'mutdinov and O. M. Kanunnikova, Fiz. Met. Metalloved. **84**(2), 78 (1997).
[2] V. N. Khachin, V. G. Pushin, and V. V. Kondrat'ev, *Titanium Nickelide: Structure and Properties* [in Russian], Nauka, Moscow (1992), 160 pp.

Translated by R. M. Durham

Properties of $Ba_xSr_{1-x}TiO_3$ films grown by rf magnetron sputtering on sapphire with an $SrTiO_3$ sublayer

E. K. Hollmann, V. I. Gol'drin, V. E. Loginov, A. M. Prudan, and A. V. Zemtsov

State Electrotechnical University (LETI), St. Petersburg, Russia
(Submitted March 31, 1999)
Pis'ma Zh. Tekh. Fiz. **25**, 1–5 (July 26, 1999)

Results are presented of experiments to deposit barium strontium titanate films on an *r*-cut sapphire substrate with a strontium titanate sublayer. It is shown that the use of a strontium titanate sublayer can ensure that the dielectric properties of barium strontium titanate films have a weak temperature dependence over a wide temperature range. Moreover, the parameters of the films are consistent with those required to fabricate microwave microelectronics devices.
 [S1063-7850(99)01707-3]

Ferroelectric films, especially $Ba_xSr_{1-x}TiO_3$, are being actively used to fabricate promising rf/microwave microelectronics devices designed to operate at room temperature. The main requirements for the properties of these films are high dielectric nonlinearity, low leakage currents (the loss tangent should not exceed 10^{-2}), and highly stable properties over the operating temperature range. The temperature range in which the nonlinear properties of $Ba_xSr_{1-x}TiO_3$ films are used varies with x, between cryogenic temperatures, $x=0$, and temperatures appreciably higher than room temperature, $x=1$ (Ref. 1). The typical change in the permittivity from its maximum to that at the upper limit of the operating temperature range is at least 80% (Refs. 2 and 3).

The present paper deals with the development of the technology required to fabricate barium strontium titanate (BST) films on *r*-cut sapphire by rf magnetron sputtering and reports an investigation of their electrophysical properties.

Barium strontium titanate films were deposited using a Leybold Z-400 system by sputtering a synthesized ferroelectric target onto (1102)-oriented single-crystal Al_2O_3 wafers on which ~ 800 Å thick $SrTiO_3$ layers had previously been deposited *ex situ*.[4] The parameters of the BST film deposition process are given in Table I.

After deposition all the samples were cooled for 60 min in pure oxygen at atmospheric pressure. Before the deposition process, the target was sputtered away from the substrate holder at the same rf power and a mixture pressure of 8 Pa (Ar/O_2 ratio = 25/75); during the first ten minutes of the deposition process the pressure varied linearly up to the working pressure, as did the Ar/O_2 ratio.

The crystal structure of the films was investigated by x-ray structural analysis using a Geigerflex Rigaku-D/max system. The BST films exhibit regions of (100), (110), and (111) orientation which is consistent with the x-ray diffraction patterns of the strontium titanate sublayers. The regions of (100) and (110) orientation occupy the largest volume. An analysis of the detailed structure of the highest-intensity (200) and (110) peaks in Fig. 1a reveals that in addition to the low-intensity peaks corresponding to the strontium titanate buffer layer, the left edge of the peak exhibits appreciable asymmetry and is somewhat elongated. However, for samples fabricated at the maximum substrate temperature (850 °C) this anomaly of the (200) and (110) peaks is not observed (Fig. 1b). We postulate that this asymmetric peak profile occurs because $Ba_xSr_{1-x}TiO_3$ solid solutions having x between zero and at least 0.65 form during the deposition process. It should be noted that this analysis was made using a standard method of expanding the peaks in Gauss and Cauchy functions, which is implemented using the x-ray analysis system described above.

In addition to studying the crystal structure of these samples, we also investigated the dielectric properties of the film for which we fabricated planar capacitors with copper plates and a gap between 6 and 10 μm wide. The capacitor parameters were measured at the frequency $f=1$ MHz using a technique described in Ref. 4. For all the samples we obtained an extremely weak dependence of the capacitance on temperature $C(T)$. A typical curve is plotted in Fig. 2. For all the samples the loss tangent $\tan\delta$ was less than 0.015, and in some cases it was below the sensitivity threshold of

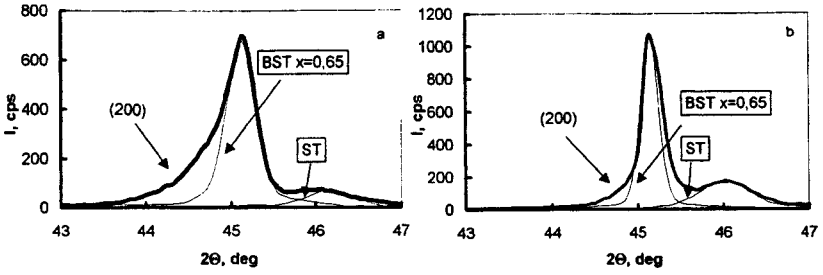

FIG. 1. X-ray peak (200) for sample fabricated at substrate temperatures: a — 760 °C, b — 850 °C.

TABLE I.

Residual gas pressure	$\sim 10^{-4}$ Pa (turbomolecular pump)
Target	$Ba_{0.65}Sr_{0.35}TiO_3$ Diameter 76 mm, thickness 4 mm
Working atmosphere	$Ar-O_2$ mixture; $p(Ar)=p(O_2)=2$ Pa
Rf discharge power	180 W
Deposition time	180 min
Substrate holder temperature	650–850 °C
Target–substrate distance	3 cm
Preliminary sputtering time	15 min

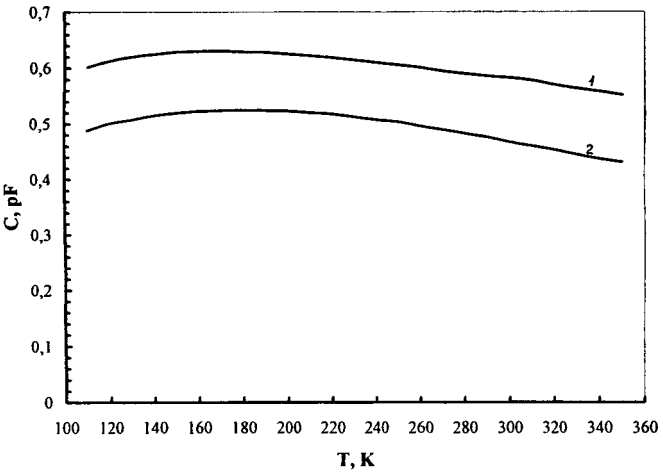

FIG. 2. Capacitance of planar capacitors fabricated using BST films as a function of temperature in the absence of a bias field, $f=1$ MHz, and different substrate temperatures T_1: *1* — $T_1=760$ °C, *2* — $T_1=850$ °C.

the devices (less than 0.0025). The change in the capacitance when a static field $E=200$ MV/m was applied was 40% for the best samples at $T=300$ K.

Capacitor sandwich structures proposed in Ref. 2 were fabricated to check that these films could be used in the microwave. They were investigated at 1.3 GHz. As a result, we found that the controllability is around 75% for a bias field $E=40$ MV/m, and $\tan\delta\approx 0.025$. The high temperature stability of the dielectric properties is thus preserved.

To sum up, we have shown that by depositing thin films of barium strontium titanate on a sapphire substrate using a strontium titanate sublayer, we can achieve acceptable parameters for microwave microelectronics devices with high temperature stability. We postulate that the temperature stability of the dielectric properties is related to the structural effect noted above.

[1] N. N. Antonov, I. M. Buzin, O. G. Vendik *et al.*, in *Ferroelectrics in Microwave Technology*, edited by O. G. Vendik [in Russian], Sovetskoe Radio, Moscow (1979).
[2] A. M. Prudan, E. K. Gol'man, A. B. Kozyrev, A. A. Kozlov, V. E. Loginov, and A. V. Zemtsov, Fiz. Tverd. Tela (St. Petersburg) **40**, 1473 (1998) [Phys. Solid State **40**, 1339 (1998)].
[3] L. A. Knauss, J. M. Pond, J. S. Horwitz *et al.*, Appl. Phys. Lett. **69**, 25 (1996).
[4] V. E. Loginov, E. K. Hollmann, A. B. Kozyrev, and A. M. Prudan, Vacuum **51**, 141 (1998).

Translated by R. M. Durham

Giant change in the optical absorption of an $La_{0.35}Pr_{0.35}Ca_{0.3}MnO_3$ film near a metal–insulator transition and its possible application

Yu. P. Sukhorukov, N. N. Loshkareva, E. A. Gan'shina, A. R. Kaul', O. Yu. Gorbenko, and K. A. Fatieva

Institute of Metal Physics, Urals Branch of the Russian Academy of Sciences, Ekaterinburg
M. V. Lomonosov Moscow State University
(Submitted April 14, 1999)
Pis'ma Zh. Tekh. Fiz. **25**, 6–13 (July 26, 1999)

The absorption spectra of a single-crystal $La_{0.35}Pr_{0.35}Ca_{0.3}MnO_3$ film were studied in the spectral range 0.1–1.6 eV at temperatures between 80 and 295 K. The metal–insulator transition in the temperature range 160–180 K was accompanied by an abrupt increase in the intensity of the transmitted light by a factor of ~400. An applied magnetic field of 0.8 T causes a 55% relative change in the intensity near the transition. The prospects for using these effects to create magnetically controlled optical devices are considered. [S1063-7850(99)01807-8]

Manganites having a perovskite-like structure, recently the subject of intensive studies, are promising materials for various devices using the colossal magnetoresistance effect observed in these compounds over a wide range of temperature. The colossal magnetoresistance effect is associated with a metal–insulator transition which usually takes place near a ferromagnetic–paramagnetic magnetic phase transition.[1] The abrupt change in the electrical resistance of single-crystal $La_{2/3}Ca_{1/3}MnO_{3+\delta}$ films accompanying the metal–insulator transition and the high optical absorption over a wide spectral range form the basis for developing electromagnetic radiation detectors or bolometers.[2] We recently reported[3] the influence of a magnetic field on the absorption coefficient of a $La_{0.9}Sr_{0.1}MnO_3$ single crystal. The relative change in the absorption at 3.8 μm is ~30% in a field of 0.8 T at 140 K, which indicates that manganites having a perovskite-like structure may be used for magnetically controlled optical devices. Here we present results of a study of the absorption spectra of a single-crystal film of a $La_{0.35}Pr_{0.35}Ca_{0.3}MnO_3$ solid solution. This compound was selected because its electrical resistance has a sharp maximum in a narrow temperature range and it has a high magnetoresistance in fields of less than 1 T (Ref. 4).

A 300 nm thick $La_{0.35}Pr_{0.35}Ca_{0.3}MnO_3$ film was grown by chemical vapor deposition on a (001)-oriented single-crystal $SrTiO_3$ substrate at 750 °C and an oxygen partial pressure of 0.003 atm. Investigations made by x-ray diffraction, Raman spectroscopy, and high-resolution transmission electron microscopy indicate that the film is epitaxial and possesses structural and chemical homogeneity.[5,6] The absorption spectra were measured in the range 0.8–12 μm (0.1–1.6 eV), at temperatures between 80 and 295 K, and magnetic fields up to 1.2 T using an IKS-21 automated infrared spectrometer. The magnetic field was applied in the direction of propagation of the light and perpendicular to the plane of the film. The equatorial Kerr effect was measured at temperatures of 20–300 K in the spectral range 1.4–3.5 eV.

Figure 1 shows the absorption spectra of the $La_{0.35}Pr_{0.35}Ca_{0.3}MnO_3$ film at various temperatures. The choice of temperatures is explained by Fig. 2, which gives the temperature dependence of the light intensity transmitted by the film (I) at $\lambda = 2.4\ \mu$m. The temperature 295 K corresponds to the paramagnetic state of the film and 80 K corresponds to the ferromagnetic state. At 180 K the film exhibits maximum transparency, while below this temperature the transparency drops sharply as a result of an insulator–metal transition. The intensity varies by more than a factor of 400. The temperature dependence of the intensity $I(T)$ (Fig. 2) agrees with that of the electrical resistivity $\rho(T)$ (Fig. 3). The drop in the resistance accompanying an insulator–metal transition varies around four orders of magnitude from 1 $\Omega \cdot$ cm (180 K) to $10^{-4}\ \Omega \cdot$cm (80 K), and the electrical resistance at 295 K is $1.7 \times 10^{-2}\ \Omega \cdot$cm. The transition takes place in a narrow temperature range ~15 deg. An external magnetic field of 0.8 T shifts the electrical resistance and transparency maxima toward higher temperatures and reduces the maximum intensity of the transmitted light. The magnetic field has a substantial influence in a narrow temperature range near the insulator–metal transition. The relative change in the intensity of the transmitted light on application of a magnetic field $\Delta I/I_{H=0} = (I_{H=0} - I_H)/I_{H=0}$ in a field of 0.8 T reaches a maximum of ~55% in the short-wavelength range (at 2.4 μm) and remains appreciable (~40%) up to 11 μm. At maximum transparency (Fig. 1, 180 K curve) in the spectral range being studied, absorption bands are observed at 1.3 μm (~1 eV) and 10 μm (0.12 eV), which correspond to local states. At wavelengths shorter than 3 μm an increase in absorption is observed. On transition to the metal state, the absorption increases over the entire spectral range of 0.8–12 μm. In the ferromagnetic region an external magnetic field has the same effect as cooling, i.e., it increases the absorption (inset to Fig. 1).

An analysis of the absorption spectra of an $La_{0.35}Pr_{0.35}Ca_{0.3}MnO_3$ film in this particular spectral range

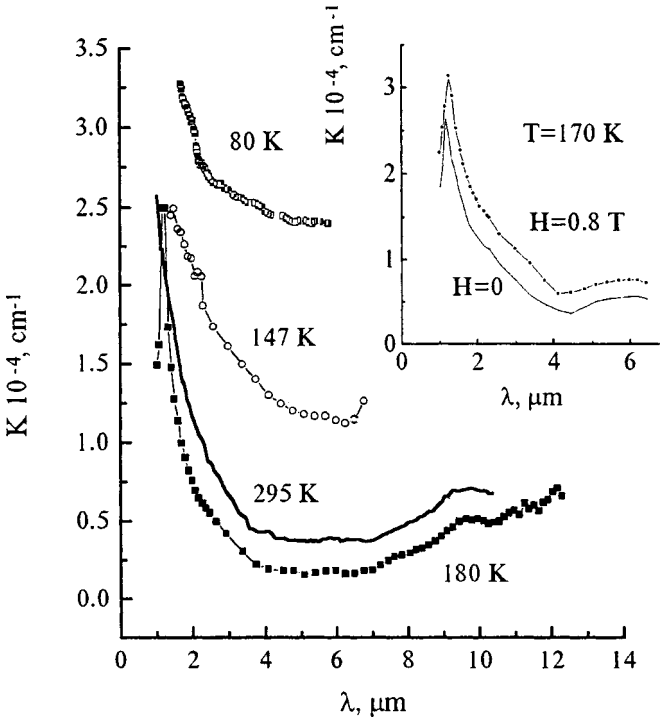

FIG. 1. Absorption spectra of a $La_{0.35}Pr_{0.35}Ca_{0.3}MnO_3$ film at various temperatures. The inset shows the absorption spectra with and without a magnetic field.

suggests that the following factors should be taken into account:

1. The absorption bands at 1.3 and 10 μm, known as mid-infrared (MIR) bands, are a characteristic feature of the spectra of strongly correlated systems. They are observed in the spectra of all cuprate high-temperature superconducting compounds[7] and in the spectra of doped manganites containing manganese ions in different-valence states: in $La_{0.7-y}Pr_yCa_{0.3}MnO_3$ polycrystals,[8] in $La_{0.9}Sr_{0.1}MnO_3$ single crystals,[3] and in $La_{1-x}Ca_xMnO_3$ polycrystals.[9] The nature of these bands is attributable to the strong correlation effect observed when an additional hole or electron is introduced into the base clusters.[10]

2. The spectral weight is redistributed from the high-energy region, where charge-transfer transitions and $d-d$ transitions take place (and in particular, transitions associated with the Jahn–Teller splitting e_g of the levels which are closest in energy[8]), to the low-energy region where interaction between light and carriers is observed when the film is cooled below the Curie temperature. We observed a similar effect when studying the absorption spectrum of a $La_{0.9}Sr_{0.1}MnO_3$ single crystal cooled below T_C (Ref. 3). This redistribution as a function of temperature for $La_{0.7-y}Pr_yCa_{0.3}MnO_3$ (Ref. 8) is similar to the redistribution of the spectral weight of the optical conductivity of $La_{1-x}Sr_xMnO_3$ (Ref. 11) and $La_{2-x}Sr_xCuO_4$ (Ref. 12) single crystals as a function of the Sr concentration, which is also a common feature of strongly correlated systems.[10] The action of this factor in a $La_{0.35}Pr_{0.35}Ca_{0.3}MnO_3$ film causes an overall increase in the absorption when the crystal is cooled below T_C.

3. Interband absorption ''tails.'' The temperature dependence of the transmitted light intensity $I(T)$ in the region where the light interacts with the carriers generally reflects the temperature behavior of the resistance $\rho(T)$. However, for lanthanum manganites with a low level of doping[13] ($x < 0.16$ for $\delta \approx 0$) charge and magnetic phase separation may occur.[1] In this inhomogeneous state the curves of $I(T)$ and $\rho(T)$ may well differ.[9] At high levels of doping as in a

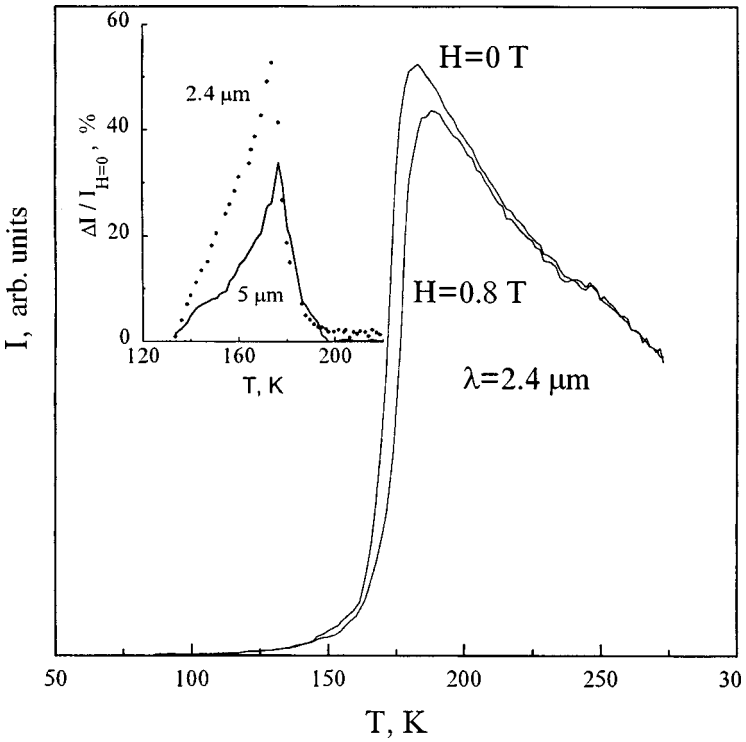

FIG. 2. Temperature dependence of the light intensity transmitted by a $La_{0.35}Pr_{0.35}Ca_{0.3}MnO_3$ film with and without a magnetic field. The inset shows the temperature dependences of the relative change in the intensity of the transmitted light under the action of a 0.8 T magnetic field at fixed wavelengths.

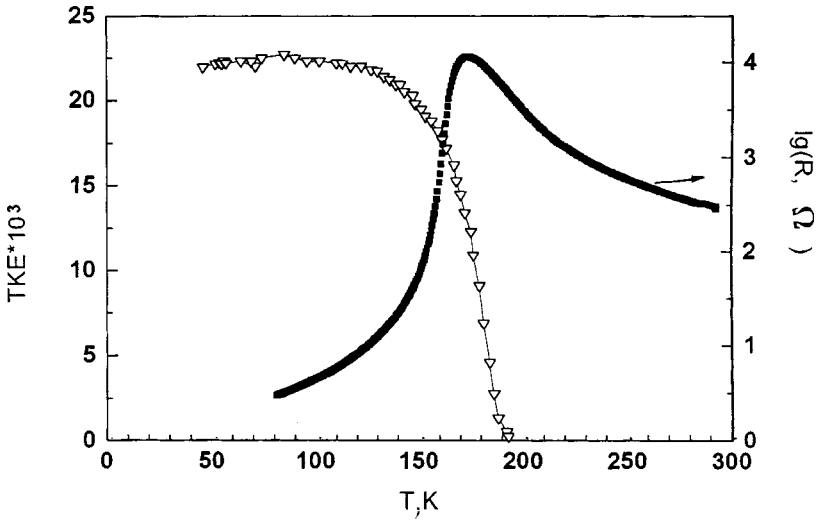

FIG. 3. Temperature dependence of the electrical resistance[4] and the equatorial Kerr effect at 2.3 eV in a 0.1 T magnetic field for a $La_{0.35}Pr_{0.35}Ca_{0.3}MnO_3$ film.

$La_{0.35}Pr_{0.35}Ca_{0.3}MnO_3$ film, a correlation is observed between $I(T)$ and $\rho(T)$ (Figs. 2 and 3).

Measurements of the temperature dependence of the equatorial Kerr effect (Fig. 3) also confirm that a homogeneous ferromagnetic phase appears. The temperature at which the equatorial Kerr effect appears is close to ~ 180 K, the temperature at which an insulator–metal transition occurs (Figs. 2 and 3).

The insulator–metal transition in a $La_{0.35}Pr_{0.35}Ca_{0.3}MnO_3$ film may be attributed to a shift of the mobility edge, which depends on the magnetic disorder.[14] The mobility edge intersects the Fermi level E_F at the insulator–metal transition temperature T_{IM}. Below this temperature the conductivity is of the metallic type, whereas above this it is caused by the activation of carriers at the mobility edge and hopping between localized states. The magnetic field lowers the mobility edge by reducing the magnetic disorder, which leads to a higher transition temperature (Fig. 2).

For a $La_{0.35}Pr_{0.35}Ca_{0.3}MnO_3$ film hysteresis of the transmitted light intensity at a fixed wavelength is observed as a function of the magnetic field. First applying a 0.8 T magnetic field and then switching it off did not restore the initial (before the field was switched on) intensity I_O. The new intensity I_l was $\sim 17\%$ lower than I_O. The intensity I_l was the initial and final point in the measurement of the hysteresis curve $I(H)$. Demagnetizing the film by switching on the field and then reducing it to zero did not restore the initial intensity I_O. All the results relating the influence of the magnetic field on the optical absorption only show good reproducibility when the film is cooled to 80 K in a magnetic field of ~ 0.8 T.

The giant change in the intensity of the transmitted light and the substantial influence of the magnetic field on the absorption of a $La_{0.35}Pr_{0.35}Ca_{0.3}MnO_3$ film near the insulator–metal transition form the basis for developing various optoelectronic devices.

These include an infrared radiation modulator operating in a wide spectral range (1–11 μm) at temperatures near the insulator–metal transition (165–180 K). This operates on the principle that the absorption of the film changes when a magnetic field is applied, i.e., the magnetoabsorption effect. It can be seen from the inset to Fig. 2 that the device has a high percent modulation (up to 55%) and its design is extremely simple, comprising a magnetic field source and a $La_{0.35}Pr_{0.35}Ca_{0.3}MnO_3$ film. The control field may be less than 0.1 T when the field is directed along the plane of the epitaxial film. In Ref. 15 we described a similar device using an $HgCr_2Se_4$ magnetic semiconductor single crystal.

Another device is an optical switch which shuts off infrared radiation when cooled below ~ 140 K. This uses the giant (by a factor of ~ 400) change in the transparency in a narrow temperature range.

Another example is a temperature- and/or magnetic-field-controlled radiation attenuator. If the temperature is maintained within the region of strongly varying intensity $I(T)$, any additional heating increases the transparency, while the application of a magnetic field reduces it.

To sum up, we have observed a giant change in the absorption of a single-crystal $La_{0.35}Pr_{0.35}Ca_{0.3}MnO_3$ film in the infrared near the insulator–metal transition (165–180 K) and we have observed that a magnetic field strongly influences the absorption. The observed effects are attributed to the insulator–metal transition which is caused by the motion of the mobility edge as the temperature and magnetic field vary. Various devices using these effects are proposed.

The authors would like to thank N. G. Bebenin for fruitful discussions of this work.

This work was supported by the Russian Fund for Fundamental Research, Grant No. 99-02-16595.

[1] É. L. Nagaev, Usp. Fiz. Nauk **166**, 833 (1996).
[2] Y. H. Hao, X. T. Zeng, and H. K. Wong, J. Appl. Phys. **79**, 1810 (1996).
[3] N. N. Loshkareva, Yu. P. Sukhorukov, B. A. Gizhevskii *et al.*, Phys. Status Solidi A **164**, 863 (1997).
[4] O. Yu. Gorbenko, A. A. Bosak, A. R. Kaul *et al.*, MRS Proc. **495**, 333 (1998).
[5] O. Yu. Gorbenko, A. R. Kaul, A. A. Bosak *et al.*, in *High Temperature Superconductors and Novel Inorganic Materials* (NATO ASI Series, 1999), pp. 233–238.
[6] B. Guettler, L. Skuja, O. Yu. Gorbenko *et al.*, MRS Proc. **517**, 111 (1998).

[7] G. A. Thomas, D. H. Rapkine, C. L. Cooper *et al.*, Phys. Rev. B **45**, 2474 (1992).
[8] K. H. Kim, J. H. Jung, D. J. Eom *et al.*, Phys. Rev. Lett. **81**, 4983 (1998).
[9] N. N. Loshkareva, Yu. P. Sukhorukov, S. V. Naumov *et al.*, [JETP Lett. **68**, 97 (1998)].
[10] A. S. Moskvin, Physica B **252**, 186 (1998).
[11] L. V. Nomerovannaya, A. A. Makhnev, I. D. Lobov, and A. Yu. Rumyantsev, *Abstracts of the 16th International School/Seminar on New Magnetic Materials for Microelectronics*, Moscow, 1998 [in Russian], Moscow State University Press, pp. 361–362.
[12] S. Usida, T. Ido, H. Takadi, T. Orima *et al.*, Phys. Rev. B **43**, 7942 (1991).
[13] M. Imada, A. Fujimori, and Y. Tokura, Rev. Mod. Phys. **70**, 1039 (1998).
[14] N. G. Bebenin and V. V. Ustinov, J. Phys.: Condens. Matter **10**, 6301 (1998).
[15] N. N. Loshkareva, Yu. P. Sukhorukov, B. A. Gizhevskiĭ, and A. A. Samokhvalov, Pis'ma Zh. Tekh. Fiz. **15**(17), 83 (1989) [Sov. Tech. Phys. Lett. **15**, 698 (1989)].

Translated by R. M. Durham

Investigation of gas diffusion through films of fullerene-containing poly(phenylene oxide)

G. A. Polotskaya, D. V. Andreeva, and G. K. El'yashevich

Institute of Macromolecular Compounds, Russian Academy of Sciences, St. Petersburg
(Submitted December 29, 1998; resubmitted February 15, 1999)
Pis'ma Zh. Tekh. Fiz. **25**, 14–19 (July 26, 1999)

A study is made of the possibility of using fullerene-containing polymers as materials for gas-separating membranes. Fullerene-containing poly(phenylene oxide) was prepared and its density and free volume were estimated. The coefficients of gas permeability and the selectivity factors for separation of air into oxygen and nitrogen were measured for poly(phenylene oxide) having various fullerene contents. A correlation is established between the change in the transport properties and the free volume. It is shown that modifying poly(phenylene oxide) with fullerene is potentially useful for improving the transport properties of the membranes.
 [S1063-7850(99)01907-2]

INTRODUCTION

The new allotropic forms of carbon known as fullerenes (C_{60} and C_{70}) possess unique properties which have been described in various reviews.[1–3] One of the main trends in fullerene research is the development of new materials for engineering and industry. Polymers open up extensive possibilities for the development of such materials. Results of investigations to obtain fullerene-containing polymers were first published in 1992 in Refs. 4 and 5. In a series of studies carried out at the Institute of Macromolecular Compounds of the Russian Academy of Sciences under the guidance of V. N. Zgonnik, in which fullerene-containing polystyrene,[6,7] polyethylene oxide,[8] polymethylmethacrylate,[9] and poly(*N*-vinylpyrrolidone)[10] were studied, it was shown that polymers containing covalently bonded C_{60} substantially modify their initial properties. The studies concentrated mainly on the synthesis process and on examining the structure and molecular mass characteristics using light scattering, mass spectrometry, ultraviolet spectroscopy, NMR, and chromatographic techniques.

As yet no information has been published on studies of gas diffusion through fullerene-containing polymers. Diffusion is used to concentrate and purify gas mixtures using polymer membranes. The fields of application of membrane gas separation are continually expanding, whereas the range of membranes used industrially is currently limited and their properties are far from perfect.

The task for the present study is to prepare a fullerene-containing composite of C_{60} and poly(2,6-dimethyl-1,4-phenylene oxide) (PPO) and to study the diffusion of gas molecules through fullerene-containing PPO with a view to using this material for gas-separating membranes. Poly(phenylene oxide) is known as a construction material having good physicomechanical properties[11] and is produced commercially in many countries, including, among others, Russia, the USA, the Czech Republic, and Japan.

EXPERIMENTAL

Fullerene containing more than 98% C_{60} (Institute of Macromolecular Compounds of the Russian Academy of Sciences) was freed of traces of moisture by heating to 100 °C in vacuum. A toluene solution of C_{60} was used. Commercial PPO having a molecular weight of 170×10^3 (Brno, Czech Republic) was dissolved in chloroform. Films of fullerene-containing PPO were prepared from a solution of C_{60} and PPO in a mixture of toluene and chloroform on a cellophane surface at 40°C.

The density ρ of the films was determined by a flotation method in a saccharose solution at 25 °C. The free volume v_f was calculated using the formula

$$v_f = v_{sp} - 1.3v_w,$$

where $v_{sp}=1/\rho$ is the specific volume and v_w is the van der Waals volume calculated using Bondy's method.

The transport of gas molecules was investigated using a PGD-01 system by passing a stream of air through a film of fullerene-containing PPO located in a diffusion cell at 30 °C and a partial gas pressure gradient of 1 atm. The quantity and composition of the gas leaving the cell was analyzed by a chromatographic method.

DISCUSSION OF RESULTS

When the C_{60} and PPO solutions were mixed, a brownish color appeared that persisted as the mixture condensed, which indicates the probable formation of a complex between C_{60} and PPO. The maximum C_{60} content in this system was 25 wt.%. A further increase in the fullerene content causes the PPO–C_{60} system to become heterogeneous both in solution and in films.

As a result of the complex formation, the structure of the polymer chains can become compacted or, conversely, looser structures may form. In order to explain the structural changes to the PPO macromolecules as a result of adding C_{60}, we determined the density of PPO films having various C_{60} contents and calculated their free volume (see Table I).

TABLE I. Physical properties of poly(phenylene oxide) modified with C_{60}.

C_{60}, wt.%	ρ, kg/m^3	$v_f \times 10^3$, m^3/kg
0	1057	0.181
0.25	1070	0.171
0.5	1088	0.154
1.0	1093	0.150
2.0	1120	0.128

The data presented in Table I indicate that the PPO density (ρ) increases with increasing C_{60} content, i.e., the polymer coils become more compact and the free volume (v_f) of the fullerene-containing PPO decreases.

Physical parameters such as the density and free volume determine many of the practically significant properties of polymers, in particular the transport of small molecules through polymer materials. The transport of gas molecules is estimated quantitatively using the coefficient of gas permeability ($\overline{P}_i$) and the selectivity factor (α) for the separation of gas mixtures. The coefficient of permeability of a gas i depends on the physical nature of the membrane polymer and is given by

$$\overline{P}_i = \frac{V l}{A \tau \Delta p},$$

where V is the gas volume, l is the membrane thickness, A is the membrane area, τ is the time for the gas to permeate, and Δp is the pressure gradient between the sides of the membrane. The gas separation process is based on the different permeability of the membranes for the various components of the gas mixture. The separation selectivity factor is determined by the ratio of the permeability coefficients of the two gases:

$$\alpha_{i/j} = \frac{\overline{P}_i}{\overline{P}_j}.$$

Polymers potentially useful for gas-separating membranes should possess high gas permeability and high selectivity. However, for most polymers these properties are antipathetic and the problem usually involves improving the selectivity of a highly permeable polymer or increasing the permeability of a highly selective polymer.

Poly(phenylene oxide) is one of the most gas-permeable glassy polymers, but it has low selectivity factors for gas separation.[12,13] Attempts have already been made to improve its selectivity using laborious and hazardous methods of chemical modification such as boration, sulfonation, alkylation, and so on,[14–16] but these have not yet been used commercially.

Figure 1 gives the results of measuring the coefficients of permeability of oxygen and nitrogen for PPO and its complexes with C_{60} containing between 0.25 and 2 wt.% C_{60}. It can be seen that when changing from pure PPO to the fullerene-containing polymer, the coefficients of gas permeability decrease; this is accompanied by a slight increase in the selectivity for separating a mixture of these gases from air, from $\alpha = 4.0$ to 4.2. Although the changes in α seem small in magnitude, they substantially exceed the measurement accuracy, so that it can be reliably asserted that the presence of fullerene improves the selectivity. At present

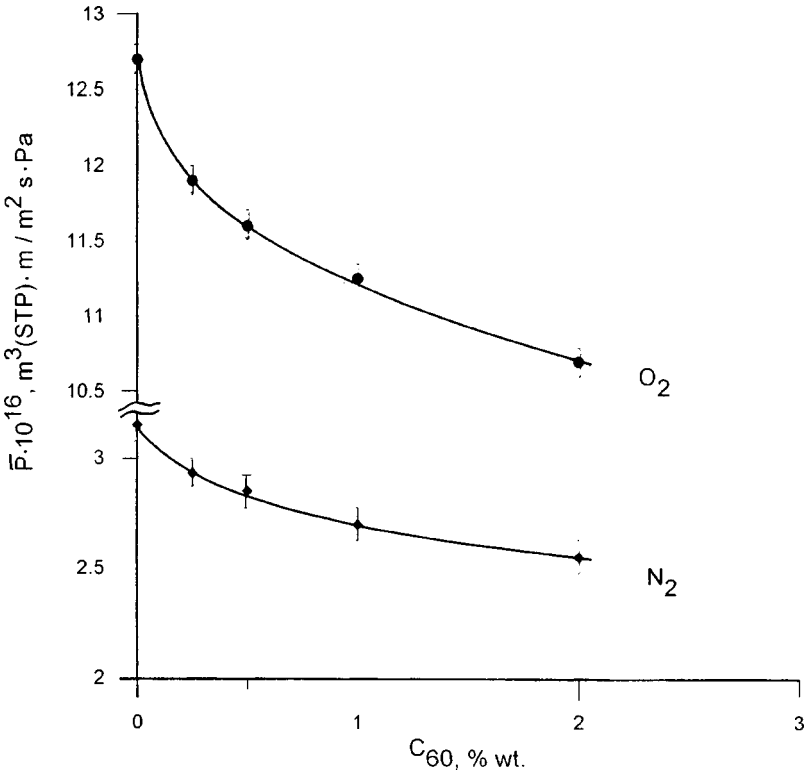

FIG. 1. Permeability coefficients for oxygen and nitrogen versus C_{60} content in PPO films.

membranes with $\alpha(O_2/N_2) \cong 3$ are used industrially and those with $\alpha(O_2/N_2) = 5-6$ are considered to be highly selective.

Note that the established trend of the transport properties correlates with the reduction in the free volume in fullerene-containing PPO compared with pure PPO.

CONCLUSIONS

To sum up, fullerene-containing PPO having an increased density and smaller free volume compared with the initial PPO was prepared by mixing solutions of C_{60} and PPO. These characteristics are responsible for the change in the transport properties of the PPO. The fullerene-containing PPO typically exhibits a lower gas permeability and enhanced selectivity for gas separation. This method of modifying PPO with fullerene to improve the transport properties is the simplest of all those known so far.

[1] V. I. Sokolov and I. V. Stankevich, Usp. Khim. **62**, 455 (1993).
[2] V. P. Belousov, I. M. Belousova, V. P. Budtov, V. V. Danilov, O. B. Danilov, A. G. Kalintsev, and A. A. Mak, Opt. Zh. **64**(12), 3 (1997) [J. Opt. Technol. **64**, 1081 (1997)].
[3] N. F. Gol'dshleger and A. P. Moravskiĭ, Usp. Khim. **66**, 353 (1997).
[4] A. D. Loy and R. A. Assing, J. Am. Chem. Soc. **114**, 3977 (1992).
[5] S. Shi, K. C. Khemani, and F. Wuld, J. Am. Chem. Soc. **114**, 10 656 (1992).
[6] V. N. Zgonnik, E. Yu. Melenevskaya, L. S. Litvinova, E. E. Kever, L. V. Vinogradova, and I. V. Terent'eva, Vysokomol. Soedin., Ser. A **38**, 203 (1996).
[7] E. Yu. Melenevskaya, L. V. Vinogradova, L. S. Litvinova, E. E. Kever, L. A. Shibaev, T. A. Antonova, E. I. Bykova, S. I. Klenin, and V. N. Zgonnik, Vysokomol. Soedin., Ser. A **40**, 247 (1998).
[8] L. V. Vinogradova, E. Yu. Melenevskaya, E. E. Kever, L. A. Shibaev, T. A. Antonova, and V. N. Zgonnik, Vysokomol. Soedin., Ser. A **39**, 1733 (1997).
[9] V. N. Zgonnik, L. V. Vinogradova, E. Yu. Melenevskaya, E. E. Kever, A. V. Novokreshchenova, L. S. Litvinova, and A. S. Khachaturov, Zh. Prikl. Khim. **70**, 1538 (1997).
[10] L. A. Shibaev, T. A. Antonova, L. V. Vinogradova, E. Yu. Melenevskaya, and V. N. Zgonnik, Pis'ma Zh. Tekh. Fiz. **23**(18), 19 (1997) [Tech. Phys. Lett. **23**, 732 (1997)].
[11] *Polymer Encyclopedia*, Vol. 2 [in Russian], Sov. Éntsiklopediya, Moscow (1979), p. 818.
[12] B. D. Bhide and S. A. Stern, J. Membr. Sci. **1**, 37 (1991).
[13] A. E. Polotsky and G. A. Polotskaya, J. Membr. Sci. **140**, 97 (1998).
[14] R. T. Chen, F. R. Shen, L. Jia, D. Stannett, and H. B. Hopfenberg, J. Membr. Sci. **35**, 103 (1987).
[15] B. J. Story and W. J. Koros, J. Membr. Sci. **67**, 191 (1992).
[16] G. A. Polotskaya, S. A. Agranova, T. A. Antonova, and G. K. Elyashevich, J. Appl. Polym. Sci. **66**, 1439 (1997).

Translated by R. M. Durham

High-Q whispering-gallery oscillations in a shielded spherical dielectric cavity

S. N. Khar'kovskiĭ, Yu. F. Filippov, Z. E. Eremenko, A. E. Kogut, and V. V. Kutuzov

A. Ya. Usikov Institute of Radio Physics and Electronics, National Academy of Sciences of Ukraine, Kharkov
(Submitted April 15, 1999)
Pis'ma Zh. Tekh. Fiz. **25**, 20–25 (July 26, 1999)

Results are presented of theoretical and experimental investigations of whispering-gallery oscillations in a shielded isotropic layered spherical dielectric cavity. Oscillations whose Q factor is two orders of magnitude higher than that of the oscillations of an open dielectric sphere are studied. Intermode interaction is observed between various cavity oscillation modes. © *1999 American Institute of Physics.* [S1063-7850(99)02007-8]

The high Q factor of a dielectric cavity using whispering-gallery oscillations is a determining factor for its application over a wide wavelength range between the millimeter and the optical.[1–3]

The boundary-value problem for a homogeneous isotropic sphere has been studied in fairly great detail for arbitrary values of the parameters.[4] It was shown that for an optimum choice of parameters the radiation energy losses to whispering-gallery modes are negligible. Dielectrics with low losses are required to produce high-Q cavities. New possibilities for obtaining an ultrahigh Q factor at low temperatures were identified in studies of the physical mechanisms for anomalously low energy dissipation in dielectric crystals. This low energy dissipation determines the maximum Q factor of these cavities.[3]

In real systems, the operating characteristics of dielectric cavities with whispering-gallery oscillations may deteriorate as a result of external influences. One method of reducing this influence is to shield the cavity. Multilayer spherical cavities are widely used in various physical applications. In particular, they are used to develop stable microwave standards in precision measuring apparatus.[5]

Here we present results of a study of the oscillations in a layered, isotropic, spherical cavity consisting of three regions: a dielectric sphere, a gap, and a metal shell of finite thickness (see inset to Fig. 2). Each region is characterized by the permittivity ε_j $(j=1,2,3)$. Here we have written $\varepsilon_3 = 4i\pi\sigma/\omega$, where σ is the conductivity of the metal surface and ω is the resonant frequency. The depth of penetration of the field in the metal is assumed to be small compared with the thickness of the metal shell.

Two independent oscillation modes form in the structure: transverse electric (TE) modes

$$E_r=0, \quad H_r=\frac{n(n+1)}{r^2}V$$

and transverse magnetic (TM) modes

$$H_r=0, \quad E_r=\frac{n(n+1)}{r^2}U.$$

The wave functions U and V are determined by solutions of a system of Maxwell equations having the form $(\Psi = U, V)$:

$$\Psi=\sum_n R_{\Psi,n}(r)P_n^m(\cos\theta)\exp(i(m\varphi-\omega_p t)).$$

Here r, θ, and φ are spherical coordinates; the subscript p denotes the triple index n, m, l, where n and m are the polar and azimuthal indices, and l is the number of half-waves within the cavity radius; and $P_n^m(\cos\theta)$ is an associated Legendre function. The distribution of the fields of the resonant oscillations over the radial coordinate is given by the function

$$R_{\Psi,n}(r) = \begin{cases} A_{\Psi,n}j_n(kr\sqrt{\varepsilon_1}), & 0\leqslant r\leqslant r_1, \\ B_{\Psi,n}j_n(kr\sqrt{\varepsilon_2})+D_{\Psi,n}\eta_n(kr\sqrt{\varepsilon_2}), & r_1\leqslant r\leqslant r_2, \\ C_{\Psi,n}h_n^{(1)}(kr\sqrt{\varepsilon_3}), & r\geqslant r_2, \end{cases}$$

where

$$k=\omega_p/c; \quad j_n(x)=\sqrt{\frac{\pi x}{2}}J_{n+\frac{1}{2}}(x),$$

$$\eta_n(x)=\sqrt{\frac{\pi x}{2}}N_{n+\frac{1}{2}}(x); \quad h_n^{(1)}(x)=\sqrt{\frac{\pi x}{2}}H^{(1)}_{n+\frac{1}{2}}(x),$$

$J_{n+\frac{1}{2}}(x)$, $N_{n+\frac{1}{2}}(x)$, and $H^{(1)}_{n+\frac{1}{2}}(x)$ are Bessel, Neumann, and Hankel functions of the first kind, $A_{\Psi,n}$, $B_{\Psi,n}$, $C_{\Psi,n}$, and $D_{\Psi,n}$ are constants.

Satisfying the conditions of continuity of the tangential components of the resonant oscillation fields at the interfaces between the media for r equal to r_1 and r_2, we obtain a system of algebraic equations for these constants. The conditions for the existence of nontrivial solutions of this system yield the following characteristic equation, which determines the resonant frequencies and Q factors of the TE and TM modes:

$$(\alpha_\Psi j_{11}'h_{21}^{(1)}-j_{11}h_{21}^{(1)\prime})[\beta_\Psi h_{32}^{(1)\prime}(j_{22}h_{21}^{(1)}-j_{21}h_{22}^{(1)\prime})-(j_{22}'h_{21}^{(1)} - j_{21}h_{21}^{(1)\prime})h_{32}^{(1)}] = ij_{11}(\beta_\Psi h_{22}^{(1)}h_{32}^{(1)\prime}-h_{32}^{(1)}h_{22}^{(1)\prime}). \quad (1)$$

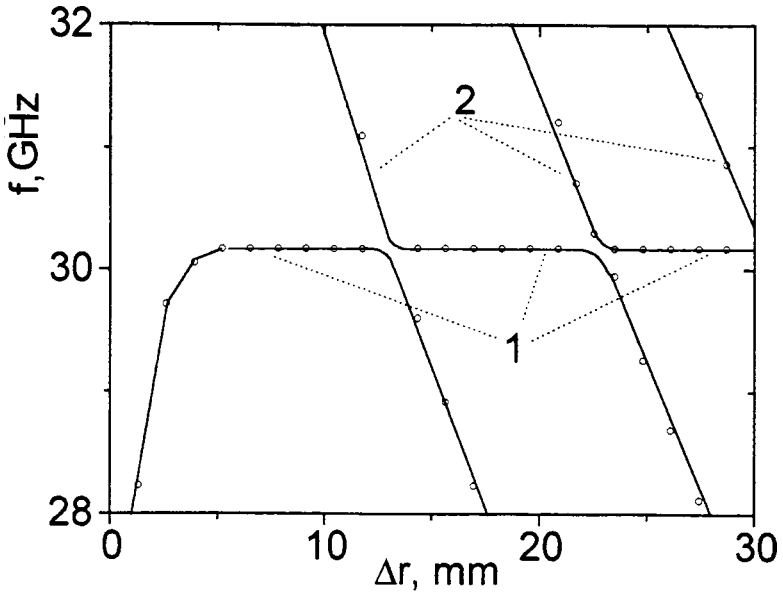

FIG. 1. Frequency of resonant oscillations of the TM mode as a function of the gap Δr for $n=30$: 1 — whispering-gallery oscillations, 2 — volume oscillations in the cavity.

Here we have $g_{ij}=kr_j\sqrt{\varepsilon_i}$, $b_{ij}=b_n(g_{ij})$, $b'_{ij}=b_{n-1}(g_{ij})-\frac{n}{g_{ij}}b_n(g_{ij})$, where the function b implies j or h

$$\alpha_U=\sqrt{\frac{\varepsilon_2}{\varepsilon_1}},\quad \alpha_V=\sqrt{\frac{\varepsilon_1}{\varepsilon_2}},\quad \beta_U=\sqrt{\frac{\varepsilon_2}{\varepsilon_3}},\quad \beta_V=\sqrt{\frac{\varepsilon_3}{\varepsilon_2}}.$$

The first bracket on the left-hand side of this equation describes the spectral parameters of the resonant oscillations in a dielectric sphere, while the second describes the oscillations in the bulk between the surface of the sphere and the metal surface. The right-hand side determines the influence of the interaction between these oscillations.

The results of a numerical investigation of the characteristic equation (1) obtained for the TM mode are plotted in Figs. 1 and 2 for a cavity containing a fluoroplastic dielectric sphere ($\varepsilon_1=2.08$, $\tan\delta=1.8\times10^{-4}$, $r_1=39$ mm), an air gap ($\varepsilon_2=1$), and a spherical copper shield ($\sigma=1.5\times10^{18}\,\mathrm{s}^{-1}$).

Figure 1 gives the resonant frequency $f=\omega/(2\pi)$ as a function of the gap between the dielectric and the metal $\Delta r=(r_2-r_1)$. In a layered cavity the frequency contains two oscillation modes, whispering-gallery modes (1) and a family of volume oscillations in the gap (2). In the range under study, for Δr shorter than the operating wavelength of 10 mm, no volume oscillations occur. To a first approximation the spectral parameters of the whispering-gallery modes are determined by the first bracket in Eq. (1). Note that in the range $0<\Delta r<3$ mm the resonant frequency of these oscillations increases with increasing Δr and then remains constant at the frequency of these oscillations in an open dielectric cavity.

When studying the radial distribution of the energy of the oscillation field in the range $3<\Delta r<10$ nm in the cavity we observed and confirmed experimentally that the whispering-gallery field exhibits a locking effect near the boundary of the dielectric sphere. A similar effect was analyzed by Vaĭnshteĭn[6] in an open cavity with a dielectric prism.

For $\Delta r>10$ mm the frequency of the volume oscillations

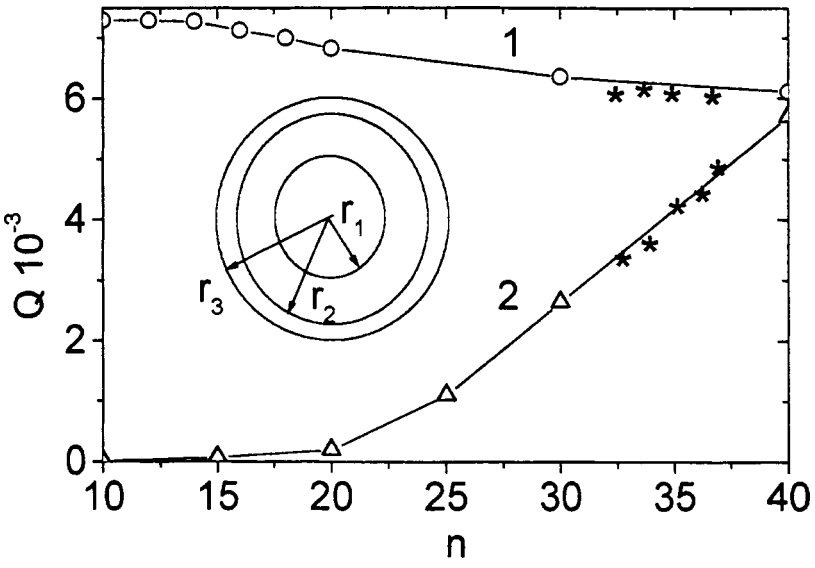

FIG. 2. Q factor of whispering-gallery oscillations of the TM mode as a function of the polar index n for $\Delta r=3$ mm; 1 — whispering-gallery oscillations in a shielded sphere, 2 — in an open sphere, and * — experimental results.

in the gap (Figs. 1 and 2) approaches the frequency of the whispering-gallery oscillations (1). In the range where the frequencies are equal intermode coupling occurs, leading to repulsion of the dispersion curves. This effect was also observed experimentally.

Figure 2 gives the intrinsic Q factor of the TM mode Q as a function of the polar index n for $\Delta r = 3$ mm. It can be seen that as n decreases, the Q factor increases to $Q = 7.3 \times 10^3$, which is higher than the dielectric Q factor $Q = 5.6 \times 10^3$. This is because as the polar index decreases, the volume of the energy of the whispering-gallery oscillation field in the gap decreases. The Q factor stops increasing when the conditions for locking of the field in the dielectric are no longer satisfied because of a change in frequency, since the electric value of the gap is not consistent with the condition for locking of the whispering-gallery oscillations in the air gap. The intrinsic Q factor of the TM oscillations of an open dielectric sphere having the same radius decreases by more than two orders of magnitude when the index n decreases from 40 to 10 because of the increased radiation losses in the sphere.

These effects occur in a hemispherical cavity bounded at $\theta = \pi/2$ by a planar metal mirror. This cavity supports oscillations for which the sum $(n+m)$ is odd for the TM mode and even for the TE modes.[7]

In the experiments one half of the dielectric sphere was replaced by a plane mirror. Whispering-gallery oscillations were excited in this cavity by the tapered end of a hollow metal waveguide via a coupling slit in the mirror. In order to resolve the oscillation spectrum of the shielded cavity, the mirror only partially covered the peripheral part of the plane base of the dielectric hemisphere. The shield was a hollow metal cylinder with a half-circle at the base. In the frequency range 32–37 GHz, the crosses in Fig. 2 show the results of measurements of the intrinsic Q factor of the whispering-gallery modes of a dielectric hemisphere shielded by a cylindrical screen. These results show good agreement with the results of a numerical solution of the characteristic equation (1).

An investigation of the change in the frequency and Q factor of the resonant oscillations when the cavity between a sphere and a metal surface is filled with various media can be effectively used to measure the complex permittivity of these media.

[1] M. E. Il'chenko, V. F. Vzyatyshev, L. G. Gassanov *et al.*, *Dielectric Cavities*, edited by M. E. Il'chenko [in Russian], Moscow (1989), 328 pp.
[2] G. Annino, M. Cassettari, L. Longo *et al.*, IEEE Trans. Microwave Theory Tech. **MTT-45**, 2025 (1997).
[3] V. B. Braginsky, V. S. Ilchenko, and K. S. Bagdassarov, Phys. Lett. A **120**, 300 (1987).
[4] M. Gastine, L. Courtois, and J. L. Dormann, IEEE Trans. Microwave Theory Tech. **MTT-15**, 694 (1967).
[5] S. Sottini, E. Giogetti, and C. Marcelino, Pure Appl. Opt. **1**, 359 (1992).
[6] L. A. Vaĭnshteĭn, *Open Resonators and Open Waveguides*, Golem Pres, Boulder, CO (1969) Russian orig. Sovet-skoe Radio, Moscow (1966), 375 pp.].
[7] Yu. F. Filippov, A. E. Kogut, V. V. Kutuzov, and S. N. Khar'kovskiĭ, Izv. Vyssh. Uchebn. Zaved. Radioélektron. **40**(2), 19 (1997).

Translated by R. M. Durham

Real structure of $Cd_2Nb_2O_7$ pyrochlore single crystals

I. L. Shul'pina, N. N. Kolpakova, M. P. Shcheglov, and A. O. Lebedev

A. F. Ioffe Physicotechnical Institute, Russian Academy of Sciences, St. Petersburg
(Submitted April 23, 1999)
Pis'ma Zh. Tekh. Fiz. **25**, 26–33 (July 26, 1999)

X-ray topography and diffractometry are used to study the crystal structure of cadmium pyroniobate $Cd_2Nb_2O_7$ at room temperature. Structural quality parameters were determined for crystals grown with different degrees of impurity doping. The nature of the crystal lattice damage is analyzed as a function of the type and concentration of impurities. © *1999 American Institute of Physics.* [S1063-7850(99)02107-2]

Cadmium pyroniobate $Cd_2Nb_2O_7$ has a pyrochlore structure (general formula $A_2B_2O_7$, space group Fd3m-O_h^7) and is the only example of a compound in which a phase transition is observed to the ferroelectric state ($T_c = 196$ K) from such a highly symmetric space group.[1] A characteristic feature of this phase transition is that below T_c a disordered (relaxor) state appears in addition to the ordered (ferroelectric) state.[2] The appearance of a disordered state in the system and its evolution with temperature are caused by a gradual ''freezing'' of the off-center displacements of the Cd^{2+} ions, which at room temperature (paraelectric phase) are dynamically localized in the $(CdO_8)^{n-}$ sublattice.[2,3] Impurities and lattice defects intensify the relaxor properties of disordered systems[4,5] although the mechanism for this behavior has not been established. In order to identify the macroscopic mechanism for structural disorder and the reasons for the coexistence of disordered and ordered states in the ferroelectric phase ($T<T_c$), we need to make a detailed analysis of the damage to the structure of $Cd_2Nb_2O_7$ crystals in the preceding phase ($T>T_c$). Such investigations have yet to be made for compounds having a pyrochlore structure, and this motivated the present study.

Undoped and doped crystals of cadmium pyroniobate $Cd_2Nb_2O_7$ were grown by spontaneous crystallization using a boric acid catalyst. The undoped crystals grown in different experiments were differently colored (colorless, yellow, orange, and reddish brown).[5] The doped crystals contained different species (Fe, Ni, Cu, Zn, and Gd) and different concentrations ($0.02 \leqslant x \leqslant 0.2$). Their color varied, depending on the dopant. For example, Gd- and Zn-doped crystals were typically light yellow and yellow, Cu-doped crystals were reddish brown, and Fe- and Ni-doped crystals were orange and orange-brown.

An x-ray structural analysis of control samples of doped and undoped crystals by powder diffractometry using an internal Si standard (DRON-1, CuK_α radiation) showed that these have a pyrochlore structure.[1,3] No other phase was identified in the crystals.

Damage to the crystal structure was investigated by x-ray topography and diffractometry at room temperature. For the topographic investigations we employed a backreflection method (Berg–Barrett–Newkirk method) using CuK_α radiation and the Lang transmission method using MoK_α radiation in a series of symmetric and asymmetric reflections.[6] The diffraction curves were obtained in two- and three-crystal recording regimes[7,8] (θ and $\theta/2\theta$ scanning respectively) using the 444 CuK_α radiation peak for $Cd_2Nb_2O_7$. Germanium single crystals (400 peak) were used as the monochromator and the analyzer.

The samples were $(111)_{cub}$-oriented plates having linear dimensions between 2 and 10 mm and thicknesses between 0.2 and 2 mm. The measurements were made using plates having natural surfaces without any additional treatment and also using thin plane-parallel plates whose surfaces had been treated mechanically and then polished chemically using a mixture of orthophosphoric and acetic acids (examples of topograms are shown in Figs. 1 and 2).

The half-widths of the reflection curves ω_θ and $\omega_{\theta/2\theta}$ for the undoped and doped crystals are given in Tables I and II. Also given are the lattice parameters d calculated from the angles $2\theta_B$ obtained by a three-crystal method.[8] The relative error in determining the lattice parameter was $\Delta d/d \sim 1 \times 10^{-5}$ as a result of the instrumental accuracy of the angular measurements ($\pm 1''$).

The large half-widths of the curves ω_θ for all the crystals indicate that their structure is not perfect. In accordance with the values of ω_θ, the crystals studied can be arbitrarily divided into three groups of structural perfection. The colorless and lightly colored crystals (crystals 5–9 in Table I) have the most structural defects (high values of ω_θ). The highly colored crystals without dopants (Nos. 1–4 in Table I) and also those having low dopant concentrations ($x<0.1$, Table II) have the most perfect structures, regardless of the dopant species. This group of crystals typically has the lowest values of ω_θ (for example, crystal No. 1 in Table I and Zn-doped crystals in Table II). As the dopant concentration increases ($x \geqslant 0.1$), the crystal structure exhibits more defects, as is evidenced by the high values of ω_θ. The structural perfection is impaired most severely in Cu- and Fe-doped crystals (Table II).

The average lattice parameter $d \sim (10.3728 \pm 0.0014)$ Å of these crystals corresponds to that typical of pyrochlore-structure compounds.[1,3] The spread of d values is random and is unrelated to the doping or the structural perfection of

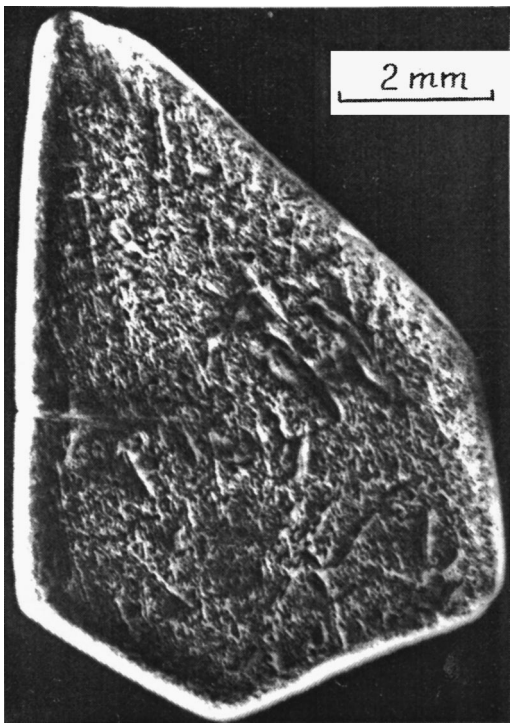

FIG. 1. X-ray topogram of an undoped crystal (7) with an image of the cellular dislocation structure obtained by the Lang method using MoK_α radiation.

the crystals. For instance, in Table I for crystal No. 1 having the smallest half-width ω_θ and crystal No. 9 having the largest ω_θ the lattice parameters are almost the same, whereas for Nos. 5 and 7 having comparable degrees of structural defects the lattice parameters differ substantially. The same is observed for doped crystals in Table II (for example, Zn- and Fe-doped crystals with $x=0.1$ or Ni-doped crystals with $x=0.1$ and Fe-doped crystals with $x=0.2$).

Thus, for these crystals the half-widths of the diffraction curves ω_θ and $\omega_{\theta/2\theta}$ are highly sensitive to lattice distortions for which the lattice parameter remains almost constant. Note that changes in the half-width of the $\omega_{\theta/2\theta}$ curves are

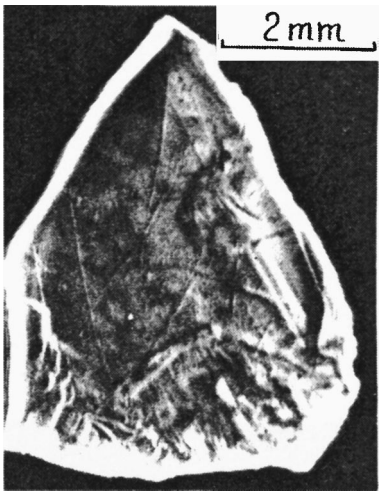

FIG. 2. X-ray topogram of a doped crystal obtained by the Lang method: M = Gd, $x=0.1$.

TABLE I. Characteristics of undoped $Cd_2Nb_2O_7$ crystals.

No.	Crystal	ω_θ, s	$\omega_{\theta/2\theta}$, s	d, Å
1	Light brown	23	10	10.3722
2	Orange	30	20	10.3728
3	Orange	48	16	10.3721
4	Golden brown	49	30	10.3734
5	Colorless	70	35	10.3728
6	Colorless	70	35	10.3719
7	Pale yellow	70	35	10.3714
8	Whitish	120	70	10.3714
9	Pale yellow	180	43	10.3720

caused by the displacement of atoms in lattice sites accompanying compressive-tensile deformation and the presence of dislocations which influence the fluctuations of the parameter d, whereas the change in the half-width of the ω_θ curves also depends on the contribution of orientational damage (deformation bending, microblock formation, fine-mesh dislocation structure, and so on). The increasing difference between the values of ω_θ and $\omega_{\theta/2\theta}$ in crystals having a more defective pyrochlore structure (Tables I and II) indicates that orientational damage is not a dominant factor. This particularly applies to colorless and lightly colored undoped crystals and doped crystals with dopant concentrations $x \geqslant 0.1$.

The topograms obtained by backreflection using CuK_α radiation showed that these crystals contain no blocks or small-angle boundaries. However, the image of the dislocation structure on these topograms is blurred or completely absent because of the strong absorption of x-rays (the criterion for identifiability of dislocations is $g>0.2$, this being the ratio of the absorption depth to the extinction length[9]). Thus, we obtained topograms of thin samples by the Lang transmission method using MoK_α radiation. We observed that the dislocation structure of the undoped crystals has a uniform cellular structure with a linear cell size between 10 and 50 μm (Fig. 1). The dislocation density varies between $10^4\,cm^{-2}$ for highly colored crystals and $5\times10^5\,cm^{-2}$ for colorless and lightly colored crystals. For barely doped crystals ($x<0.1$) the dislocation structure also has a uniform cellular structure although the dislocation density is lower than that in undoped crystals, which is consistent with the higher structural perfection of the barely doped crystals. This is confirmed by the similar half-widths of the reflection curves for this group of crystals (Tables I and II).

For crystals with higher dopant concentrations ($x \geqslant 0.1$) the image of the defect structure becomes less clearly defined on the topograms (Fig. 2). This factor combined with the data given in Table II (an increase in the half-width of the ω_θ and $\omega_{\theta/2\theta}$ curves) suggests that the crystal structure contains more defects when $x \geqslant 0.1$. In particular, structural damage may be caused by point defects formed as a result of some impurities entering interstitial sites. The tendency to form these defects in $Cd_2Nb_2O_7$ crystals with increasing dopant concentration is inherent in the pyrochlore structure.[10,11]

A common property of the M^{2+} dopants introduced is that their ionic radii are considerably smaller than the ionic radius of Cd^{2+} (0.99 Å), which is the minimum for the formation of a pyrochlore structure.[10] In addition, for dopants

TABLE II. Characteristics of doped crystals.

	Dopant concentration, x											
	0.02			0.05			0.1			0.2		
Dopant M	ω_θ, s	$\omega_{\theta/2\theta}$, s	d, Å	ω_θ, s	$\omega_{\theta/2\theta}$, s	d, Å	ω_θ, s	$\omega_{\theta/2\theta}$, s	d, Å	ω_θ, s	$\omega_{\theta/2\theta}$, s	d, Å
Zn^{2+}	50	40	10.3717				60	40	10.3726	120	60	10.3723
(0.83)*	22	10	10.3719				22	20	10.3722	70	35	10.3721
Ni^{2+}				30	23	10.3722	60	25	10.3717			
(0.74)*	40	25	10.3720	35	18	10.3716	90	35	10.3716			
Fe^{2+}				20	18	10.3715	120	50	10.3723			
(0.80)[a]*	35	21	10.3720	42	23	10.3725	28	20	10.3719	60	29	10.3715
Cu^{2+}	45	25	10.3716				180	60	10.3716	95	20	10.3726
(0.80)[b]*	25	18	10.3718				200	60	10.3714	210	60	10.3742
Gd^{3+}												
(0.94)*				50	28	10.3715						

[a]The ionic radius of Fe^{3+} is 0.67 Å.
[b]The ionic radius of Cu^{1+} is 0.98 Å.

with variable valence (such as Cu and Fe) not only the ionic radius but also the charge may differ from those of the Cd^{2+} ion. In accordance with the condition for stability of a pyrochlore structure, which imposes constraints on the degree of deformation of the $(CdO_8)^{n-}$ and $(NbO_6)^{n-}$ structural sublattices,[11] these factors imply that the Cd^{2+} ion in the $(CdO_8)^{n-}$ sublattice can either be replaced by an M^{2+} dopant ion or by both an M^{2+} ion and a B^{3+} (0.20 Å) boron ion.[5] However, only a small number of M^{2+} dopants can enter the $(CdO_8)^{n-}$ sublattice as substitutional impurities and the remaining ones enter interstitial sites, impairing the structural perfection. Since for $x<0.1$ doped $Cd_{2-x}M_xNb_2O_7$ crystals have the smallest half-widths of the diffraction curves (Table II), the dopants are predominantly substitutional. In this case, the change in the color of the doped crystals is related to the specific substitutional impurity. The dependence of the color of doped crystals on the type of dopant suggests that the color of undoped crystals is also related to the presence of substitutional impurities, although in this case the impurity is random (for example, B^{3+}, Fe^{2+}, V^{2+}, and so on[5]). The presence of random impurities is characteristic of all undoped crystals, but in colorless crystals the impurities predominantly enter interstitial sites, causing appreciable structural damage (Nos. 5–9 in Table II).

Similar structural damage is observed in doped crystals with dopant concentrations $x \geqslant 0.1$, where the interstitial position of the dopant becomes the dominant factor. Damage to the crystal structure may also be caused by vacancy defects in place of the Cd^{2+} ion or substitutional impurities having larger radii than the Cd^{2+} ion (such as Pb^{2+}, $(Cd^{2+}+B^{3+})$, and so on[5,10]). To conclude, we note that although the nature of the defects and structural damage in $Cd_2Nb_2O_7$ crystals requires further study, the fact that their structural characteristics are highly sensitive to lattice distortions indicates that x-ray diffraction techniques are potentially useful to study the structural quality not only of pyrochlores but of ferroelectrics and relaxors in general.

This work was supported financially by the Russian Fund for Fundamental Research (Projects Nos. 97-02-18099 and 98-02-18309).

[1] *Landolt-Börnstein Numerical Data and Functional Relationships in Science and Technology, New Series, Group III, Crystal and Solid State Physics*, Vol. 16a (Springer-Verlag, Berlin, 1981).
[2] N. N. Kolpakova, M. Wiesner, G. Kugel, and P. Bourson, Ferroelectrics **201**(1), 107 (1997).
[3] K. Lukaszewicz, A. Pietraszko, A. Stepien-Damm, and N. N. Kolpakova, Mater. Res. Bull. **29**, 987 (1994).
[4] F. Chu, I. M. Reaney, and N. Setter, J. Am. Ceram. Soc. **78**, 1947 (1995).
[5] N. N. Kolpakova, M. Wiesner, A. O. Lebedev, P. P. Syrnikov, and V. A. Khramtsov, Pis'ma Zh. Tekh. Fiz. **24**(17), 36 (1998) [Tech. Phys. Lett. **24**, 679 (1998)].
[6] A. R. Lang, *Diffraction and Microscopic Methods in Materials Science*, Metallurgiya, Moscow (1984), 364 pp.
[7] V. A. Bushuev, R. N. Kyutt, and Yu. P. Khapachev, *Physical Principles of x-ray Diffractometric Determination of the Real Structural Parameters of Multilayer Epitaxial Films* [in Russian], Kabardino-Balkar State University Press, Nal'chik (1996), 178 pp.
[8] P. Fewster, J. Appl. Crystallogr. **15**, 275 (1982).
[9] I. L. Shulpina and T. S. Argunova, J. Phys. D **28**, A47 (1995).
[10] F. Jona, G. Shirane, and R. Pepinsky, Phys. Rev. **98**, 903 (1955).
[11] R. A. McCauley, J. Appl. Phys. **51**, 290 (1980).

Translated by R. M. Durham

Hydrodynamic characteristics of pulsed processes in a compressible medium with a multiple (pulsating) energy deposition law

V. S. Krutikov and A. G. Lopatnev

Institute of Pulse Research and Engineering, National Academy of Sciences of Ukraine, Nikolaev Ukrainian State Maritime Technical University, Nikolaev

(Submitted February 17, 1999)
Pis'ma Zh. Tekh. Fiz. **25**, 34–41 (July 26, 1999)

The inverse problem of reconstructing the pressure at the moving boundary of a cylindrical plasma piston from the pulsating pressure at a point in the wave zone is solved for the first time. The law of motion of the plasma piston was unknown and needed to be determined. Kinematic and dynamic parameters of the expanding piston were obtained to determine the law of power deposition into the channel. As a result of an exact analytic solution of the problem, it is shown that if the pressure function at the channel wall is a series of pulses of increasing amplitude, the pressure function at a fixed point in the wave zone is also a series of increasing pulses. The pulsation period of the pressure curve at the channel wall is equal to the pulsation period of the power deposition curve and the pulsation period of the pressure curve at a fixed point in the wave zone. © *1999 American Institute of Physics.* [S1063-7850(99)02207-7]

In electrical discharges, laser pulses, and so forth in a compressive medium, the power deposition law usually takes the form of an isolated pulse, a problem which has been fairly thoroughly studied.[1,2] The possible applications of pulsed processes increase substantially when two, three , and in general, multiple, power deposition events whose pulsations obey a specific law are used in an expanding plasma channel. It was shown in Refs. 3–5, for example, that by parametrically varying the characteristics of the discharge circuit, the power deposition law can be varied fairly extensively to produce complex pressure pulses. Vovchenko *et al.*[6] considered an external hydrodynamic problem with a two-pulse power deposition law in a plasma channel. In this case, because of mathematical difficulties the authors used an approximation rather than an accurate solution of the cylindrically symmetric wave equation and the functions being studied were determined by superposition, calculated from the linear increase in the radius and the small-amplitude pulsations of the channel radius. As a result of an approximate analytic solution of the problem, the authors concluded that the pressure function at the channel wall is a series of pulses of decreasing amplitude and the pressure function for a fixed point in the wave field is a series of increasing pulses.[6] It is interesting to consider this important problem without making the above assumptions, in an exact formulation. Exact analytic solutions of the wave equation in regions with moving boundaries and an analysis of these solutions can yield more reliable conclusions.

Cylindrical symmetry is a particularly complicated case, and so far no exact analytic solution of the wave equation has been obtained in regions with moving boundaries.

We shall examine the problem

$$\varphi_{tt}-a^2\varphi_{rr}-a^2r^{-1}\varphi_r=0,\ \ r\geqslant R(t), \tag{1}$$

$$\varphi_t(r,0)=\varphi(r,0)=0,\ \ R(0)=r_0, \tag{2}$$

$$\rho\varphi_t|_{r=r_1}=P=f(r_1,t), \tag{3}$$

where t is the time, $R(t)$, r_0, r, and r_1 are the coordinates of the moving boundaries: the initial and instantaneous points in the wave zone, respectively, and a and ρ are constants. If the conditions are only defined at a fixed point in the wave zone (3), this determines a class of inverse problems. In order to solve inverse problems, we need to reconstruct the values of these functions at other points, including the moving boundaries, where the law of motion of the boundary is unknown and needs to be determined. We shall obtain a solution of the wave equation for the expansion of a cylinder in an unbounded compressible medium using the method of inverse problems and allowing for interaction of the nonlinear arguments.[7–9]

Applying a one-sided Laplace transformation to Eq. (1), allowing for zero initial conditions, we obtain an operator equation whose solution for the motion of a boundary in an unbounded medium with allowance for condition (3) gives the dependences of interest to us. The values of the functions under study are[7]

$$\overline{\varphi}=-\frac{\overline{f}(r,s)K_0(\mu r)}{s\rho K_0(\mu r_1)},\quad \overline{\varphi}_r=\frac{\overline{f}(r_1,s)K_1(\mu r)}{a\rho K_0(\mu r_1)},$$

$$s\overline{\varphi}=-\frac{\overline{f}(r,s)K_0(\mu r)}{\rho K_0(\mu r_1)}, \tag{4}$$

where $\mu=s/a$, s is the transformation parameter, and K_0 and K_1 are modified Bessel functions.

In Eq. (4) we can convert to the inverse transforms by a rational method in each specific case, depending on the form of the function f.

We shall express the transform $P(r_1,t)$ in a class of Bessel functions and we shall assume that for the inverse problem the following are known:

$$P(r_1,t)=f(r_1,t)=A\left(t-\frac{r_1^2}{a^2}\right)^{-1/2}, \quad t>r_1/a,$$

$$A=\text{const}. \tag{5}$$

Then, allowing for Eq. (4) and converting to the inverse transforms, we obtain for the values of the functions at any points and at the moving boundary

$$P(r,t)=A\left(t^2-\frac{r^2}{a^2}\right)^{-1/2}, \quad v(r,t)=\frac{A\,t}{r\rho}\left(t^2-\frac{r^2}{a^2}\right)^{-1/2},$$

$$t>r/a, \quad P(R(t),t)=A\left(t^2-\frac{R^2(t)}{a^2}\right)^{-1/2}, \tag{6}$$

$$v(R(t),t)=\frac{A\,t}{R(t)\rho}\left(t^2-\frac{R^2(t)}{a^2}\right)^{-1/2}=\frac{dR(t)}{dt}. \tag{7}$$

We shall determine the function $R(t)$ from the second relation in Eq. (7):

$$R^2(t)=\frac{2A}{\rho}\sqrt{t^2-\frac{R^2(t)}{a^2}}+\frac{2A^2}{\rho^2a^2}\ln\left|\sqrt{t^2-\frac{R^2(t)}{a^2}}-\frac{A}{\rho a^2}\right|. \tag{8}$$

The function $R(t)$ is calculated from Eq. (8) and similar relationships as in the case of spherical symmetry.[8,9] A good approximation is the formula for $a\to\infty$

$$R(t)=\left(\frac{2At}{\rho}\right)^{1/2}.$$

For the case $P(r_1,t)=f(r_1,t)$, i.e., an arbitrary function, suitable formulas are given in Ref. 7. These formulas are exact and substituting them into the wave equation converts its left-hand side to zero. A comparison was made with the results of a numerical solution using the characteristics of the complete system of equations of motion, continuity, and state in the Tait form.[7] The limits of validity of the wave equation and its accurate solutions in problems of pulsed hydrodynamics and acoustics were determined and found to be in the range $M=v/a\leqslant 0.2$ (Ref. 10), where v is the expansion velocity of the cavity. In this case, the shock wave separates immediately from the expanding piston at the velocity $a_0=\text{const}$.

For a pulsating law we have

$$P(r_1,t)=\sum_{m=0}^{n}\frac{A_m\sigma_0\left(t-\alpha_m-\dfrac{r_1-r_0}{a}\right)}{\sqrt{(t-\alpha_m)^2-\left(\dfrac{r_1-r_0}{a}\right)^2}}, \tag{9}$$

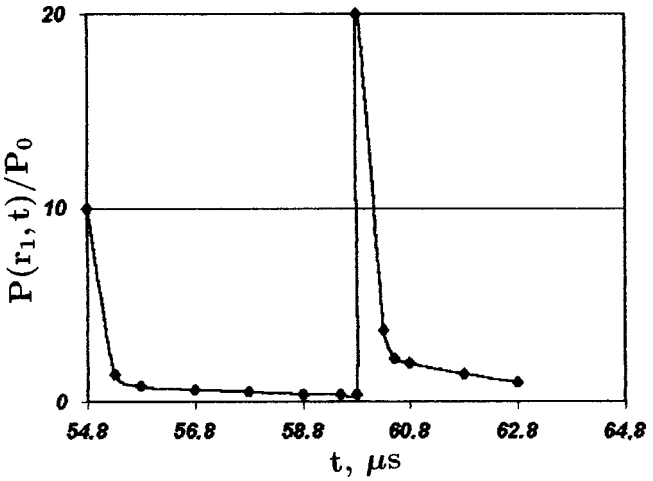

FIG. 1. Initial increasing series of pressure pulses for the reconstruction as a function of time at a fixed point in the wave zone.

$$P(R(t),t)=\sum_{m=0}^{n}\frac{A_m\sigma_0\left(t-\alpha_m-\dfrac{R(t)-r_0}{a}\right)}{\sqrt{(t-\alpha_m)^2-\left(\dfrac{R(t)-r_0}{a}\right)^2}}$$

$$-\frac{1}{2}\rho v^2(R(t),t). \tag{10}$$

The pressure at the moving boundary of the piston is determined taking into account the nonlinear term of the Cauchy–Lagrange integral:[10,11]

$$v(R(t),t)=\sum_{m=0}^{n}\frac{A_m(t-\alpha_m)\sigma_0\left(t-\dfrac{R(t)-r_0}{a}-\alpha_m\right)}{\rho(R(t)-r_0)\sqrt{(t-\alpha_m)^2-\left(\dfrac{R(t)-r_0}{a}\right)^2}}, \tag{11}$$

$$R(t)-r_0=\sqrt{\sum_{m=0}^{n}\frac{2A_m(t-\alpha_m)\sigma_0(t-\alpha_m)}{\rho}}, \tag{12}$$

where σ_0 is a zeroth-order unit step function.

Using the known kinematic and dynamic parameters (9)–(12) of a expanding cylindrical plasma piston, we can determine the power deposited in the channel using the energy balance equation.[1]

Figures 1–4 gives the results of calculations using formulas (9)–(12) for $A_0=10\times10^{-6}$ kgf·s/cm^2, $A_1=20\times10^{-6}$ kgf·s/cm^2, $\rho=102$ kgf·s/cm^4, $a=1460$ m/s, $r_0=0.013\times10^{-3}$ m, $r_1=0.08$ m, $\alpha_1=5\times10^{-6}$ s, and $\alpha_0=0$.

An analysis of formulas (9)–(12) shows that if the pressure function at point r_1 in the wave zone is a series of pulses of decreasing amplitude, the pressure function at the walls of the plasma channel will also be a series of pulses of decreasing amplitude. Conversely, an increasing series of pulses at the moving boundary will correspond to a series of increasing amplitude at the point in the wave zone, as shown in the figures. This behavior is consistent with the physics of the effect as described by the wave equation. Two different pressure discontinuities generated at the moving boundary

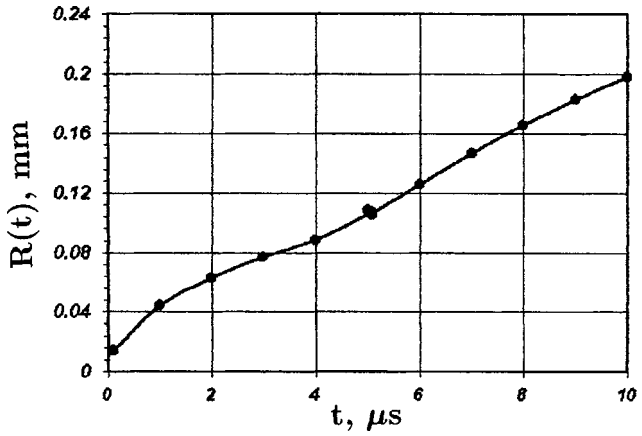

FIG. 2. Reconstruction of the radial variation of the moving boundary of the plasma piston as a function of time.

and propagating along the medium will have two properties: first, they will always be separated by the same distance, this being proportional to α_m ($a=\text{const}$ and no compression is predicted). Second, the amplitude ratio will always be preserved (the first discontinuity may be greater or smaller than the second), varying in the same way as $1/\sqrt{t^2-(r-r_0/a)^2}$, but with the delay α_m.

The distance between the discontinuities can vary if at least one of these propagates at a velocity exceeding the velocity of sound, $a=\text{const}$. In this case, however, the effects are described by different equations, such as the complete system (1) (Ref. 10). The amplitude of the discontinuity may also increase during propagation, for example, when a wave propagates through sections of a two-phase medium saturated with bubbles of specific sizes and concentrations, which should also be described by different equations.

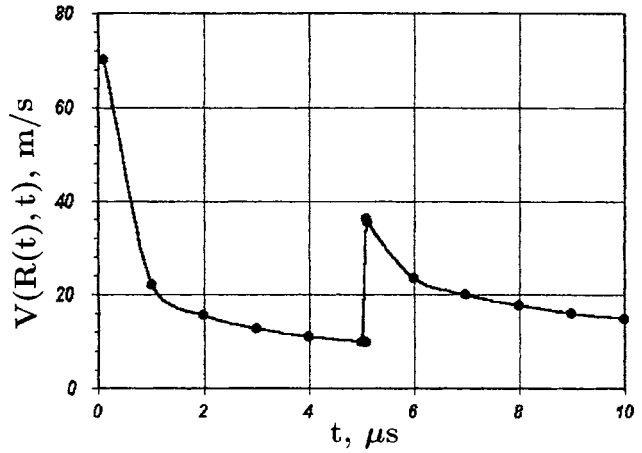

FIG. 3. Reconstruction of the velocity variation of the moving boundary as a function of time.

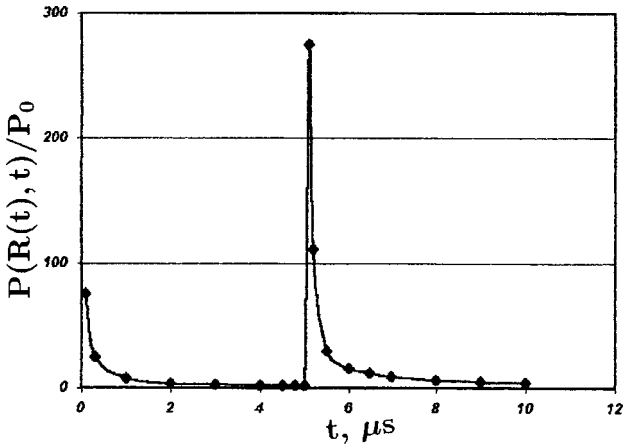

FIG. 4. Reconstruction of the pressure variation at the moving boundary of the plasma piston as a function of time using the given pulsating pressure at the point in the wave zone in Fig. 1.

An analysis of formulas (9)–(12) and the energy balance equation for moderately strong electrical discharges in water[11]

$$\frac{N(t)}{l}=S\frac{dP(R(t),t)}{dt}\frac{1}{\gamma-1}+P(R(t),t)\frac{dS}{dt}\frac{\gamma}{\gamma-1},$$

where $S=\pi R^2(t)$, γ is the effective adiabatic exponent of the plasma, l is the channel length, and $N(t)$ is the power deposited in the channel, shows that the pulsation period of the pressure curve at the channel wall is equal to the pulsation period of the power deposition curve and the pulsation period of the pressure curve at a fixed point in the wave zone.

In Fig. 3 the curve of the velocity of the moving piston boundary has a second discontinuity smaller than the first, whereas the pressure curve $P(R(t),t)$ in Fig. 4 has a second discontinuity greater than the first. This is consistent with the physics of the effect described by the wave equation. The second pressure discontinuity is induced from a considerably larger (almost an order of magnitude) channel radius, although it expands slightly more slowly.

[1] K. A. Naugol'nykh and N. A. Roĭ, *Electric Discharges in Water* [in Russian], Nauka, Moscow (1971), 151 pp.
[2] L. M. Lyamshev, Usp. Fiz. Nauk **151**, 479 (1987) [Sov. Phys. Usp. **30**, 252 (1987)].
[3] A. V. Ivanov, A. I. Vovchenko, and O. A. Bogachenko, Tekh. Élektrodinam. No. 6, 15 (1981).
[4] V. V. Ivanov, Élektron. Obrab. Mater. No. 3, 30 (1982).
[5] A. I. Vovchenko, Tekh. Élektrodinam. No. 1, 12 (1983).
[6] A. I. Vovchenko, V. G. Kovalev, and V. A. Pozdeev, Pis'ma Zh. Tekh. Fiz. **23**(9), 58 (1997) [Tech. Phys. Lett. **23**, 358 (1997)].
[7] V. S. Krutikov, Pis'ma Zh. Tekh. Fiz. **14**, 510 (1988) [Sov. Tech. Phys. Lett. **14**, 226 (1988)].
[8] V. S. Krutikov, Prikl. Mat. Mekh. **55**, 1058 (1991).
[9] V. S. Krutikov, Dokl. Akad. Nauk **333**, 512 (1993).
[10] V. S. Krutikov, Akust. Zh. **42**, 534 (1996) [Acoust. Phys. **42**, 471 (1996)].
[11] L. I. Slepyan, Dokl. Akad. Nauk SSSR **282**, 809 (1985) [Sov. Phys. Dokl. **30**, 448 (1985)].

Translated by R. M. Durham

Possible ionization of mercury atoms by elastic reflection in hyperthermal surface ionization experiments

N. M. Blashenkov and G. Ya. Lavrent'ev

A. F. Ioffe Physicotechnical Institute, Russian Academy of Sciences, St. Petersburg
(Submitted March 3, 1999)
Pis'ma Zh. Tekh. Fiz. **25**, 42–45 (July 26, 1999)

An elastic collision model baed on data given by Danon *et al.* [Phys. Rev. Lett. **65**, 2038 (1990)] was used to calculate the ionization potential of mercury atoms (V') at the critical charge transfer distance as a function of the kinetic energy of the atoms (E). The linear dependence $V'(E)$ obtained supports the model of surface ionization of mercury atoms by elastic reflection from a surface. © *1999 American Institute of Physics.* [S1063-7850(99)02307-1]

In our view, no generally accepted theoretical interpretation has been put forward so far for experimental data on the surface ionization of hyperthermal (4–8 eV) mercury atoms.[1]

In the present study, a model of elastic reflection of atoms from a surface is used to estimate the changes in the ionization potential of mercury atoms (V') at the critical charge transfer distance (x_c) as a function of the energy (E) of the incident atoms using data from Ref. 1. The behavior of this dependence may serve as one criterion for selecting the ionization model for hyperthermal atoms.

The surface ionization of particles having a zero accommodation coefficient was studied by Ionov.[2] In elastic interaction the temperature of the Maxwellian energy distribution of reflected neutral particles (T_e), which differs from the surface temperature (T), remains constant. Those particles which have lost their electron to the absorbent as a result of elastic interaction with the surface as they pass through the region x_c and are reflected as ions, should perform the work $\lambda_+ > \lambda_0$ and cannot all leave the surface (here λ_+ and λ_0 are the desorption work of the positive and neutral particles). If the time of particle motion in the region x_c exceeds the time taken to establish charge equilibrium between the particles and the surface, the degree of ionization (α_e) in an elastically reflected particle flux in the plane x_c is given by[2]

$$\alpha_e|_{x_c} = A \exp \frac{e(\varphi - V')}{kT},$$

where A is the ratio of the particle partition functions in the ion and neutral states and φ is the work function of the surface. All particles reflected in the neutral form surmount the barrier λ_0, whereas an additional potential barrier $\lambda_+ - \lambda_0$ will exist for the ions, which they must overcome by means of the initial kinetic energy. Thus, the degree of ionization α_e in a particle flux reflected elastically from the surface of an adsorbent having the ionization potential V is expressed by the formula proposed by Ionov:[2]

$$\alpha_e = A \exp \frac{e(\varphi - V')}{kT} \exp \frac{\lambda_0 - \lambda_+}{kT_e}$$

$$= A \exp \frac{e(\varphi - V)}{kT} \exp \left[(\lambda_0 - \lambda_+) \left(\frac{1}{kT_e} - \frac{1}{kT} \right) \right], \qquad (1)$$

from which it follows that for $\lambda_+ > \lambda_0$ the value of α_e increases with increasing T_e. Note that in the elastic collision model, the ratio A of the partition functions remains constant as T_e increases, because if excited states were populated with increasing T_e the collisions would be inelastic.

We transform Eq. (1), expressing λ_+ and λ_0 in terms of V' and V from the relation obtained from the closed thermodynamic cycle:[3] $\lambda_0 - \lambda_+ = e(V - V')$. Using the identity $V - V' = (V - \varphi) - (V' - \varphi)$ and performing simple transformations (1), we obtain

$$\alpha_e = A \exp \left\{ \frac{e(\varphi - V)}{kT_e} \left[1 - \frac{\varphi - V'}{\varphi - V} \left(\frac{T_e}{T} - 1 \right) \right] \right\}.$$

The ion current (j) accompanying elastic reflection of mercury atoms from a surface (case of difficult ionization) is given by

$$j \simeq eg\alpha_e,$$

where g is the particle flux reaching the surface.

It can be seen from these formulas that if we know the ion current, the energy of the mercury atoms $E = kT_e$, the work function of the surface, and the ionization potential of the mercury atoms, we can calculate the values of V' for various kT_e.

Since the ion current was given in relative units in Ref. 1, we omitted the constants g and A in the calculations of V' as in Ref. 1 and equated the value of α_e to the experimental values of the ion yield.[1] Figure 1 gives V' as a function of the kinetic energy E of the mercury atoms incident on the surface.

In our view, the linear dependence of V' on E supports the mechanism for ionization by elastic reflection of mercury atoms from an adsorbent. We postulate that the S shell of the mercury atom is deformed in proportion to the kinetic energy of the atoms. Deformation of the S shell is accompanied by an increase in the electron charge density over distances

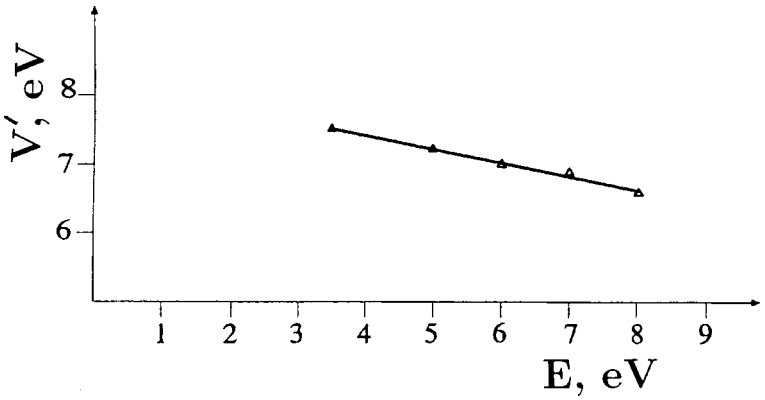

FIG. 1. Ionization potential of mercury atoms (V') at the critical charge transfer distance as a function of the kinetic energy of the atoms (E).

greater than the mean radius of the S-shell. The value of V' decreases in inverse proportion to this distance.[4] In the limits of the calculated variations of V', all the calculated values vary linearly with E. Moreover, at the maximum kinetic energy of the atoms 8.2 eV the difference $e(V-V')$ is 3.84 eV, which is lower than the first excited level of the mercury atom (4.67 eV), i.e., the ionization process takes place without the involvement of excited states, which is confirmed by the dependence of $\ln j$ on E, typical of barely ionizable particles $e(V-\varphi)\geqslant kT$ (Refs. 2 and 5).

It is interesting to note that the expressions for α_e are the same as the formula for the degree of nonequilibrium surface ionization α_n of vibrationally excited molecules and radicals.[5] The identity of the formulas can be attributed to the identity of the assumptions used in order to independently derive the expressions for α_e (Ref. 2) and α_n (Ref. 6):

1. The probability of particle charge transfer is determined by the electron distribution over the energy levels of the emitter, i.e., by the surface temperature T.

2. The probability of particle escape is determined by their quasi-Maxwellian initial energy distribution, which is characterized by the temperature T_n or T_e.

Thus, the degree of nonequilibrium surface ionization is determined by the values of T, T_n, or T_e and does not depend on the mechanism for the establishment of nonequilibrium conditions in the adsorbent–adsorbate system. The value of T_e is provided by the kinetic energy of the atoms reaching the surface,[1] and T_n is either provided by the energy of heterogeneous chemical reactions[6] or by resonant absorption of infrared radiation by adsorbed molecules.[7]

In conclusion, the authors would like to thank V. I. Paleev and N. D. Potekhina for useful discussions.

[1] A. Danon, A. Vardi, and A. Amirav, Phys. Rev. Lett. **65**, 2038 (1990).
[2] É. Ya. Zandberg and N. I. Ionov, *Surface Ionization* [in Russian], Nauka, Moscow (1969), 432 pp.
[3] L. N. Dobretsov and M. V. Gomoyunova, *Emission Electronics* [Israel Program for Scientific Translations, Jerusalem (1971); Nauka, Moscow (1966), 564 pp.].
[4] W. Heitler, *Elementary Wave Mechanics* [Clarendon Press, Oxford (1945); Moscow (1948), 136 pp.].
[5] N. M. Blashenkov and G. Ya. Lavrent'ev, Pis'ma Zh. Tekh. Fiz. **21**(24), 15 (1995) [Tech. Phys. Lett. **21**, 1000 (1995)].
[6] N. M. Blashenkov and G. Ya. Lavrent'ev, Pis'ma Zh. Tekh. Fiz. **14**, 1359 (1988) [Sov. Tech. Phys. Lett. **14**, 593 (1988)].
[7] N. M. Blashenkov and G. Ya. Lavrent'ev, Pis'ma Zh. Tekh. Fiz. **23**(23), 22 (1997) [Tech. Phys. Lett. **23**, 909 (1997)].

Translated by R. M. Durham

Reverse saturable absorption in aromatic polyimides sensitized with fullerenes and dyes

N. V. Kamanina and L. N. Kaporskiĭ

''S. I. Vavilov State Optical Institute'' All-Russia Scientific Center, St. Petersburg
(Submitted July 21, 1998; resubmitted March 2, 1999)
Pis'ma Zh. Tekh. Fiz. **25**, 46–51 (July 26, 1999)

An investigation is made of optical limitation in a photosensitive polyimide system sensitized with fullerenes and dye under conditions when reverse saturable absorption is observed. The initial level of the effect and the prospects for using these media as laser radiation power limiters in the range 50–1000 mJ/cm^2 are determined. © *1999 American Institute of Physics.* [S1063-7850(99)02407-6]

The optical, photoelectric, and electromagnetic properties of aromatic polyimides ascribed to the excitation of the π-electron systems of these polymers[1–3] continue to attract interest and are yielding a wide range of research options involving the use of organic polymers in laser physics, microelectronics, and other information transformation systems.[4,5]

At present, an important aspect of studying the properties of polymer systems involves studying the reverse saturable absorption observed when fullerenes are incorporated in the matrix. These investigations can be used not only to study and estimate the optical nonlinearity[6] but also to determine the prospects for using fullerene-containing media as laser radiation doubling and trebling elements[7] and also as optical limiters for laser radiation.[7,8]

Kost *et al.*[9] studied the mechanisms for optical limiting in polymethylmethacrylate with added C_{60} molecules, determined the threshold of the effect, and made a comparison with the data for a fullerene-containing toluene solution. Hosoda *et al.*[10] investigated the effectiveness of adding fullerenes to polysilanes, while Wang *et al.*[11] studied the effectiveness of adding them to polyvinylcarbazole. The first investigations of the change in the optical absorption spectrum and optical limiting of $\lambda = 532$ nm laser radiation for a polyimide–fullerene system were reported by Kamanina *et al.*[12]

The aim of the present investigation is to make a comparative study of reverse saturable absorption in polyimide–fullerene and polyimide–fullerene–dye structures.

The aromatic polyimides used as the matrix in the present study had the general formula described in Ref. 13. The solvent was 1,1,2,2-tetrachloroethane,[3] which can effectively dissolve fullerenes (the solubility[14] of C_{60} in this solvent is ~ 5.3 mg/ml). A 6.5% composition of polyimides in tetrachloroethane to which we added a 0.15–2 wt.% fullerene mixture was deposited by centrifugation on glass substrates on which conducting layers had been predeposited. The fullerenes were added in the form of a fullerene extract containing 87% C_{60} and 13% C_{70}. The thickness of the samples was $\sim 1\ \mu$m. For comparison we prepared a polyimide sample to which we added 0.5% fullerene and 0.15% dye (malachite green).

The optical limitation of laser radiation by a fullerene-containing medium was investigated using an experimental apparatus whose single-pass system is similar to that described in Ref. 15. The radiation source was a pulsed neodymium yttrium aluminum garnet laser. An LiF crystal was used for passive modulation of the modes, and the radiation was converted to the second harmonic using a CDA crystal. The wavelength of the output radiation was 532 nm. We recorded the radiation incident on the sample and that transmitted by it. The radiation energy was varied using calibrated light filters. The input and output signals were recorded directly using laser radiation energy meters.

The main experimental results are plotted in Fig. 1 which gives the output radiation energy from the samples (E_{out}) as a function of the input energy (E_{in}). It can be seen that reverse saturable absorption is observed for polyimide structures containing 0.5% (curve *2*) and 2% fullerene (curve *3*), and also for the sample containing 0.5% fullerene and 0.15% malachite green (curve *4*). Curve *1* gives the data for the polyimide matrix without any sensitizers.

It can be seen that the nonlinear transmission process begins at E_{in} in the range 5–25 mJ for various samples. If the diameter of the second harmonic radiation spot is ~ 3 mm, this corresponds to an optical limitation level of order 0.07–0.35 J/cm^2. The addition of a dye as well as the fullerene attenuates the laser radiation ~ 15 times at the maximum illumination level of 200 mJ. It is worth noting that the optical limiting effect depends on the impurity concentration. This process was analyzed in greater detail for polyimide systems in Ref. 12 and will not be stressed in the present study. We merely note that the simultaneous addition of fullerenes and dye shifts the initial section of the nonlinear process to the right, toward higher levels of illumination, although it results in a substantially higher attenuation factor.

The physical mechanism responsible for the reverse saturable absorption effect and hence the principle of an optical limiter using fullerene-containing media, is associated with the fact that when a $\lambda = 532$ nm photon is absorbed by a C_{60} or C_{70} molecule, a triplet-state molecule forms whose

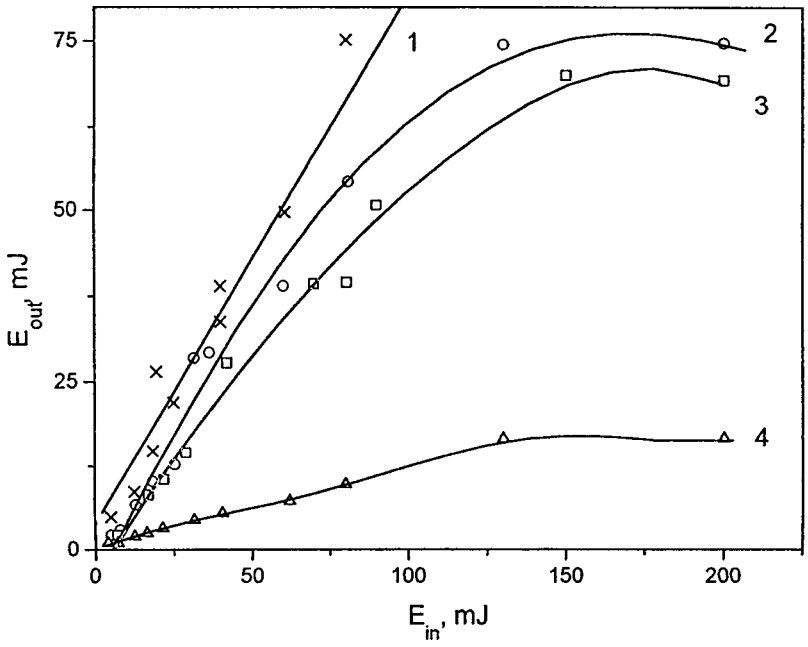

FIG. 1. Output energy from samples as a function of input radiation energy: *1* — polyimide matrix, *2* — polyimide–fullerene structure (0.5 wt.% fullerene extract), *3* — polyimide–fullerene structure (2 wt.% fullerene extract), and *4* — polyimide–fullerene–dye structure (0.5 wt.% fullerene extract and 0.15 wt.% dye.)

cross section for the absorption of a particular photon is several times the absorption cross section for the unexcited molecule.[8] The absorption should increase as the intensity of the incident light increases because of the increased population of excited states.[7,8] Note that the figure shows an increase in the absorption of fullerene-containing structures for all samples. Saturation then occurs and the transmission of light by the medium is limited. The kinetics of the filling and decay of the levels involved in the optical limiting of the radiation is satisfactorily described by a six-level scheme and was analyzed in detail in Refs. 6 and 7.

In our study the behavior of curve *4* (see Fig. 1) differs from that of curves *2* and *3* because the addition of the dye may have the result that the singlet transition scheme typical of polyimide with a wide range of dyes (such as malachite green, oxazine-1, and so on) has some influence.[3] The transition times and relaxation times of the energy levels responsible for the singlet and triplet mechanisms differ, but it is impossible to estimate which of these mechanisms predominates in our study because this requires the preparation of samples having more distinct ranges of concentrations and a wider range of illumination intensities. This will form the subject for further research. At this point we stress than the simultaneous addition of a dye and fullerene substantially increases the number of absorbing centers (increases the absorption) and subsequent saturation which causes stronger attenuation of the laser radiation, as is clearly shown by curve *4* (see Fig. 1).

The results of these investigations show that the use of fullerene-containing polyimides and also similar systems containing dyes as laser radiation power limiters in the range $50-1000\,\mathrm{mJ/cm^2}$ holds great promise.

The authors are grateful to V. I. Berendyaev for supplying the dry polyimide and also to M. A. Khodorkovskiĭ for supplying the fullerenes.

This work was partially supported under the Subprogram ''Optoelectronic and Laser Technologies'' (one line of research in the ''National Technological Base'' Presidential Program).

[1] M. Ree, T. L. Nunes, and K.-J. R. Chen, J. Polym. Sci. **33**, 453 (1995).
[2] V. S. Mylnikov, Adv. Polym. Sci. **115**, 3 (1994).
[3] B. M. Rumyantsev, V. I. Berendyaev, N. A. Vasilenko, S. V. Malenko, and B. V. Kotov, Vysokomol. Soedin. **39**, 720 (1997).
[4] N. V. Kamanina and N. A. Vasilenko, Opt. Quantum Electron. **29**, 1 (1997).
[5] Yu. A. Cherkasov and E. L. Aleksandrova, Zh. Nauchn. Prikl. Fotogr. No. 2, 87 (1998).
[6] S. Couris, E. Koudoumas, A. A. Ruth, and S. Leach, J. Phys. B: At. Mol. Opt. Phys. **28**, 4537 (1995).
[7] V. P. Belousov, I. M. Belousova, V. P. Budtov, V. V. Danilov, O. B. Danilov, A. G. Kalintsev, and A. A. Mak, Opt. Zh. **64**(12), 3 (1997) [J. Opt. Technol. **64**, 1081 (1997)].
[8] A. V. Eletskiĭ and B. M. Smirnov, Usp. Fiz. Nauk **165**, 977 (1995).
[9] A. Kost, L. Tutt, M. B. Klein, T. K. Dougherty, and W. E. Elias, Opt. Lett. **18**, 334 (1993).
[10] K. Hosoda, K. Tada, M. Ishikawa, and K. Yoshino, Jpn. J. Appl. Phys. **36**, L372 (1997).
[11] Y. Wang, N. Herron, and J. Casper, Mater. Sci. Eng., B **19**, 61 (1993).
[12] N. V. Kamanina, L. N. Kaporskiĭ, and B. V. Kotov, Opt. Zh. **65**(3), 85 (1998) [J. Opt. Technol. **65**, 250 (1998)].
[13] P. I. Dubenskov, T. S. Zhuravleva, A. V. Vannikov, N. A. Vasilenko, E. V. Lamskaya, and V. I. Berendyaev, Vysokomol. Soed. A No. 6, 1211 (1988).
[14] M. T. Beck and G. Mandi, Fullerene Sci. Technol. **5**(2), 291 (1997).
[15] V. P. Belousov, I. M. Belousova, V. G. Bespalov, V. P. Budtov, V. M. Volynkin, V. A. Grigor'ev, O. B. Danilov, A. P. Zhevlakov, A. G. Kalintsev, A. N. Ponomarev, S. A. Tul'skiĭ, and E. Yu. Yutanova, Opt. Zh. **64**(9), 82 (1997) [J. Opt. Technol. **64**, 870 (1997)].

Translated by R. M. Durham

Induction self-acceleration of a high-current electron beam

A. E. Dubinov

Russian Federal Nuclear Center — Research Institute of Experimental Physics, Sarov (Arzamas-16)
(Submitted July 21, 1998)
Pis'ma Zh. Tekh. Fiz. **25**, 52–56 (July 26, 1999)

Computer modeling using the particle-in-cell method confirmed that self-acceleration by induction of a high-current relativistic electron beam predicted by G. A. Askar'yan [At. Énerg. **6**, 658 (1959)] may occur when this beam passes through a thick diaphragm containing an aperture. © *1999 American Institute of Physics.* [S1063-7850(99)02507-0]

Some forty years ago, Askar'yan put forward the idea that a high-current relativistic electron beam may undergo self-acceleration by induction when most of the beam is removed from motion or stopped.[1] One method of achieving this self-acceleration, as proposed by Askar'yan,[2] may involve dumping the current at a thick diaphragm with a small aperture where most of it is absorbed.

As far as the author is aware, the possibility of implementing this method of acceleration has not been verified in practice, despite the simplicity of this effect and its significant value. One exception is an experimental study[3] in which a virtual cathode played the role of a diaphragm with an annular aperture. In this study,[3] the authors observed higher-energy electrons compared with the applied voltage in the drift space behind the virtual cathode, and they attributed this additional acceleration to the effect predicted by Askar'yan.[1,2]

However, the appearance of accelerated electrons in the drift space beyond the virtual cathode may have a different explanation: the virtual cathode is a source of a strong Coulomb field which repels the drift electrons, which are also in the accelerating phase of the high-power microwave radiation generated by the oscillations of the virtual cathode.[4] Thus, there is no justification for asserting that the ideas put forward in Refs. 1 and 2 are confirmed in Ref. 3.

In view of this, the aim of the present study is to check that an self-acceleration by induction may occur when an electron beam is dumped onto a thick diaphragm with a small aperture, as was proposed by Askar'yan.[2]

For this purpose, the dynamics of the dumping of a high-current relativistic electron beam onto a thick diaphragm with an aperture was modeled by computer. The modeling was performed using the fully self-consistent KARAT 2.5-dimensional electromagnetic PIC code developed by Tarakanov.[5]

Figure 1 shows the geometry of the modeling region with the required dimensions and proportions. The structure being modeled was a high-current vacuum electron diode with an annular cathode and a thick diaphragm incorporating a thin annular aperture, beyond which the drift zone was located. A strong longitudinal magnetic field of 50 kG was applied to the entire region. It was assumed that a high-voltage rectangular pulse with an open-circuit amplitude of 400 kV was applied to the diode. The variable parameters were the aperture width (1–5 mm), the thickness of the electron beam tube (6–10 mm), and the electron beam current

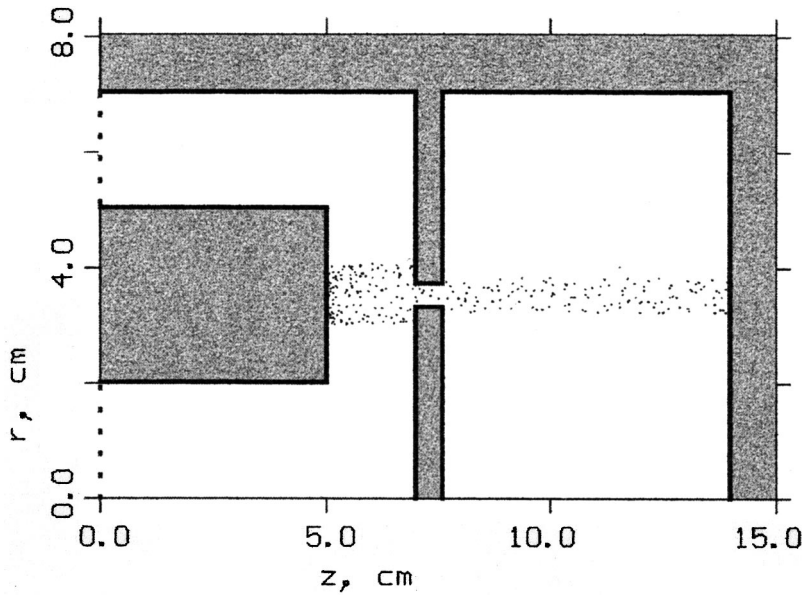

FIG. 1. Geometry of modeled region in (r,z) coordinates (the upper half is shown).

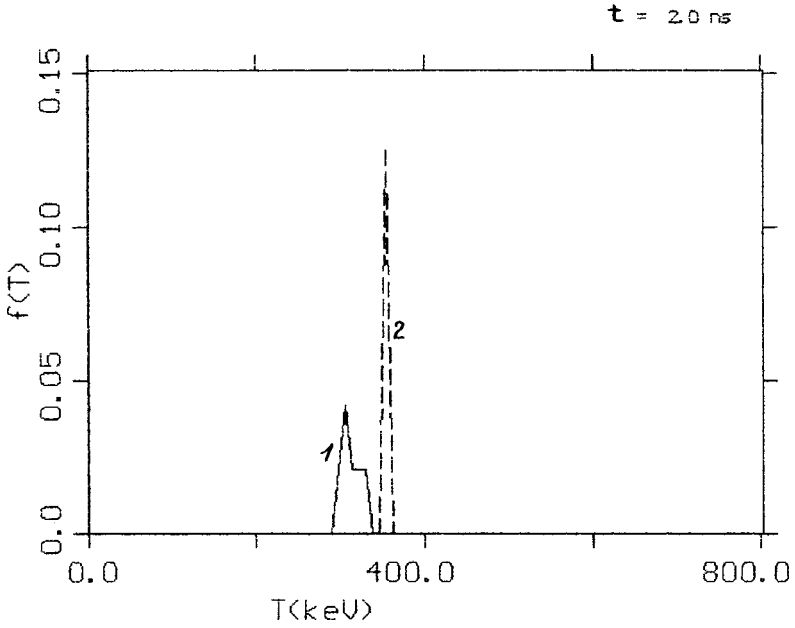

FIG. 2. Energy distributions of beam electrons: *1* — before diaphragm, *2* — after diaphragm.

(4–8 kA). The electron energy distribution function on either side of the diaphragm at a distance of 1 mm from its planes was monitored in the calculations.

By way of example, we present the results of modeling for a 3 mm wide aperture, an electron beam tube 8 mm thick, and a beam current of 5 kA (Fig. 2).

Since the diode voltage in the electron current regime is slightly lower compared with the open-circuit regime, the energy of the electrons reaching the diaphragm is appreciably lower than 400 keV (approximately 303 keV). However, after propagating through the aperture, the electrons already possess a significantly higher energy $\sim$358 keV.

The increase in energy was more than 18%, although this is still considerably less than the estimates obtained from the formulas given in Ref. 2. The reason for this discrepancy may be that in our case the accelerated fraction of the electron current and the fraction of the current absorbed by the diaphragm are spatially separated along the radius, whereas the formulas from Ref. 2 refer to the case where both fractions coincide.

For the other values of the parameters, the increase in the electron energy was between 3% and 24%. Thus, the electron self-acceleration effect predicted in Refs. 1 and 2 does occur in this model scenario.

However, it is quite clear that using this effect to accelerate electrons to high energies presents problems. Nevertheless, we shall give two examples in which neglecting self-acceleration by induction may lead to mismatch in the exact tuning of various devices.

The first example concerns the correct sampling of beam particles in various types of energy analyzer. For instance, Minashkin *et al.*[6] proposed an electron spectrometer with a toroidal magnetostatic field in which a beam from a high-current diode is coupled into a toroidal solenoid using a small-aperture diaphragm, and this was then analyzed by Dubinov *et al.*[7] Thus, in order to avoid significant errors when reconstructing the energy spectrum in these systems it is fundamentally important to allow for the self-acceleration by induction.

The second example concerns the formation of thin electron beams in cyclotron-resonance masers. In Ref. 8, for example, Bratman and Samsonov describe an oscillator in which the beam is formed by cutting away part of a higher-current beam generated by an explosive-emission cathode. The self-acceleration effect must be taken into account to obtain more accurate matching between the electrons and the electrodynamic structure of the maser.

[1] G. A. Askar'yan, At. Énerg. **6**, 658 (1959).
[2] G. A. Askar'yan, Tr. Fiz. Inst. Akad. Nauk SSSR **66**, 66 (1973).
[3] A. N. Didenko, A. G. Zherlitsyn, Yu. P. Usov, and G. P. Fomenko, Pis'ma Zh. Tekh. Fiz. **4**, 381 (1978) [Sov. Tech. Phys. Lett. **4**, 154 (1978)].
[4] B. V. Alyokhin, A. E. Dubinov, V. D. Selemir *et al.*, IEEE Trans. Plasma Sci. **22**, 945 (1994).
[5] V. P. Tarakanov, *User's Manual for Code KARAT*, Berkley Research Associates, Springfield, VA (1992).
[6] N. V. Minashkin, V. D. Selemir, and N. V. Stepanov, Author's Certificate No. 1681658, 16.06.89, MKI: G 01 t 1/29, Byull. Izobret. No. 27, 1992.
[7] A. E. Dubinov, N. V. Minashkin, V. D. Selemir *et al.*, in *Proceedings of the Ninth IEEE International Pulsed Power Conference*, Albuquerque, NM, 1993, p. 708.
[8] V. L. Bratman and S. V. Samsonov, in *Fizika Mikrovoln, Vol. 1* (IPF RAS, 1996), p. 14.

Translated by R. M. Durham

Adsorption of sulfur on heated $(10\bar{1}0)$ Re

N. R. Gall', E. V. Rut'kov, and A. Ya. Tontegode

A. F. Ioffe Physicotechnical Institute, Russian Academy of Sciences, St. Petersburg
(Submitted April 29, 1999)
Pis'ma Zh. Tekh. Fiz. **25**, 57–64 (July 26, 1999)

High-resolution Auger electron spectroscopy is used to study the adsorption of sulfur on a $(10\bar{1}0)$ Re surface and to determine the regions of thermal stability of the resulting adsorption states. The formation of surface sulfide is observed and its stoichiometry, Re_2S, and the absolute sulfur concentration on the rhenium surface $N_S=(6.0\pm1)\times10^{14}$ atom/cm^2 are determined. It is shown that the surface sulfide is destroyed by thermal desorption of sulfur from the rhenium surface and the desorption activation energy is estimated as $E_d=(3.3\pm0.2)$ eV for a coverage close to the surface sulfide and $E_d=(4.9\pm0.2)$ eV in the limit $\theta\to0$. [S1063-7850(99)02607-5]

An understanding of the processes accompanying the interaction between sulfur and the surface of refractory metals is important in heterogeneous catalysis, metallurgy, and corrosion prevention. The adsorption of sulfur on the surface of transition[1–4] and platinum[5–7] metals has been fairly well studied, but only a few studies have dealt with group VII metals.[8] Moreover, conclusions on the nature of the high-temperature processes are based on measurements made at room temperature after cooling the sample. In addition, no quantitative estimates have been made of the sulfur concentration in the observed adsorption states.

1. EXPERIMENTAL METHOD

The investigations were carried out using a high-resolution, ultrahigh-vacuum ($P\sim10^{-10}$ Torr) Auger spectrometer, described by Gall *et al.*[9] The sample was a $1\times0.02\times40$ mm polycrystalline rhenium ribbon heated by an ac current. The ribbon was cleaned by alternately heating in ultrahigh vacuum at 2500 K and in an oxygen atmosphere ($P_{O_2}\sim10^{-6}$ Torr). After cleaning, the surface of the ribbon only exhibited the Auger peaks of rhenium. The cleaning process was accompanied by texturing of the ribbon and the $(10\bar{1}0)$ face emerged at the surface with the work function $e\varphi=5.15$ eV, which is typical for this face.[10] According to the x-ray diffraction data, the degree of orientation of the face relative to the surface was 99.9%. The ribbon temperature was measured using a micropyrometer, and outside the pyrometer range it was determined by linearly extrapolating the dependence of the temperature on the heating current.

A stream of hydrogen sulfide H_2S was supplied to deposit sulfur on the surface. We used the $E=156$ eV Auger peak of sulfur and the triplet of rhenium Auger peaks at $E=162$–177 eV. For calibration purposes we also used a tungsten ribbon which was cleaned and textured using a technique described in Ref. 4.

2. FORMATION OF SURFACE SULFIDE

In order to study the high-temperature adsorption behavior of sulfur, hydrogen sulfide molecules were supplied to the spectrometer chamber at elevated sample temperatures, 800–2000 K. The ribbon was held for a certain time in the H_2S atmosphere, then the hydrogen sulfide was pumped out and the Auger spectra of the sample surface were recorded. The published data[1,3,8] indicate that at $T>800$ K H_2S molecules decompose at the metal surface, the hydrogen is desorbed, and sulfur remains in the adlayer. No thermal desorption of sulfur from the surface of transition or platinum metals was observed at these temperatures. It is logical to assume a similar physical pattern for rhenium.

It was found that the sulfur concentration at the surface increases with exposure and reaches a maximum for a holding time of ~30 s (at $P_{H_2S}\sim10^{-6}$ Torr). In this case, the amplitude of the rhenium Auger signal decreases by a factor of ~1.2 and the amplitudes of the sulfur and rhenium Auger signals do not depend on the subsequent exposure to hydrogen sulfide vapor. These amplitudes also do not depend on the temperature at which the sample is exposed to H_2S in the range 800–1200 K, and do not vary during annealing in ultrahigh vacuum at $T<1200$ K. The low degree of screening of the substrate (by a factor of ~1.2) suggests that the sulfur contributing to the Auger signal is only located on the surface of the sample, since the degrees of screening observed for the formation of bulk compounds (sulfides, silicides) in the surface region of the metal are far higher.[11,13] It is logical to assume that the sulfur forms a surface sulfide on the rhenium surface similar to that observed as a result of high-temperature adsorption of sulfur on (100)W (Ref. 4) and (100)Mo (Ref. 11).

What is the sulfur concentration in the surface sulfide? It has been shown that the adsorbed S atoms do not penetrate into the interior and are apparently distributed on the surface, but their concentration definitely does not exceed a monolayer (sulfur is even desorbed from the sulfur surface at room temperature[8]). For this adlayer morphology, the Auger signal of the adsorbate is directly proportional to its concentration.

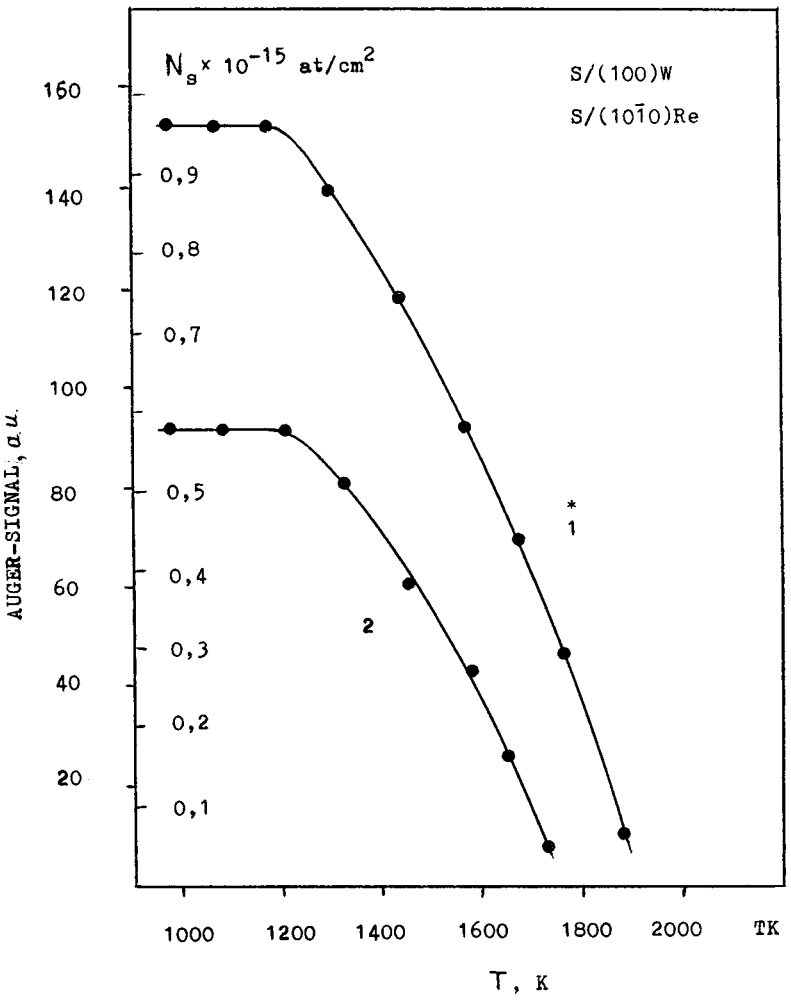

FIG. 1. Changes in the Auger signal of sulfur when surface sulfides of tungsten (*1*) and rhenium (*2*) are annealed in 100 K steps. The rhenium is exposed to H_2S vapor at $P=10^{-4}$ Torr and $T=1000$ K. The samples were held for 30 s at each point.

Figure 1 gives comparative data on the concentrations of adsorbed sulfur at (100)W and $(10\bar{1}0)$ Re surfaces obtained on the same scale, normalized so that the ratio of the amplitudes of the Auger peaks of the pure substrates corresponds to the standard.[12] Since tungsten and rhenium are neighbors in the periodic table, effects associated with the role of fast backscattered electrons at both substrates can be neglected and the amplitudes of the Auger peaks of sulfur can be compared directly.

The plateaus on the curves in Fig. 1 correspond to the surface sulfides. The sulfur concentration in the surface sulfide of tungsten is $N_S^W=(0.95\pm0.05)\times10^{15}$ atom/cm^2 (Refs. 1 and 4), whereas for rhenium this is ~1.6 times lower, i.e., $N_S^{Re}\sim(6.0\pm0.1)\times10^{14}$ atom/cm^2. Bearing in mind that the self-atom concentration at the (1010) Re face is $\sim1.3\times10^{15}$ atom/cm^2, we can easily determine the stoichiometry of the surface sulfide as Re_2S.

3. THERMAL DESORPTION OF SULFUR

Figure 1 (curve *2*) shows the changes in the Auger signals of sulfur observed when the surface sulfide obtained by holding the metal heated to $T=1000$ K is annealed in H_2S vapor ($P_{H_2S}\sim10^{-5}$ Torr, $t=30$ s). It can be seen that as far as $T=1200$ K, the Auger signal of the adsorbate remains constant, then begins to decrease, and at $T>1800$ K the metal surface is free from adsorbed sulfur. The curve remains unchanged when the exposure time of the sample in H_2S is increased to 10 min or more. It can be seen that the thermal stability of the surface sulfide on rhenium is slightly lower than on (100)W where heating to $T=1950$ K is required to clean the surface. Sulfur is only removed from the surface of tungsten and molybdenum by thermal desorption so that it is logical to assume that this is also the case for $(10\bar{1}0)$ Re.

The following experiment was carried out to check this assumption. We used an auxiliary Re ribbon, similar to the working one, which was placed ~15 mm away at an angle of 45° to the surface of the sample. The same adsorption states as on the working ribbon could be created on this auxiliary ribbon. The experiment is shown schematically in Fig. 2. Hydrogen sulfide vapor was supplied to create Re_2S surface sulfides on the auxiliary ribbon. The H_2S vapor was then extracted and the working ribbon was cleaned by heating to $T=2200$ K. When the auxiliary ribbon was heated, the sulfur atoms were desorbed and accumulated on the pure surface of the working ribbon held at room temperature, where they were recorded using an Auger electron spectrometer. The relative position of the ribbons used experimentally allowed $\sim1/30$ of all the S atoms desorbed from the auxiliary ribbon to be collected at the surface of the working ribbon.

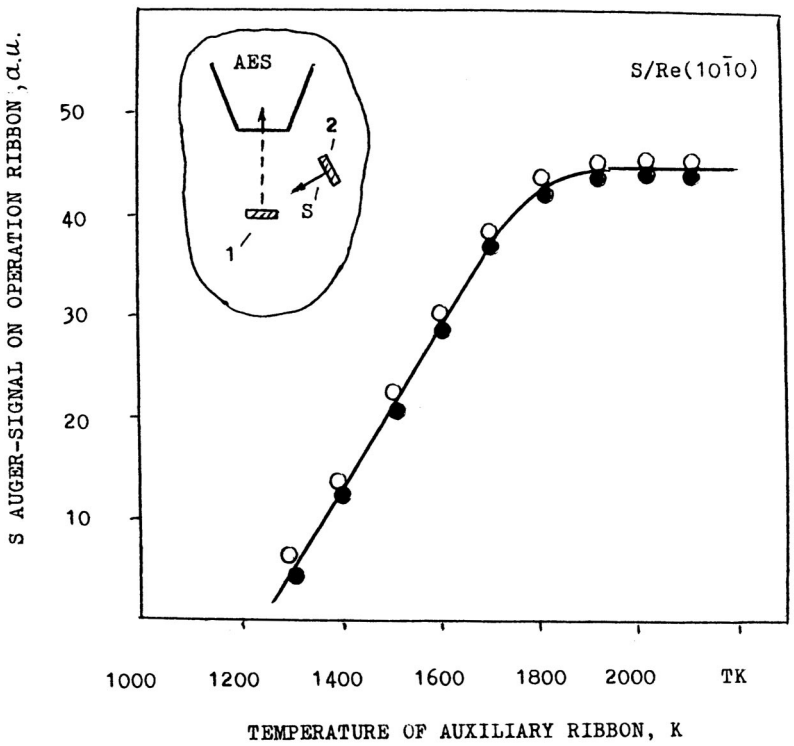

FIG. 2. Increase in the Auger signal of sulfur at the surface of the working ribbon when the auxiliary ribbon containing Re_2S surface sulfides is annealed in 100 K steps, being held for 30 s at each point. The scale is magnified eight times compared with Fig. 1. Filled circles — surface sulfides formed by exposing rhenium to H_2S vapor at 1000 K for 30 s, open circles — the same conditions but held for 10 min. The inset shows a schematic of the experiment: *1* — working ribbon ($T=300$ K), *2* — auxiliary ribbon ($T=1100-2200$ K).

The experiment was carried out as follows: at $T=1000$ K Re_2S surface sulfides formed on the auxiliary ribbon. The temperature was then raised abruptly to $T^*=1100$ K and the ribbon was held for 30 s. The desorbed sulfur was recorded on the working ribbon which was held at room temperature. The experiment was then repeated: surface sulfides were formed on the auxiliary ribbon and the working ribbon was cleaned. However, in contrast to the first experiment, the temperature of the auxiliary ribbon was raised to $T^*=1200$ K and the desorbed sulfur was again recorded from the working ribbon. In the following experiments T^* was increased by 100 K each time.

Figure 2 gives the results of the desorption of sulfur from the surface sulfide formed on the auxiliary ribbon. It can be seen that at $T<1200$ K no sulfur is desorbed from the surface. At higher temperatures the quantity of desorbed sulfur increases and stabilizes at $T>1800$ K. This suggests that the reduction in the surface concentration of sulfur observed on curve *2* in Fig. 1 is the result of its direct thermal desorption from the surface. The quantity of sulfur atoms capable of being transferred from ribbon *2* to ribbon *1* by thermal desorption, calculated from the data given by curve *2* in Fig. 1, shows good agreement with the measured Auger signals of the transferred sulfur plotted in Fig. 2.

Assuming that thermal desorption is the only process resulting in the removal of sulfur from the surface, we can estimate the change in its activation energy E_d as the surface concentration N_S decreases. For this purpose we assume the first desorption order and we use the Arrhenius formula for t, the particle lifetimes at the surface at given temperature T:

$$t=\tau_0\times\exp[E_d/kT], \tag{1}$$

where $\tau_0=10^{-13}$ s is the pre-exponential factor and k is the Boltzmann constant. In order to estimate the characteristic times of the process, we carried out isothermal annealing of the surface sulfides for each temperature plotted in Fig. 1 and we studied the rate of decrease in the sulfur Auger signal. It was found that at each temperature some of the sulfur from the surface sulfides undergoes rapid desorption and then the curves $N_S=N_S(t)$ reveal a plateau. At all temperatures the characteristic time of the process is $t\sim 10-20$ s. An estimate of the energy using formula (1) gave $E_d=(3.3\pm 0.2)$ eV for a coverage similar to the surface sulfides and $E_d=(4.9\pm 0.2)$ eV in the limit $\theta\to 0$.

It is interesting to understand whether sulfur can penetrate into the interior of the metal. Increasing the H_2S vapor pressure to $P_{H_2S}\sim 10^{-4}$ Torr and the holding time of the auxiliary ribbon to 10 min at $T=1000-1200$ K did not increase the quantity of sulfur on the working ribbon after heating the auxiliary ribbon in the range 1500–2500 (the accumulation of sulfur is the same as that given in Fig. 2). These experiments suggest that sulfur does not accumulate in the interior of the rhenium as an Re–S solid solution nor as a bulk sulfide. Thus, as for group VI metals, the high-temperature adsorption of sulfur on Re merely results in the formation of surface sulfide.

4. DISCUSSION OF RESULTS

The surface sulfide formed on the rhenium possesses Re_2S stoichiometry which differs fundamentally from the surface sulfides studied previously and from the surface sulfides of tungsten and molybdenum. This behavior is consistent with the trend familiar for bulk compounds of metals with nonmetals:[14] in the transition from group VI to VII and VIII, the stoichiometries of the minimum equilibrium bulk silicides and sulfides shift from MeX to Me_2X and even Me_3X, and no equilibrium carbides are formed.

We also note that Ogletree *et al.*[8] observed that an adsorption state characterized by the ratio of Auger peaks $I_s/I_{Re}=5.3$, a degree of substrate exposure ~ 2.3, and a $p(1\times 2)$ structure (from tunneling microscopy data) formed on the $(10\bar{1}0)$Re face as a result of the adsorption of S_2 molecules. The authors[8] consider this state to be a monolayer of chemisorbed sulfur, unfortunately omitting to clarify whether this is in the form of atoms or S_2 molecules. A comparison with our data where we showed that the ratio $I_S/I_{Re}=5.4$ is achieved in Re_2S surface sulfides and the degree of screening of the substrate is only ~ 1.2, suggests that the authors[8] observed a state formed as a result of a solid-state chemical reaction accompanied by the penetration of sulfur atoms into the interior of the substrate, as was observed previously[5,6] for Pd and Pt.

This work was supported by the Russian State Program ''Surface Atomic Structures,'' Project No. 4.6.99.

[1] V. Maurice, J. Oudar, and M. Huber, Surf. Sci. **219**, L628 (1989).
[2] N. R. Gall', E. V. Rut'kov, A. Ya. Tontegode, and M. M. Usufov, Pis'ma Zh. Tekh. Fiz. **20**(18), 65 (1994) [Tech. Phys. Lett. **20**, 754 (1994)].
[3] C. H. Dark, H. M. Kramer, and E. Bauer, Surf. Sci. **116**, 467 (1982).
[4] N. R. Gall, E. V. Rut'kov, A. Ya. Tontegode, and M. M. Usufov, Appl. Surf. Sci. **93**, 353 (1996).
[5] C. H. Peterson and R. M. Lambert, Surf. Sci. **187**, 339 (1987).
[6] A. E. Reynolds and D. J. Tildesley, Surf. Sci. **206**, L824 (1988).
[7] M. A. Van-Hove and S. Y. Tsong, J. Vac. Sci. Technol. **12**, 230 (1975).
[8] D. F. Ogletree, R. Q. Hwang, P. M. Zeglinski, A. Lopoz, Vazquez-de-Parga, G. A. Somorijai, and M. Salmeron, J. Vac. Sci. Technol. B **9**, 886 (1991).
[9] N. R. Gall, S. N. Mikhailov, E. V. Rut'kov, and A. Ya. Tontegode, Surf. Sci. **191**, 185 (1987).
[10] V. S. Fomenko, *Handbook of Emission Properties of Materials* [in Russian], Kiev (1981), 360 pp.
[11] N. R. Gall', E. V. Rut'kov, A. Ya. Tontegode, and M. M. Usufov, Zh. Tekh. Fiz. **66**(5), 143 (1996) [Tech. Phys. **41**, 483 (1996)].
[12] L. E. Davice, N. C. McDonald, P. W. Palmberg, G. E. Rich, and R. E. Weber, *Handbook of Auger Electron Spectroscopy* (Eden Prerie, 1976), p. 247.
[13] N. R. Gall, E. V. Rut'kov, A. Ya. Tontegode, and M. M. Usufov, Phys. Low-Dimens. Semicond. Struct. **9**, 17 (1998).
[14] H. J. Goldsmith, *Interstitial Alloys* (London, 1967), p. 340.

Translated by R. M. Durham

Use of ellipsometric measurements for high-sensitivity monitoring of surface temperature

M. V. Yakushev and V. A. Shvets

Institute of Semiconductor Physics, Siberian Branch of the Russian Academy of Sciences, Novosibirsk
(Submitted March 26, 1999)
Pis'ma Zh. Tekh. Fiz. **25**, 65–71 (July 26, 1999)

An analysis is made of the possibility of developing a high-sensitivity ellipsometric method of monitoring the surface temperature of samples in ultrahigh vacuum. The method is based on the temperature dependence of the phase thickness of the layer being studied. Measurements made for ZnTe layers show that the sensitivity coefficients for the ellipsometric angles ψ and Δ are 0.1 and 0.5° respectively per degree temperature. This is more than an order of magnitude higher than the sensitivity of ellipsometric methods of measuring temperature used conventionally. © *1999 American Institute of Physics.* [S1063-7850(99)02707-X]

Reliable monitoring of sample temperature under ultrahigh vacuum conditions is an important problem in technology. As a result of radiant heat exchange, in the absence of thermal contact with the heater, the temperature of the sample may differ substantially from the thermocouple readings, especially during heating or cooling. Hence, optical methods of monitoring[1] and specifically ellipsometry[2–5] are of particular interest since the surface temperature is measured directly.

Ellipsometric monitoring is based on the temperature dependence of the optical constants of the materials at a fixed wavelength, or the energy position of singular points in the spectra of the dielectric functions. In both cases, the sensitivity is 0.001–0.005° of the measured ellipsometric parameter ψ per 1 °C so that the temperature can be measured with a relative error of 5–10°.

In the present study we analyze the possibility of developing a modified ellipsometric method of monitoring temperature based on the temperature dependence of the phase thickness of a semiconductor (or other) layer deposited on a substrate. The ellipsometric parameters ψ and Δ of this system may be written symbolically in the form[6]

$$e^{i\Delta}\tan\psi \equiv \rho = F(N_s, N_f, \beta), \tag{1}$$

where N_s and N_f are the complex refractive indices of the substrate and the film, respectively, and

$$\beta = 2\pi(d/\lambda)\sqrt{N_f^2 - \sin^2\varphi} \tag{2}$$

is the phase thickness of the film. Here we use conventional notation: d is the film thickness and λ and φ are the wavelength and the angle of incidence of the light. Differentiating both sides of Eq. (1) with respect to temperature, we obtain

$$d\rho/dT = (\partial F/\partial N_s)\frac{dN_s}{dT} + (\partial F/\partial N_f)\frac{dN_f}{dT} + (\partial F/\partial\beta)\frac{d\beta}{dT}. \tag{3}$$

The first two terms on the right-hand side of Eq. (3) are ascribed to the temperature dependence of the Fresnel coefficients, and the third term is the contribution of the temperature dependence of the phase thickness to the derivatives of the ellipsometric parameters. The derivative of the phase thickness is expressed in the form

$$\frac{d\beta}{dT} = 2\pi(1/\lambda)\sqrt{N_f^2 - \sin^2\varphi}\,\frac{dd}{dT} + \frac{2\pi N_f d/\lambda}{\sqrt{N_f^2 - \sin^2\varphi}}\,\frac{dN_f}{dT}. \tag{4}$$

The first term in Eq. (4) is attributed to the thermal expansion of the film and in most cases of practical importance is negligible. The second term is determined by the temperature dependence of the optical constants of the film and, significantly, it is directly proportional to the product of the temperature sensitivity of the refractive index dN_f/dT and the thickness d. This implies that the sensitivity of the ellipsometric parameters to the change in temperature can theoretically be increased without bound by increasing the film thickness.

This then yields the main constraints on the film material which should be satisfied to maximize the sensitivity: first, the material should be transparent in the wavelength range of the probe radiation so that measurements can be made for fairly thick films; second, the temperature dependence of the refractive index should be as large as possible.

These two constraints impose partly contradictory requirements. To lowest order, for a solid we can in fact assume that the temperature dependence of N_f is caused by the temperature shift of the energy position E_i of the critical point closest to the photon energy $\hbar\omega$. Then we have

$$dN_f/dT \approx (dE_i/dT)(dN_f/d(\hbar\omega)). \tag{5}$$

For most semiconductors and insulators the value of dE_i/dT lies in a narrow range $(3-6)\times 10^{-4}$ eV/deg so that the maximum of dN_f/dT will lie in the region of strongest dispersion, i.e., close to the critical points in the Brillouin zone. However, strong absorption of light is observed in this region, which restricts the use of thick films. A compromise may be reached by using ranges of photon energies slightly

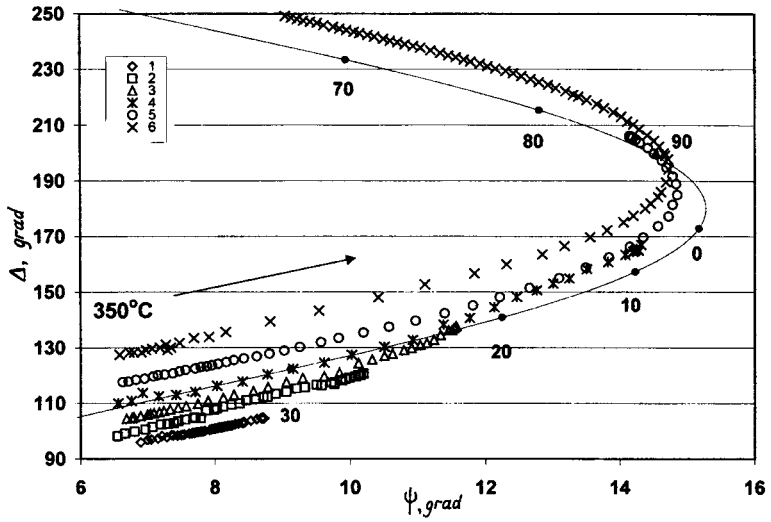

FIG. 1. Changes in ellipsometric parameters during cooling of ZnTe/GaAs samples from 350 °C to room temperature. The arrow indicates the direction of change. The experimental points are shifted along the Δ axis by −10 (*1*), −5 (*2*), 0 (*3*), +5 (*4*), +10 (*5*), and +15° (*6*). Sample thickness: *1* — 0.14, *2* — 0.25, *3* — 0.46, *4* — 0.89 , *5* — 1.75, and *6* — 2.60 μm. The solid curve gives the calculated curve for a ZnTe/GaAs system calibrated over the layer thickness in nanometers.

smaller than the band gap. In this case, it is possible to achieve negligible absorption while the dispersion of the refractive index remains fairly high.

In particular, HeNe laser radiation ($\hbar\omega = 1.96$ eV), which is usually used in monochromatic ellipsometers, falls within the region of optimum sensitivity for semiconductors such as $Cd_xZn_{1-x}Te$ ($x \leqslant 0.1$), $Al_xGa_{1-x}As$ ($x = 0.5-0.6$), and others having a band gap in the range 2.0–2.3 eV. For other semiconductors, optimum conditions can easily be achieved by using a spectral ellipsometric apparatus.

The sensitivity of the method is illustrated by the results of measurements for ZnTe films of varying thickness. The films were grown on a GaAs(001) substrate by molecular beam epitaxy. The substrate heater was calibrated using the melting points of In, Sn, and Pb and could control the sample temperature to within ±10°. The thicknesses of the as-grown films were determined *in situ* using an LÉF-701 automatic ellipsometer ($\lambda = 632.8$ nm, $\varphi = 67.5°$) and were in the range 0.14–2.6 μm.

Figure 1 shows the changes in the ellipsometric parameters observed when the samples were cooled from 350 °C to room temperature. For comparison the figure also gives the calculated dependence of ψ and Δ on the film thickness at 350 °C, which is repeated cyclically with a period $d_0 = 107$ nm. For convenience the experimental points are shifted relative to one another along the Δ axis. It can be seen that during cooling the parameters ψ and Δ are shifted along the calculated curve. This shift differs for all samples and, in units of the phase thickness, is proportional to the absolute film thickness *d*. For films having maximum thick-

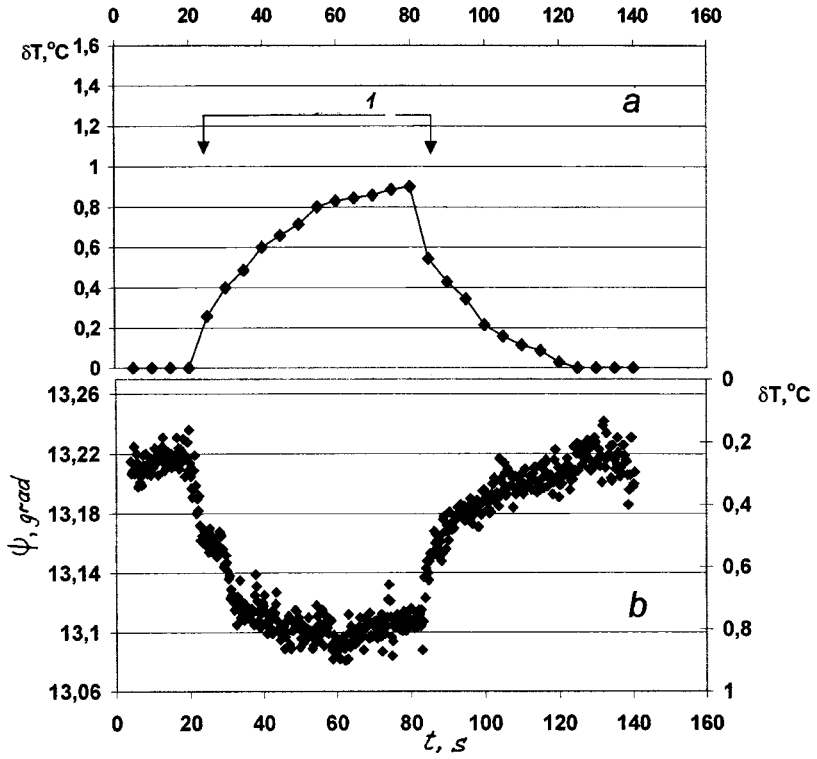

FIG. 2. Temperature of thermocouple junction (a) and the parameter ψ (b) as a function of time during heating of the sample surface by pulsed thermal radiation (*1* — heat pulse).

nesses of 2 and 6 μm the temperature sensitivity of the ellipsometric angles reaches 0.5 and 0.1° per 1 °C for Δ and ψ, respectively. This is between one and two orders of magnitude higher than the similar sensitivity parameters for measurements using homogeneous GaAs and Si substrates.[2]

The coefficient of the temperature dependence of the refractive index can be estimated from the experiments. Assuming that the inequality $N_f^2 \gg \sin^2\varphi$ is satisfied, it follows from Eq. (2) that $\delta\beta/\beta \approx \delta N_f/N_f$, where δN_f and $\delta\beta$ are the changes in the refractive index and the phase thickness during cooling. Using the experimentally determined ratio $\delta\beta/\beta$, we find $(\delta N_f/\delta T)/N_f = (9.3 \pm 0.3) \times 10^{-5}\,\mathrm{deg}^{-1}$. This value characterizes the coefficient of temperature dependence of the refractive index averaged in the range 20–350 °C and is slightly higher than the value of $7.2 \times 10^{-5}\,\mathrm{deg}^{-1}$ obtained in Ref. 1 from interferometric measurements. However, it should be noted that the ZnTe layers grown in this study had an anomalously low refractive index of 2.51 at $\lambda = 632.8$ nm, which differed from the usual value $N_f \approx 3$ (Ref. 7). In any case careful measurements of the coefficient dN_f/dT as a function of T are required to lock the ellipsometric angles to the temperature scale.

We shall discuss the minimum detectable change in temperature. This depends on the sensitivity of the ellipsometric angles $\alpha_\psi = d\psi/dT$ and $\alpha_\Delta = d\Delta/dT$ and on the measurement error for these angles $\delta\psi$ and $\delta\Delta$. As the film thickness increases, the sensitivity parameters α_ψ and α_Δ increase without bound, although their measurement errors increase. Thus, the question posed can only be answered experimentally. Such an experiment was carried out *ex situ* for a ZnTe/GaAs sample having the film thickness $d = 4.5\,\mu$m. The measurements were made using an LÉF-8 Mikroskan automatic ellipsometer. In order to improve the measurement accuracy, the size of the probe spot was reduced to $10 \times 20\,\mu$m. We clamped a thermocouple to the sample with the junction wetted with drops of liquid Ga and in thermal contact with the sample. During the measurements a heated heater coil was brought in contact with the surface of the sample. The results are plotted in Fig. 2. The thermocouple readings were converted to changes in temperature. The temperature dependence of the refractive index was then used to calculate the sensitivity α_ψ and the ψ scale was also graduated in terms of temperature.

The changes in temperature measured by the two methods show qualitative agreement. The differences of a factor of 1.5 observed in the absolute values may be attributed to the different heating dynamics of the sample surface and the thermocouple junction under conditions of a transient heat flux. The statistical spread of the parameter ψ can be used to estimate the measurement error: $\delta\psi \approx 0.01°$, and thus the minimum detectable change in temperature is ~ 0.1 °C. This value can obviously be reduced still further, but in order to achieve higher accuracy the measurement conditions must be optimized and more stringent constraints must be imposed on the quality of the sample itself and on the stability of the measuring apparatus.

To conclude, we have demonstrated that ellipsometric measurements are highly sensitive to the surface temperature of layered structures such as ZnTe/GaAs and can detect temperature changes of 0.1°.

[1] G. J. Glanner, H. Sitter, W. Faschinger, and M. A. Herman, Appl. Phys. Lett. **65**, 998 (1984).
[2] T. Tomita, T. Kinosada, T. Yamashita *et al.*, Jpn. J. Appl. Phys. **25**, L925 (1986).
[3] R. K. Sampson and H. Z. Massoud, J. Electrochem. Soc. **140**, 2673 (1993).
[4] K. K. Svitashev, V. A. Shvets, A. S. Mardezhov *et al.*, Mater. Sci. Eng., B **44**, 164 (1997).
[5] Z. T. Jiang, T. Jamaguchi, M. Aoyama, and T. Hayashi, Jpn. J. Appl. Phys. **37**, 479 (1998).
[6] R. M. Azzam and N. M. Bashara, *Ellipsometry and Polarized Light* (North-Holland, Amsterdam, 1977; Nauka, Moscow 1981, 583 pp.).
[7] *Properties of Narrow Gap Cadmium-Based Compounds*, edited by P. Gapper (INSPEC, Infra-Red Limited, London, 1994), 618 pp.

Translated by R. M. Durham

Influence of an external electric field on the recovery of stabilized zirconium dioxide under helium ion bombardment

O. N. Gorshkov, V. A. Novikov, and A. P. Kasatkin

Physicotechnical Research Institute, Nizhniĭ Novgorod State University, Russia
(Submitted January 15, 1999)
Pis'ma Zh. Tekh. Fiz. **25**, 72–75 (July 26, 1999)

It is shown that the application of an external electric field during helium ion bombardment of yttrium-stabilized zirconium dioxide single crystals may have a substantial influence on the processes accompanying the radiation-stimulated recovery of yttrium-stabilized zirconium dioxide: its *n*-type conductivity and refractive index may vary, and metallic nanosize inclusions may appear in the yttrium-stabilized zirconium dioxide matrix. © *1999 American Institute of Physics.* [S1063-7850(99)02807-4]

Allowance for the influence of internal and external electric fields on the processes accompanying ion bombardment of insulators is an important problem in solid-state radiation physics.[1] It is predicted that an external electric field may have a particularly significant influence for superionic conductors (solid electrolytes). For example, it was shown by Gorshkov *et al.*[2,3] that helium ion bombardment of yttrium-stabilized zirconium dioxide (YSZD),[4] which initially contains a high concentration of fairly mobile oxygen vacancies, causes a release of oxygen from the surface layer, whose thickness is of the order of the projected range of the helium ions. In the present study we show that the application of an external electric field during helium ion bombardment of YSZD single crystals can have a substantial influence on the processes accompanying the radiation-stimulated recovery of YSZD (changes in its *n*-type conductivity and refractive index and the appearance of metallic nanosize inclusions in the YSZD matrix), since YSZD is a material with ionic bonds and oxygen migrates in the charged state.

The initial samples were YSZD single crystals (88 mol.% ZrO_2 + 12 mol.% Y_2O_3) produced by direct rf melting in a cold container.[5] The preparation of the samples and the choice of irradiation regimes were described in Refs. 2 and 3. The samples were placed on a grounded holder and a potential relative to the holder was applied to the irradiated surface of the sample. A steel mesh (wire diameter 0.5 mm, mesh size 2.5×2.5 mm) was used as the contact clamped to this surface. The potential was equalized along the surface of the irradiated layer because of its fairly high conductivity. The YSZD was bombarded with 40 keV helium ions at a dose $\Phi=2\times10^{17}$ ions/cm^2 in an external electric field $E=2\times10^4$ V/cm. The change in the conductivity of the irradiated YSZD was determined by a standard four-probe method and the change in the refractive index of the material and the formation of metallic nanosize inclusions in the YSZD matrix was established by analyzing the light transmission spectra of the initial and irradiated YSZD samples.

The application of an electric field during irradiation in the direction conducive to the release of oxygen ions from the irradiated layer increased the conductivity of the material by about a factor of forty. The conductivity of these samples was approximately 0.8 of that of samples bombarded by an ion dose $\Phi=10^{18}$ ions/cm^2 in the absence of an external electric field ($\sim$1 S/cm the concentration of conduction electrons was 10^{19} cm^{-3}, and their mobility was $\sim$1 cm^2/V·s) (Refs. 2 and 3). This conductivity with a fairly low degree of recovery of the material is attributable to the presence of electrons in the α-band of the defect states, which is inside the band gap.[6] Assuming that the mobility of these electrons depends weakly on the ion dose and the field intensity, we find that the electron concentration with no field is 2×10^{17} cm^{-3} (0.8×10^{19} cm^{-3} with a field). Figure 1 shows the optical transmission spectra of the samples. These spectra are similar to those of samples irradiated in the absence of a field[2,3] and also contain an optical absorption band in the wavelength range $\lambda\sim400-650$ nm, which can be ascribed to the absorption of light by nanosize inclusions with metallic electrical conductivity, formed in the YSZD matrix during irradiation. The relative volume of the inclusions rose by more than a factor of three when a field was applied. The lower transmission coefficient $T(\lambda)$ in the long-wavelength region for curve *2* compared with those for the other curves stems from an increase in the refractive index of the irradiated layer, which in the absence of a field occurs at ion doses of approximately 10^{18} ions/cm^2 (Refs. 2 and 3).

To sum up, experiments to study the helium ion bombardment of YSZD with $E=40$ keV and $\Phi=2\times10^{'17}$ ions/cm^2 in an external electric field $E=2\times10^4$ V/cm have shown that this field has a substantial influence on the radiation-stimulated recovery of YSZD: the application of a field in the direction conducive to the release of oxygen ions from the irradiated layer appreciably accelerates those processes (increase in *n*-type conductivity and refractive index and the appearance of nanosize metallic inclusions) which are a consequence of the material recovery. The application of a field in the opposite direction slows these processes.

This work was carried out under a grant for research in nuclear engineering and the physics of ionized radiation beams (Section IX. Ion Beams and Scientific and Techno-

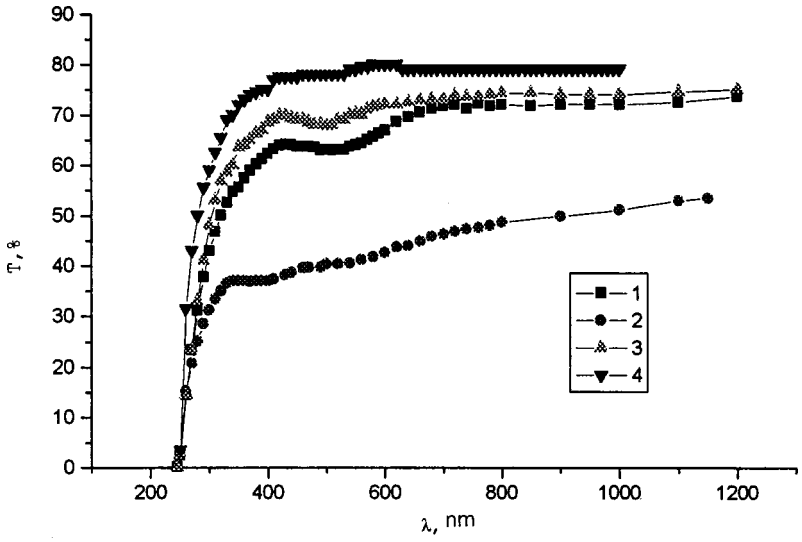

FIG. 1. Transmission spectra of initial YSZD single crystals (*4*), single crystals bombarded by helium ions with $E=40$ keV and $\Phi=2\times10^{17}$ ions/cm^2 (*1–3*) without (*1*) and with an external electric field $E=2\times10^4$ V/cm applied in the direction conducive to the release of oxygen ions from the irradiated layer (*2*) and in the opposite direction (*3*).

logical Principles of Their Applications) and also as part of the program ''Fundamental and Applied Problems of Plasma–Surface Interaction.''

[1] V. V. Gromov, *Electric Charge in Irradiated Materials* [in Russian], Energoizdat, Moscow (1982), 112 pp.
[2] O. N. Gorshkov, T. A. Gracheva, A. P. Kasatkin *et al.*, Vysokochist. Veshchest. No. 2, 85 (1995).
[3] O. N. Gorshkov, T. A. Gracheva, A. P. Kasatkin *et al.*, Poverkhnost' No. 1, 15 (1997).
[4] V. N. Chebotin and M. V. Perfil'ev, *Electrochemistry of Solid Electrolytes* [in Russian], Khimiya, Moscow (1978), 312 pp.
[5] V. I. Aleksandrov, V. V. Osiko, A. M. Prokhorov *et al.*, Usp. Khim. **47**, 385 (1978).
[6] R. I. Merino and V. M. Orera, Solid State Ionics **76**, 97 (1995).

Translated by R. M. Durham

Resonant nature of the sensitivity of gas-analytical chemical sensors using a composite acoustic resonator

S. G. Alekseev, S. V. Boritko, L. M. Dorozhkin, and G. D. Mansfel'd

Institute of Radio Engineering and Electronics, Russian Academy of Sciences, Moscow, Russia
(Submitted February 8, 1999)
Pis'ma Zh. Tekh. Fiz. **25**, 76–80 (July 26, 1999)

It is shown that the sensitivity of gas-analytical chemical sensors can be drastically enhanced when the thickness of the film deposited on the resonator surface corresponds to a quarter of the acoustic wavelength in the resonator. © *1999 American Institute of Physics.* [S1063-7850(99)02907-9]

The development of gas-analytical chemical sensors using surface and bulk acoustic waves has recently attracted increased interest. Dorozhkin *et al.*[1,2] reported the development of a gas-analytical sensor consisting of a composite acoustic resonator having a piezoelectric film which excites an rf bulk acoustic wave at one end of the acoustic line and a thin-film coating which selectively and reversibly sorbs the gas being analyzed at the other end (see inset to Fig. 1).

The physics of the operation of this device is as follows. The acoustic mode frequency of the excited piezoelectric film forming part of the resonator depends on the properties and thickness of the layers forming this film. When the gas to be analyzed is present, the parameters, and in particular the thickness of the sorbent film, vary causing a shift of the resonator operating frequency, and over a wide range of concentrations these changes are proportional to the concentration of the sample gases.

The sorbent film in gas-analytical sensors using bulk acoustic waves is conventionally considered to be a mass load which can be varied by sorption of the sample gas. This approach is justified when the thickness of the sorbent film is much less than the acoustic wavelength and is widely used, for example, in quartz microbalances.[3] In this case the sensor response depends linearly on the mass load. A different situation, not studied previously, arises when the thickness of the sorbent film becomes comparable with the wavelength. In this case it is predicted that the frequency variation of the composite acoustic resonator and consequently the sensitivity of the sensor will have a substantially stronger dependence when the thickness of the sorbent film varies in the presence of the sample gas.

The aim of the present study is to demonstrate that the sensitivity of gas-analytical chemical analyzers using composite acoustic resonators can be enhanced drastically by optimizing the thickness of the sorbent film.

A model of a composite acoustic resonator used to calculate the sensor response in gas analyses was described in detail in Ref. 4. In the notation used in Ref. 4 layer *1* corresponds to a piezoelectric film of thickness l_1 and layer *2* corresponds to a sorbent film of thickness l_2. The two films are positioned on opposite plane-parallel faces of a plate made of a material having low acoustic losses (substrate) of thickness d. For thin supply electrodes the expression for the electrical impedance has the form

$$Z_e = -iX_{C1}\left[1+\frac{K_{l1}^2 V_1}{\omega l_1}\frac{b_{11}^{(0)}}{D^{(0)}}\right], \tag{1}$$

$$b_{11}^{(0)} = [\sin w_1(\sin w \cos w_2 + \eta \cos w \sin w_2) + 2\gamma(\cos w \cos w_2 - \eta \sin w \sin w_2)(1-\cos w_1)],$$

$$D^{(0)} = \gamma\eta \sin w_1 \sin w_2 \sin w - \eta \sin w_1 \cos w_2 \cos w - \eta \cos w_1 \sin w_2 \cos w - \cos w_2 \cos w_1 \sin w,$$

where $w=qd$, $w_i=b_i l_i$, $i=1,2$, $\gamma=\rho_1 V_1/\rho V$, $\eta = r_2 V_2/\rho V$; V_1 is the velocity of sound in layer *1*, renormalized to allow for the piezoeffect; ρ_1 is its density; ρ and ρ_2 are the densities and V and V_2 are the sound velocities in the substrate and the sorbent film, respectively; K_{t1}^2 is the square of the electromechanical coupling constants of the piezoelectric film, $X_C = l_1/(\omega\varepsilon\varepsilon_0 S)$ is its capacitive reactance, and ω is the sound frequency.

We shall assume that the change in the thickness of the sorbent film is determined by its sorption capacity, and over a small range is proportional to the concentration of the gas being analyzed. This assumption is confirmed by the results of ellipsometric measurements for the sensors studied here. Using formula (1), we can find the antiresonance frequencies (i.e., the maxima of the function Z_e) for two similar values of the sorbent film thickness (the initial thickness in the absence of gas and the final thickness after sorption) and their difference determines the sensor response. The calculations were made for a composite resonator made from yttrium aluminum garnet of thickness $d=1.5$ mm with a guanidine nitrite piezoelectric film ($\rho_1=1.51$ g/cm^3, $V_1=2.2\times10^5$ cm/s) and a divinylstyrene rubber sorbent film ($\rho_1=0.93$ g/cm^3, $V_1=1.65\times10^5$ cm/s). The behavior of the resonant peaks was analyzed in the frequency range 80–110 MHz. The results of the calculations are plotted in Fig. 1 for the same relative change in the thickness of the sorbent film as a result of sorption of the sample gas. It can be seen that the frequency response of the sensor is a nonmonotonic function of the initial sorbent film thickness and has a maximum when the thickness is a quarter of the acoustic wave-

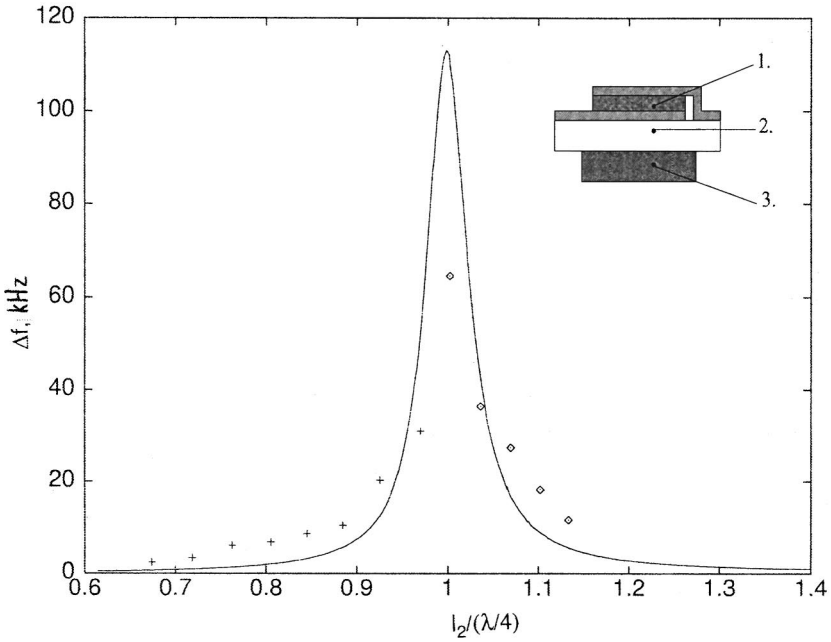

FIG. 1. Frequency shift of composite acoustic resonator when sample gas is supplied as a function of the parameter $l_2(\lambda/4)$: *1* — piezotransducer, *2* — acoustic line, and *3* — sorbent film.

length (at 100 MHz this is $\lambda/4=4.125\,\mu$m). Note that the calculations predict even larger frequency shifts for films whose thickness is an odd number (3, 5, 7, and so on) of quarter wavelengths.

In order to check this theory experimentally, we investigated two samples of sensors on yttrium aluminum garnet substrates with 3.5 and 4.5 μm thick sorbent films made from DST-30 divinylstyrene rubber. The sample gas supplied to the sensors was *n*-octane at a constant concentration of order 2500 ppm.

The symbols in Fig. 1 show the change in the frequency of the various modes of the composite resonator when the sample gas is supplied (the left-hand wing with an initial sorbent film thickness of less than $\lambda/4$ is the first sensor and the right-hand wing with an initial thickness of $\geqslant\lambda/4$ is the second). It can be seen that the calculations and experiment show good agreement, which supports the assumption that the sensor response exhibits resonant behavior as the operating frequency of the composite resonator varies. The observed discrepancy between the absolute values of the amplitudes of the resonant peaks can be explained by the fact that the calculations neglected any change in the attenuation factor and the velocity of the acoustic waves in the sorbent film during sorption of the sample gas.

Note that the choice of sample gas and sorbent was not a random one. Recently, particular attention has been focused on the development of sensors to determine explosive concentrations of fuel vapor in commercial oil and gas installations and also for selecting types of fuel and high-speed monitoring of gasoline grades. Octane is the most notable representative of the sample gases for fuels: however, DST-30 films also fairly effectively sorb vapor of heavy hydrocarbons.

To sum up, we have shown that the frequency shift of a composite acoustic resonator increases abruptly when the thickness of the film deposited on its surface corresponds to a quarter of the acoustic wavelength in the resonator. This study has a highly significant practical result: by correctly selecting the material for the composite resonator and the thickness of the sorbent film, we can improve the sensitivity of gas-analytical sensors based on composite acoustic resonators by factors of ten.

In conclusion, the authors are grateful to colleagues at the Institute of General and Inorganic Chemistry of the Russian Academy of Sciences L. M. Dorozhkin and G. N. Dorozhkina for supplying the sensor samples, and to A. A. Lavrenov and I. A. Rozanov for useful discussions and for supporting this work.

[1] L. M. Dorozhkin, V. S. Doroshenko, Yu. M. Krasilov, N. T. Kuznetsov, D. A. Murashov, and I. A. Rozanov, Zh. Anal. Khim. **50**, 979 (1995).
[2] L. M. Dorojkin, V. V. Volkov, V. S. Doroshenco, A. A. Lavrenov, D. A. Mourashov, and I. A. Rozanov, Sens. Actuators B **44**, 488 (1997).
[3] V. V. Malov, *Piezoresonance Sensors* [in Russian], Énergoatomizdat, Moscow (1989), 450 pp.
[4] G. D. Mansfel'd and S. G. Alekseev, Radiotekhnika **1**, 75 (1988).

Translated by R. M. Durham

Production of highly dispersed metal powders by electrical explosion in reduced-pressure nitrogen

V. S. Sedoĭ and V. V. Valevich

Institute of High-Current Electronics, Siberian Branch of the Russian Academy of Sciences, Tomsk, Russia; Tomsk State University of Control Systems and Radio Electronics, Tomsk, Russia

(Submitted April 7, 1999)
Pis'ma Zh. Tekh. Fiz. **25**, 81–84 (July 26, 1999)

It is suggested that nitrogen may be used as the ambient medium to obtain highly dispersed powders of pure metals. At reduced pressure nitrogen is chemically inert and has a higher dielectric strength than rare gases. A reduction in the gas density reduces the particle size of the pure metal powder down to the nanometer range. © *1999 American Institute of Physics.* [S1063-7850(99)03007-4]

1. The electrical explosion of wires can be used to obtain powders of various metals. Their dispersion and properties depend on many factors, the most important being the energy density deposited in the wire material,[1,2] the density of the ambient gas,[3–5] and its chemical activity.[2,4,6] Traditionally explosions have been conducted in rare gases (Ar, Xe)[3] at elevated pressure to obtain pure metal powders. In the present study we suggest using an electrical explosion in nitrogen at reduced pressure. The activation energy for the formation of nitrides is fairly high and nitrogen may exhibit the properties of a rare gas.

2. We investigated the preparation and various characteristics of aluminum, copper, cobalt, and indium powders. While producing the samples we monitored the parameters of the LC discharge circuit and the current, which were used to control the energy density w deposited in the material. The electrical explosion regime was close to a matched regime when almost all the energy stored initially in the capacitance C is released in the wire. In each case the gas pressure P (Ar, Xe, N_2) was set at the lowest possible level (or slightly higher) so that the explosion took place when the current ceased.[7] Under these conditions the wire is not shunted by a discharge in the ambient medium.

The samples were analyzed using the following methods and devices. The specific surface area S of the powder was determined by low-temperature adsorption of nitrogen. A phase analysis of the samples was made using a DRON-UM1 x-ray apparatus. The bound nitrogen content was also determined quantitatively by dissolving the samples in boiling sulfuric acid by the Kjeldahl method and in boiling concentrated alkali.

Differential thermal analysis of the oxidation of the powders in air was used to compare their chemical activity. For this analysis we compared the temperatures T at which intensive oxidation begins and the mass increment Δm as a result of oxidation. The results are presented in Tables I and II.

3. The experiments showed that molecular nitrogen is chemically inert at reduced pressure. No nitrides were detected in any of the metal powders investigated, as is confirmed by chemical and x-ray analyses. The chemical analyses showed that when exploded in nitrogen, aluminum, which is considered to be a metal that readily forms nitrides,[8] produces an appreciable (more than 2 wt.%) quantity of AlN at pressures exceeding 350 Torr. The dissociation energy of the nitrogen molecule (53.7 kJ/mol) is much higher than the sublimation energy w_s of the metal, which for aluminum is 18.8 kJ/mol, and is close to the energy density preliminarily stored in the electric circuit. Additional activation is required to synthesize the nitride. Other important factors may be the loss of nitrogen stoichiometry in the reaction zone at reduced pressure and the short-lived nature of the process.

A comparison of the results presented in the tables suggests the following fundamental dependences.

Nitrogen has the highest dielectric strength, followed by xenon and argon which is qualitatively fully consistent with the right-hand region of the well-known Paschen curves. A nitrogen-containing gap sustains the same voltage at a lower pressure. In this case, the pressure depends not only on the electric field strength and the type of ambient gas but also on the wire material, the amount of energy released, and the time of application of the voltage. The characteristic times

TABLE I. Results of analysis of copper powder.

No.	w/w_s	E, kV / cm	τ, 10^{-6} s	Gas	P, Torr	S, m^2/g	T, °C	Δm, %
1	0.8	1.2	1.9	N_2	30	3.7	120	21
2	0.8	1.2	1.9	Ar	450	2.2	130	22
3	1.0	0.9	3.0	N_2	120	8.9	188	11
4	1.0	0.9	3.0	Ar+He	225+435	6.2	111	13
5	1.0	0.9	3.0	Xe+He	225+165	5.8	159	12

TABLE II. Results of analysis of aluminum powders.

No.	w/w_s	E, kV / cm	τ, 10^{-6} s	Gas	P, Torr	S, m^2/g	T, °C	Δm, %
1	0.75	1.0	1.8	N_2	105	22	289	5.2
2	0.75	1.0	1.8	Ar	510	18	355	9.4
3	0.75	1.0	1.8	Xe	330	9.3	375	13.3
4	1.0	1.4	1.8	N_2	150	24	350	18.0
5	1.0	1.4	1.8	Ar+He	100+466	–	293	14.8
6	1.0	1.4	1.8	Xe	450	16.1	293	5.2

$\tau=(LC)^{0.5}$ are given in Tables I and II in order to estimate this time.

The dispersion of the powder increases as the deposited energy density increases. Other conditions being equal, the deposited energy density is increased by increasing the electric field strength along the wire, which requires an increase in the dielectric strength of the ambient gas, i.e., an increase in pressure. As the ambient gas pressure increases, the dispersion of the powder decreases. Nevertheless, the increase in the dispersion with increasing deposited energy density remains appreciable. Since the particle size depends on the density of the ambient gas, powders obtained in nitrogen will have a higher dispersion for the same deposited energy density.

The activity of the samples can be compared by means of a differential thermal analysis of the oxidation of powders obtained in various gases. Samples obtained in nitrogen at low deposited energy density (No. 1 in Tables I and II) begin to undergo intensive oxidation at lower temperatures than samples obtained in rare gases at the same energy density. However, samples obtained in nitrogen at higher deposited energy become passivated. This behavior is seen particularly clearly for aluminum powder (Table II) for which the temperature for the onset of intensive oxidation becomes higher (289 °C and 350 °C, respectively for samples 1 and 4 in Table II) and the mass increment as a result of oxidation increases. Powders obtained in nitrogen exhibit high activity and do not require additional passivation.

4. To sum up, we have shown that it is potentially useful to produce pure metal powders in reduced-pressure nitrogen. Nitrogen has a higher dielectric strength and low mass density than rare gases and this can increase the dispersion of the powder. However, metal powders obtained in nitrogen exhibit fairly high chemical activity in a test oxidation reaction.

The authors are grateful to colleagues at the Institute of Oil Chemistry of the Siberian Branch of the Russian Academy of Sciences and the Institute of Strength Physics and Materials Science of the Siberian Branch of the Russian Academy of Sciences for performing the analyses.

This work was financed by Grant IG No. 20 from the Siberian Branch of the Russian Academy of Sciences.

[1] Yu. A. Kotov and N. A. Yavorskiĭ, Fiz. Khim. Obrab. Mater. No. 6, 24 (1978).
[2] V. V. Valevich and V. S. Sedoĭ, Izv. Vyssh. Uchebn. Zaved. Fiz. No. 6, 70 (1998).
[3] G. P. Glazunov, V. P. Kantsedal, L. A. Kornienko *et al.*, Voprosy Atomn. Nauki i Tekhniki. Ser. Atomn. Materialovedenie **1**(1), 21 (1978).
[4] V. S. Sedoi, V. V. Valevich, and J. D. Katz, Aerosols **4**(2), 48 (1998).
[5] W. Jiang and K. Yatsui, IEEE Trans. Plasma Sci. **26**, 1498 (1998).
[6] Yu. A. Kotov and O. M. Samatov, Poverkhnost' **10**, 90 (1994).
[7] E. I. Azarkevich, Yu. A. Kotov, and V. S. Sedoĭ, Zh. Tekh. Fiz. **45**, 175 (1975) [Sov. Phys. Tech. Phys. **20**, 111 (1975)].
[8] G. V. Samsonov, O. P. Kulik, and V. S. Polishchuk, *Preparation and Methods of Analysis of Nitrides* [in Russian], Naukova Dumka, Kiev (1978), 317 pp.

Translated by R. M. Durham

Recording of the dynamic wave structure at the surface of a rotating liquid

P. P. Belousov, P. Ya. Belousov, and Yu. N. Dubnishchev

Institute of Heat Physics, Siberian Branch of the Russian Academy of Sciences, Novosibirsk
(Submitted January 18, 1999)
Pis'ma Zh. Tekh. Fiz. **25**, 85–89 (July 26, 1999)

Methods of laser fiber-optic 2D Doppler anemometry and shadow visualization were used for the first time to record the wave structure at the surface of a rotating liquid. © *1999 American Institute of Physics.* [S1063-7850(99)03107-9]

Experimental investigations of wave processes at the surface of a rotating liquid are related to the problem of modeling the influence of the Earth's rotation on wave motion and tidal phenomena in the oceans. Although the theory of these processes has been developed in great detail, the experimental modeling and substantiation of the theoretical conclusions encounters considerable difficulties. The possibility of studying these wave structures under laboratory conditions is limited by the level of metrological precision, for which the requirements include making nonperturbing measurements and high sensitivity, particularly when determining the component of the local velocity vector of the liquid surface collinear to the axis of rotation.

We know[1,2] that the surface wave structure of a liquid in a rotating basin is described in cylindrical coordinates (r, θ) by the Helmholtz equation whose solution has the form

$$z = J_m(kr)\cos(\omega t - m\theta),$$

where ω is the natural frequency of the oscillations, $m = 0, \pm 1, \pm 2, \ldots$, and $k^2 = (\omega^2 - 4\Omega^2)/gh$; here Ω is the angular rotation velocity, h is the basin depth, and g is the acceleration due to gravity. In this case, the boundary-value problem has no simple solution. The wave structure may contain symmetric and antisymmetric oscillation modes. Rotation causes mode splitting and the solution consists of a complex system of Kelvin and Poincaré waves propagating in the direction of rotation of the basin and in the opposite direction. The development of a fiber-optic laser Doppler meter for measuring the 2D velocity vector in an orthogonal coordinate basis formed in a two-beam differential configuration[3,4] opened up possibilities for providing the metrology in experimental investigations under laboratory conditions. This device could be used for experimental investigations of the structure of waves excited at the surface of water in a rotating cylindrical container. The experiment is shown schematically in Fig. 1. The component of the velocity vector collinear to the axis of rotation (v_z) and the tangential component (v_x) were measured simultaneously. The sensitivity of the meter for the axial component is $\gamma_z = f_{Dz}/v_z = 3\,(\mathrm{MHz}\cdot\mathrm{m})/\mathrm{s}$ and for the tangential component $\gamma_x = f_{Dx}/v_x = 0.108\,(\mathrm{MHz}\cdot\mathrm{m})/\mathrm{s}$, where f_{Dz} and f_{Dx} are the Doppler frequency shifts in the z and x measuring channels. Thus, the sensitivity of the measurements of the axial component was ~ 30 times that for the tangential component. The high resolution of the device revealed the dynamic wave structure at the surface of the rotating liquid.

Figure 2 gives an example of the analog signals reflecting the time behavior of the tangential component (upper trace) and the collinear component (lower trace) of the local velocity vector of the surface waves relative to the axis of rotation in the laboratory coordinate system. The analog signal corresponding to v_z is shown in Fig. 2b. The upper trace shows the locking signal with the rotation of the container. These signals did not vary when the probe field was displaced along the radius which indicates that radial nodal lines are present in the wave structure. Figure 2c shows the signal corresponding to the v_z component when the angular velocity is slightly increased.

Figure 3a shows the dynamic relief of the surface waves

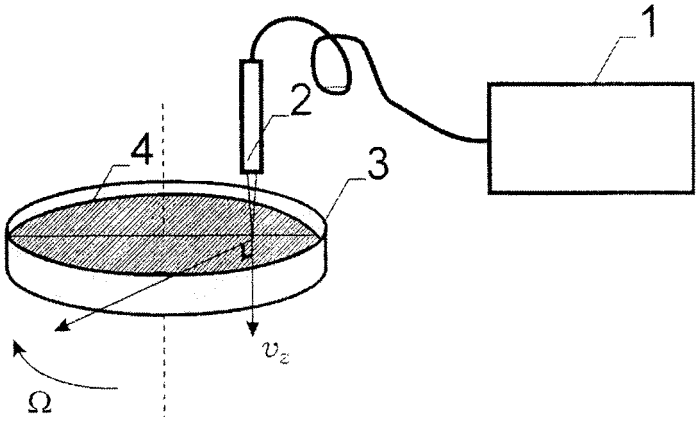

FIG. 1. Schematic of experiment: *1* — 2D laser velocity vector meter, *2* — fiber-optic probe, *3* — rotating cylindrical vessel containing water ($\phi = 170$ mm, depth $h = 50$ mm, angular velocity $\omega \sim 0.75$ rev/s), and *4* — water surface.

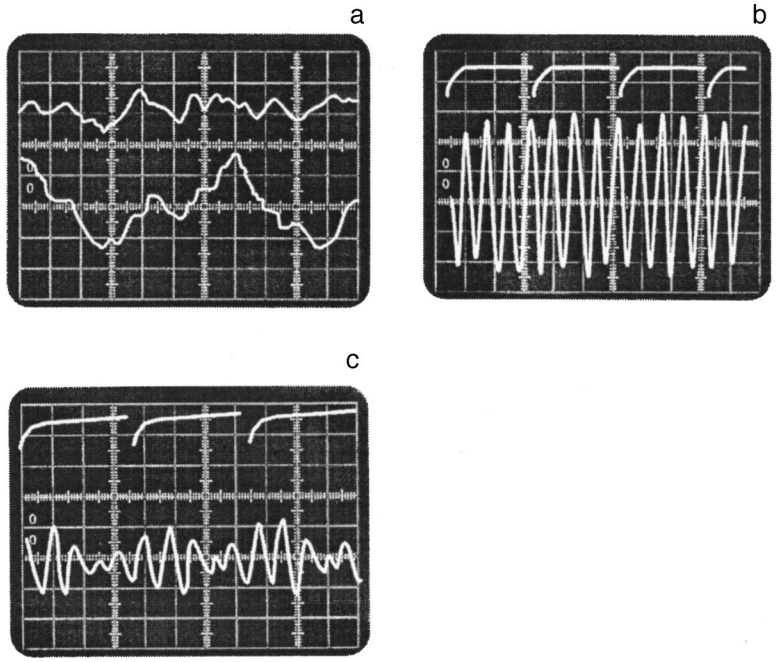

FIG. 2. Measurement of the tangential component v_x and the collinear component v_z of the surface wave velocity relative to the axis of rotation: a — analog signals corresponding to v_x (upper trace) and v_z (lower trace) components of the velocity vector (vertical scale v_x — 15.5 mm/s per cell, v_z — 0.56 mm/s per cell, horizontal scale — 0.1 s per cell); b — analog signal corresponding to the v_z velocity component. The upper trace gives the locking signal with the rotation of the cylindrical container (the length of the markers corresponds to a rotation period $T=1.33$ s). Vertical scale 0.56 mm/s; c — analog signal corresponding to the v_z velocity component. The rotation frequency is slightly increased compared with Fig. 2b.

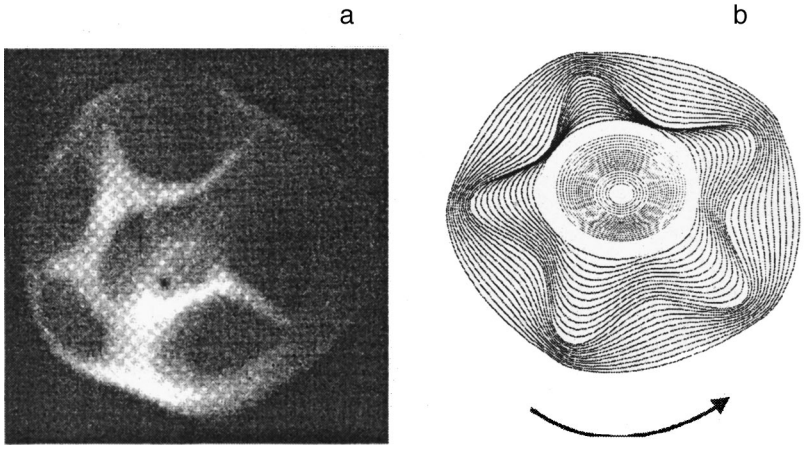

FIG. 3. a — Dynamic relief of surface waves (five-pronged structure) visualized by oblique illumination. Wave amplitude ~0.3 mm; b — qualitative form of five-pronged structure of the dynamic surface wave profile (not to scale).

(five-pronged rotating structure) visualized by oblique illumination. The amplitude of the relief gradient (from the peak to the trough) is 0.3 mm. Visualization presents serious problems. Considerable difficulties are encountered when classical methods are used (such as modification of the Hilbert transform in reflected light[5]) because of the paraboloid shape of the mean surface level of the liquid as it rotates. Visualization using oblique illumination and suitable spatial filtering can reveal the dynamic structure of the surface, but projection distortions are introduced. Figure 3a clearly shows the five-pronged radial ($m=5$) and concentric structure of the nodal lines which reflect an antisymmetric oscillation mode.[6] Figure 3b gives a qualitative representation (not to scale) of the five-pronged structure of the dynamic relief. These examples of the surface wave structure of a rotating liquid are consistent with the theoretical models and confirm that these optical methods are adequate for this class of hydrodynamic problems.

The authors thank V. G. Meledin, G. V. Bakakin, I. V. Naumov, and V. V. Sotnikov for assistance with the work.

This work was supported by the Russian Fund for Fundamental Research, 96-02-19246.

[1] H. Lamb, *Hydrodynamics*, 6th ed. (Cambridge University Press, Cambridge, 1932; Gostekhteoretizdat, Leningrad, 1947, 928 pp.).
[2] L. N. Sretenskiĭ, *Theory of Wave Motion in Liquids* [in Russian], ONTI NKTD SSSR, Leningrad (1936), 303 pp.
[3] Yu. N. Dubnishchev, Avtometriya No. 2, 13 (1996).
[4] P. P. Belousov, P. Ya. Belousov, and Yu. N. Dubnishchev, Avtometriya No. 2, 8 (1998).
[5] V. A. Arbuzov, Yu. N. Dubnishchev, A. V. Lebedev *et al.*, Pis'ma Zh. Tekh. Fiz. **23**(23), 84 (1997) [Tech. Phys. Lett. **23**, 938 (1997)].
[6] P. Le Blond and L. Maĭsek, *Waves in the Ocean*, Part 1, Mir, Moscow (1981), 480 pp.

Translated by R. M. Durham

Plasma parameters of an electron cyclotron resonance discharge in a magnetic mirror in a quasi-gasdynamic confinement regime

A. V. Vodop'yanov, S. V. Golubev, V. G. Zorin, S. V. Razin, and M. A. Shilov

Institute of Applied Physics, Russian Academy of Sciences, Nizhniĭ Novgorod, Russia
(Submitted March 25, 1999)
Pis'ma Zh. Tekh. Fiz. **25**, 90–93 (July 26, 1999)

An experimental investigation is made of x-ray bremsstrahlung in the 2–10 keV range of a pulsed discharge under electron cyclotron resonance conditions in a straight magnetic mirror system pumped by a high-power millimeter radiation beam. The plasma temperature and density were determined from the spectrum and intensity of the x-rays. The results indicate that a quasi-gasdynamic plasma confinement regime is achieved. © *1999 American Institute of Physics.* [S1063-7850(99)03207-3]

At present, microwave discharges in heavy gases in open magnetic systems under electron cyclotron resonance (ECR) conditions are attracting considerable attention. This type of discharge is widely used in multiply charged ion sources for cyclotron accelerators.[1] The possibility of using an ECR discharge as a source of soft incoherent x-rays[2–4] for high-resolution lithography is also being considered. The prospects for improving the operating efficiency of these sources, i.e., increasing the ion charge state, the ion beam current, and the soft x-ray intensity involve using higher-frequency, higher-power gyrotron radiation. This is because increasing the radiation frequency is predicted to substantially increase the plasma density, which will not only increase the ion current but will also establish so-called quasi-gasdynamic confinement of a nonequilibrium plasma (the electron temperature is much higher than the ion temperature).[5,6] The plasma density at which the confinement mechanism changes can be estimated from the condition that the classical confinement lifetime $\tau_c \approx \nu^{-1}$ (where ν is the electron–ion collision frequency[7]) equal the gasdynamic confinement time $\tau_g \approx kL/(V_s)^{-1}$ (where k is the mirror ratio of the system, L is its length, and V_s is the ion-acoustic velocity).[8] In the quasi-gasdynamic confinement regime the plasma lifetime in the system depends weakly on its density and thus, as the plasma density increases, the conditions for the formation of multiply charged ion sources improve (the parameter $N\tau$ increases where N is the electron density and τ is the plasma lifetime). Naturally, as the plasma density increases, the electron temperature must be maintained at a sufficiently high level optimum for multiple ionization ($\sim$1000 eV). The authors of Ref. 6 attribute the establishment of this regime to a substantial shift of the ion charge distribution toward higher degrees of ionization (the average charge of the argon ions in Ref. 6 was 11–12, whereas in conventional sources using a significantly lower microwave radiation frequency the average charge of the argon ions did not exceed 8). It is therefore highly relevant to measure the plasma density and the electron temperature in an ECR discharge. In the present paper these parameters were determined by measuring the absolute intensity of the x-ray bremsstrahlung.

The experiments were carried out using the apparatus shown schematically in Fig. 1. Linearly polarized microwave radiation was fed into a discharge chamber having a characteristic transverse dimension of 14 cm, inserted in a straight magnetic mirror. The pulse duration of the magnetic field was $\sim$13 ms, the system length was 25 cm, the mirror ratio was 3.5, and the maximum magnetic field intensity in the mirror was 2.3 T. The working gas was argon at a pressure of $\sim 4\times10^{-4}$ Torr. The discharge x-ray radiation was investigated in the range 2–10 keV using an XR-100T cooled PIN-diode analyzer. The device operates in the photon counting mode and the maximum rate of information processing is 10^4 photons per second. The spectral resolution is 250 eV. The diode was placed on the axis of the mirror 130 cm from the center of the discharge. The required attenuation of the x-ray flux was provided by a freely suspended aluminum filter and collimator.

Figure 2 shows the plasma radiation spectrum obtained by accumulating information from 250 discharge shots. The measurements were processed assuming that the photon re-

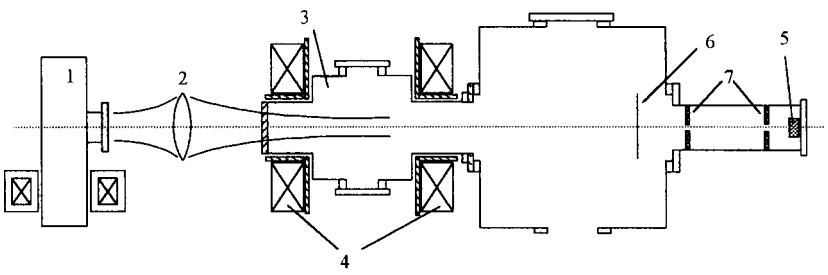

FIG. 1. Schematic of apparatus: *1* — gyrotron (f = 37.5 GHz, T = 1 ms, P = 130 kW), *2* — focusing dielectric lens, *3* — vacuum chamber, *4* — solenoids of magnetic mirror confinement system, *5* — XR=100T x-ray analyzer, *6* — aluminum filter (15 μm thick), and *7* — lead collimator.

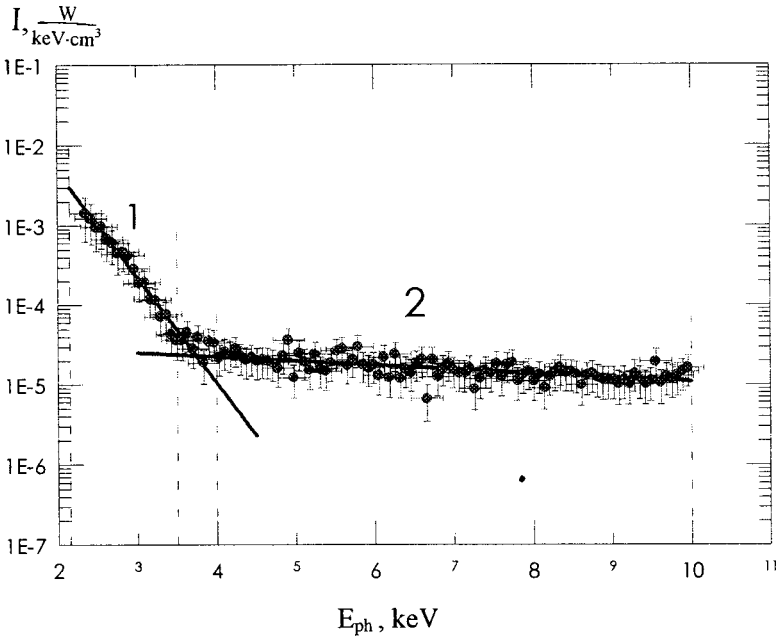

FIG. 2. Spectral intensity of plasma x-rays.

cording efficiency depends on their energy, the transmission coefficient of the aluminum filter, and the beryllium input window of the analyzer. The dependence of the radiation intensity on the photon energy in a semilogarithmic plot is fairly well approximated by two straight lines. Estimates show that this spectrum corresponds to plasma x-rays with a two-temperature electron energy distribution. It can be seen from this spectrum that the first group of electrons has a temperature of 300–400 eV and the second group has a temperature of 7–10 KeV. The measured absolute x-ray intensities can also be used to determine the densities of these two groups of electrons. For this we need to know the effective ion charge although the plasma density depends weakly (as the square root) on this value. On the basis of the results reported in Ref. 6, under the experimental conditions described the effective ion charge is taken to be 6. As a result, the density of the low-temperature group of electrons was of the order of $10^{14}\,\mathrm{cm}^{-3}$ and that of the high-temperature group was of the order of $10^{10}\,\mathrm{cm}^{-3}$.

The measured parameters indicate that a quasigasdynamic plasma confinement regime can be established under the experimental conditions, since the inequality $\tau_g > \tau_c$ is satisfied for the plasma density and electron temperature achieved experimentally.

The authors are grateful to Professors S. Myake and N. Abe (Osaka University, Japan) for their cooperation with the experiments and for useful discussions.

[1] R. Geller, B. Jacquot, and P. Sortais, Nucl. Instrum. Methods Phys. Res. A **243**, 244 (1986).
[2] Y. Arata, S. Myake, H. Kishimoto, N. Abe, and Y. Kawai, Jpn. J. Appl. Phys. No. 7, 1281 (1988).
[3] Y. Arata, S. Myake, and H. Kishimoto, Jpn. J. Appl. Phys. **28**(7), 234 (1989).
[4] S. V. Golubev, V. G. Zorin, Yu. Ya. Platonov, and S. V. Razin, Pis'ma Zh. Tekh. Fiz. **20**(4), 7 (1994) [Tech. Phys. Lett. **20**, 135 (1994)].
[5] S. V. Golubev, V. G. Zorin, T. N. Zorina, and S. V. Razin, in *Proceedings of International Workshop on Strong Microwaves in Plasmas*, Nizhniĭ Novgorod, 1991, Vol. 1, pp. 485–489.
[6] S. V. Golubev, V. G. Zorin, and S. V. Razin, Pis'ma Zh. Tekh. Fiz. **23**(8), 60 (1997) [Tech. Phys. Lett. **23**, 319 (1997)].
[7] V. P. Pastukhov, Nucl. Fusion **14**, 3 (1974).
[8] D. D. Rutov, Plasma Phys. Controlled Fusion **28**, 191 (1986).

Translated by R. M. Durham